(1)

Effects of Vibrational and Translational Energies on Chemical Reactions

Akihiro Watanabe

Doctoral Program in Fundamental Science and Technology

Graduate School of Science and Technology

Niigata University

Preface and Acknowledgments

This dissertation is described on the basis of my study in Niigata university from 1994 to 1997. I have studied the chemical reaction in gas phase by kinetic approach and treated various radicals using pulse lasers: Amidogen (NH_2), difluoromethylene (CF_2), and hydroxyl radical (OH).

I wish to express my sincere thanks to Professor Ikuo Tokue for his kind guidance and encouragement for these years.

I am deeply grateful to Professor Katsuyoshi Yamasaki, whose scientific discernment, boundless enthusiasm, and persistent encouragement for my graduate course.

I am deeply indebted to Dr. Keiich Yokoyama for calculation of energy diagram of the reaction system CF_2 + O and helpful advice on quantum calculation.

I express my sincere gratitude to Professor Yoshio Masuda, Professor Noriyuki Shimakura, and Professor Yoshio Ito for their significant suggestions in the seminar.

I wish to thank other Professors in department of chemistry and I am indebted to Mr. Takuya Hasegawa and Mr. Akio Ishii for their technical support and helpful advice.

Special thanks go to the members of the kinetics group and my friend: Ms. Tomoko Kimura, Mr. Hiroshi Masuya, Mr. Manabu Satho, Mr. Akira Itakura, Mr. Teruaki Kakuda, Mr. Hirofumi Fukushima, and Mr. Aki Tanaka for their technical assistance, many discussions, friendship and making these years actually quite enjoyable and memorable.

Finally, many thanks are also extended to all my family for moral support to my graduate study.

CONTENTS

CHAPTER 1 GENERAL INTRODUCTION

Chemical reaction is defined to be the spatial rearrangement of atoms or groups in molecules. There have been two types of approach for studying chemical reactions. One is "*kinetics*" giving information about rates of reactions; the other is "*dynamics*" elucidating how chemical bonds are rearranged. Chemical reactions have been studied in many fields for a long time even in the period of alchemy and iatrochemistry and lots of researchers have put their heart into the study on chemical reactions. Establishment of the body of theory about chemical reaction has made progress since mid-nineteenth century. A basic theory of chemical kinetics had arisen from the study of Wilhelmy[1] in 1850. Theory of chemical kinetics made rapid progress with the development of chemical industry in the industrial revolution.

A modern chemical kinetics is based on the concept of "activation of molecules", and rate constant is expressed by the following Arrhenius equation:

$$k = A\exp(-E/RT), \qquad (1)$$

where A is a pre-exponential factor and E is an activation energy of a reaction. Arrhenius had presented the equation in 1989[2] and the equation is still utilized in the analysis of kinetic studies. Basic concept of a reaction mechanism in gas phase had been established by the studies on the decomposition of N_2O_5 (Daniels and Johnston[3]) and the reaction between halogen and H_2 (Bodenstein and Lind[4]). These experiments indirectly traced reactions by a change of physical quantity, for example, total pressure of system.

Direct observation of reactions by spectroscopic technique had begun in 1920's. Hartridge and Roughton[5] studied the reaction between hemoglobin and O_2 or CO by the flow method coupled with an irradiation of light, and they monitored absorption with a monochromator in 1921. In 1930's, Rabinowitch and Lehmann[6] used arc discharge in gaseous Br_2 and I_2, and detected the change in absorbance of halogen molecule with a photomultiplier tube in the study on the recombination of halogen atoms. After their pioneering work, photolysis for producing activated molecules and atoms, and spectroscopic techniques for detecting molecules and atoms of interest have widely used in the fields of kinetics.

Polanyi[7] reported an elementary reaction and gave a concept of reaction dynamics in the study of atomic frame produced in the reaction of alkaline metal with halogen. He related the energy partitioning of reaction products and the potential energy surface. A correlation between quantum states of reactants and products were discussed and a kind of propensity had been established. Since then, a new approach which called reaction dynamics has made progress in the studies on chemical reactions.

The invention of lasers in 1960's had brought a revolution of the study on chemical reactions. Lasers offer high resolutions of time and energy. Production for high concentration of radicals and atoms by photolysis was achieved by the lasers, and sensitive detections such as laser-induced fluorescence (LIF)[8] and multiple-photon ionization (MPI)[9,10] were developed. A single quantum state of reactants and products can be detected by these techniques.

The goal of the present study is to elucidate the effect of the degrees of

freedom on chemical reactions. Studies on rate constants and quantum state distributions extract the information on the dynamics of elementary reactions. If the vibrational motion of the reactants changes the rate of reaction or opens new reaction path, a quantum control of chemical reactions may be realized.

Temperature dependence of rate constants has been measured and activation energy has been obtained by equation (1). Since the reactants are thermalized to ambient temperature, the correlation between reaction rates and the degrees of freedom cannot be elucidated by only temperature dependence. In this dissertation, the effects of vibrational and translational energies on chemical reactions were studied. Degrees of freedom, particularly vibration and translation, were excited with pulse lasers, and the state specific rate constants are determined. Details of reaction mechanism have been derived from a theoretical calculation in combination with results of the kinetic studies. Furthermore, a new method of analysis was developed for simultaneous determination of the rate constants and the initial products distributions of reaction or photolysis.

This dissertation consists of six chapters. A brief explanation of each chapter is described below:

(1) General introduction (this chapter).

(2) Chemiluminescent reaction following the uv photolysis of HN_3: Dispersed emission spectra of the chemiluminescence were recorded in the uv photolysis of hydrogen azide (HN_3), and assigned to electronic transitions of $NH_2(\tilde{A}^2A_1-\tilde{X}^2B_1)$. It is found that the vibrationally excited $NH_2(\tilde{A})$ is produced in the reaction of vibrationally excited $NH(a^1\Delta)$ with HN_3. The rate constants

for the production of various vibrational levels of amidogen, $NH_2(\tilde{A})$, and their dependence on photolysis wavelength were determined. The potential energy surface governing the reaction NH(a) + HN_3 was derived.

(3) Experimental apparatus: Apparatus and techniques for the measurement of rate constants are described.

(4) Reaction of CF_2 with $O(^3P)$: Difluoromethylene, $CF_2(\tilde{X}\ ^1A_1$, $\upsilon_1\upsilon_2\upsilon_3$=000 and $\upsilon_1\upsilon_2\upsilon_3$=010) were produced in 193 nm photolysis of dibromofluoromethane (CF_2Br_2) and detected by LIF. Total removal rate constants for reaction of CF_2 + $O(^3P)$ and their vibrational energy dependence were measured. Reaction mechanism and dynamics were elucidated by the results of the experiments and an *ab initio* calculation.

(5) Reaction of NH_2 with NO: Vibrationally excited $NH_2(\tilde{X}\ \upsilon_1\upsilon_2\upsilon_3$=0v0) were produced in 193nm photolysis of ammonia and detected by LIF. The rate constants for the vibrational relaxation were determined at various vibrational levels of NH_2 with some collision partners (CF_4 and N_2). The rate constants for the reaction of $NH_2(\upsilon_1\upsilon_2\upsilon_3$=0v0, v=0,1, and 2) with NO were also determined. Hydroxyl radical, OH, a product of the reaction, was detected in the present experiment and its production yield was determined by original LIF calibration technique. The experimental results indicates that higher vibrational levels of NH_2 are more effective to produce OH.

(6) Integrated profiles method: A new method for the analysis of temporal profiles of reaction products has been developed. Since this method linearize the equations of regression, the various problems and disadvantages of the conventional non-linear analyses is resolved. Not only rate constants for vibrational relaxation but also the nascent vibrational distribution of

products are simultaneously determined by the kinetic analysis because relative detectivities can be obtained by this method. The method was applied to analyze a $O(^1D)$ + NH_3 reaction and its reliability was clearly demonstrated.

References

1. I. Wilhekmy, *Ann. Physik. Chemie* (Poggendorf), 81, 413, 499 (1850)
2. S. Arrhenius, *Z. Phys. Chem.*, **4**, 226 (1889)
3. F. Daniels, and E. H. Johnston, *J. Am. Chem. Soc.*, **43**, 53 (1921)
4. M. Bodenstein, and S. C. Lind, *Z. Phys. Chem.*, **57**, 168 (1907)
5. H. Hartridge, and F. J. W. Roughton, *Proc. Roy. Soc.*, **A104**, 376 (1921)
6. E. Rabinowitch, and H. L. Lehmann, *Trans. Faraday Soc.*, **31**, 689 (1935)
7. J. C. Polanyi, *Acc. Chem. Res.*, **5**, 161 (1972)
8. R. N. Zare, and P. J. Dagdigian, *Science,* **185**, 739 (1974)
9. W. Demtröder, "Laser Spectroscopy," 2nd ed, Springer-Verlag (1982).
10. S. H. Lin, Y. Fujimura, H. J. Neusser, and E. W. Schlag, "Multiphoton Spectroscopy of Molecules," Academic Press (1984).

CHAPTER 2 COLLISION ENERGY DEPENDENCE OF THE OVERALL RATE CONSTANT FOR THE REACTION $NH(a^1\Delta) + HN_3$

2.1 INTRODUCTION

Chemiluminescence is due to the reactions which produce emissive excited states. Such highly reactive species as atoms and radicals are frequently related with the production of the electronically excited states. Chemiluminescence was observed in many reaction systems; nevertheless, most of the mechanisms have not completely been resolved yet. The goal of the present study is not only to make clear the reaction mechanism but also to investigate the effect of a collision energy on a chemiluminescent reaction. Spectroscopic information reveals a source of the emission and a kinetic study gives the reaction mechanism of the chemiluminescence. The visible emission in the HN_3 photolysis system was studied in the present work.

There have been a few reports on the chemiluminescence in the photodissociation of hydrogen azide HN_3. Okabe[1] first observed the emission over the range of 430-800 nm in the photolysis of HN_3 with rare gas lamps (Xe and Kr). He assigned the source of the emission to the transition of N_2 first-positive band ($B^3\Pi_g$–$A^3\Sigma_u^+$). McDonald and co-workers,[2-4] who performed pioneering works on the photolysis of HN_3, observed visible emission in the 266 nm photolysis. They proposed that the emission was due to the transition of $NH_2(\tilde{A}^2A_1$–$\tilde{X}^2B_1)$ only by comparing with its absorption wavelength. They also proposed a reaction $NH(a^1\Delta,v=0) + HN_3 \rightarrow NH_2(\tilde{A}^2A_1) + N_3$ for the mechanism on the basis of the heat of reaction.

Piper et al.[5] observed temporal profiles not only of the visible emission but also of the laser-induced fluorescence (LIF) of $NH(c^1\Pi–a^1\Delta)$. They reported that both profiles were consistent with the mechanism proposed by McDonald et al., although their rate constant was about two times larger than that measured by McDonald et al. The mechanism had been accepted with little doubt since then and no study showed the direct information on the origin of the emission by more reliable spectroscopic technique. The overall rate constant for the reaction $NH(a^1\Delta,v=0) + HN_3$ has also been reported using various techniques;[6-10] however, there have been few studies on the reaction products, particularly on the electronically excited states.

In the present study, a dispersed emission spectrum was observed and assigned to the vibrational band of the $NH_2(\tilde{A}^2A_1–\tilde{X}^2B_1)$ transition. The internal state distribution, however, was not consistent with the reaction mechanism accepted so far. The modified reaction mechanism including internally excited $NH(a^1\Delta)$ is proposed from spectroscopic and kinetic analysis of the emission.

The overall rate constant for the reaction $NH(a^1\Delta) + HN_3$ has been determined using different photolysis wavelengths (266 nm and 193 nm) in the present study and given information on the reaction dynamics. The rate constants were found to be dependent not only on the photolysis wavelength but also on the vibrational levels of the $NH_2(\tilde{A}^2A_1)$ produced in the reaction. The rate constants reduce with an increase in the energy of photodissociation and with a decrease in the vibrational energy of the product $NH_2(\tilde{A}^2A_1)$. The results are rationalized by the generation of centrifugal potential barrier due to the large translational energy of $NH(a^1\Delta)$. The relation between the rate

constant and collision energy will be discussed.

2.2 EXPERIMENT

2.2.1 Apparatus

Experimental apparatus consists of four parts: lasers, gas handling system, detectors, and data acquisition system. The detection system has arranged for three modes of experiments: measurement of dispersed emission, laser fluence dependence of emission intensity, and time profiles of emission.

A. Lasers

Photolysis at two different wavelengths were performed: 266 nm from Nd^{3+}:YAG laser (Continuum YG660-20, 0.2-5 mJ $pulse^{-1}$) and 193 nm from ArF excimer laser (Lambda Physik Lextra-50SL, 5 mJ $pulse^{-1}$). Typical repetition rate was 4-10 Hz. Both laser beams were trimmed with an aperture to 6mm in diameter. The output beams from the YAG laser have three different wavelengths: 1064 nm, 532 nm, and 266 nm. A 60° quartz prism was used to separate the 266 nm light. The laser beam was aligned with two 90° prisms and a 266 nm dichroic mirror. In the experiment of 193 nm photolysis, the beam height was adjusted with two 90° prisms.

B. Flow systems

The cell made of Pyrex has two ports for observation with quartz window of 22 mm in diameter. The cell was evacuated with a rotary pump (ULVAC D-950). The pressure of the sample gas was monitored with a capacitance manometer (Baratron 122AA, full scale 10 Torr). Exhausted gas was cooled

with liquid N_2 at the downstream of the cell to prevent contamination of the oil in the pump. Two types of flow systems were used for two photolysis wavelengths. The laser beam was parallel with gas flow in the experiments with 266 nm, while the 193 nm beam was perpendicular to the gas flow.

C. Dispersed emission spectra

Dispersed emission spectra were observed to identify the source of emission. A schematic diagram of the apparatus is shown in Fig. 2.1. Emission from the observation region was collected through a long-pass filter (Toshiba Y-43) and was focused with a lens (f=80 mm) on the entrance slit of a monochromator (Nikon P-250). Typical scan speed was 5 nm/min and a spectral resolution was 3 nm (FWHM). The signal from a photomultiplier (Hamamatsu R928) mounted on the exit slit was sent to a home-made amplifier (×10) and then fed into a gated integrator (Stanford Research Systems SR-250). The delay of a sampling gate from the laser pulse was 2 μs and its duration was 5 μs. The signals of 30 pulses were averaged. In order to correct for the shot-to-shot laser fluctuations, undispersed emission was focused with a lens (f=60 mm) on another photomultiplier (Hamamatsu 1P28) through a filter (Toshiba O-54) at the opposite side of the monochromator. The signal from the 1P28 was amplified (×10) and inverted with a home-made amplifier and then averaged with a home-made gated integrator. A typical gate delay and width were 1.5 and 3.5 μs, respectively. Input time constant of gated integrator was 100 μs corresponding to a number of average over 30 pulses. Both dispersed and undispersed emission signals were fed into an A/D computer interface (Stanford Research Systems SR-245) and sent to

computer (EPSON PC-286VM) via RS-232C. The data were acquired by a software programmed with N88-BASIC (NEC).

D. Laser fluence dependence of the emission intensity

The laser fluence dependence of the emission intensity was measured to check whether or not multiphoton process occur. The laser fluence was adjusted with a Q-switch delay in the 266 nm photolysis, while the fluence was reduced with a few wire gauze (mesh size 1.5 mm) in the 193 nm photolysis. Relative laser fluence was monitored with photodiode (Hamamatsu S1722-02, biased by -36 V) using reflection with a quartz disk (2.4 mm thickness). The signal from the photodiode was fed into a gated integrator (SR-250) and sent to the computer. Typical conditions of the gated integrator were as follows: gate delay of 340 ns, gate width of 200 ns, and a sampling average was unity. The power of 193 nm laser beam was measured with an internal power monitor attached in the laser itself and the signal from the photodiode was converted to laser fluence. The fluence of 266 nm laser beams could not be measured directly with the joule meter for visible light (Photon control, model 25) but estimated from the difference in the power of 532 nm beam at the best and worst phase-matching angle of the KD*P crystal for the 266nm beam. A dispersed emission was detected with a photomultiplier (R928) at the exit slit of a monochromator whose resolution was 7 nm (FWHM). The signals of photomultiplier were sent to the computer, as described in previous section.

E. Temporal profiles of the emission

The apparatus for observation of temporal profiles of the emissions is also shown in Fig. 2.1. The signal from the photomultiplier was amplified (× 300) and digitized with a home-made transient memory whose time resolution was 40ns. In this experiment, all signal cables were terminated with 50 Ω. Signals of 15000-30000 pulses were averaged to obtain a good S/N ratio. The relative laser fluence was monitored with a photodiode and averaged with a gated integrator to normalize the dispersed emission signal. Data acquisition was the same as that described in the previous section.

2.2.2 Samples

Hydrogen azide, HN_3, was synthesized in vacuo as follows:

1. Sodium azide (NaN_3) of 0.9 g and stearic acid ($C_{17}H_{35}COOH$) of 16 g were put in a 300 cm^3 flask and the air was evacuated with a diffusion pump (ULVAC U-250) for 15 hours.

2. The samples were heated with an oil bath and the temperature was kept at 100±1℃ for 7 hours. The generated gases were collected with a liquid N_2. The trap was evacuated every 30 minutes to remove volatile matter.

3. The crude HN_3 was purified by trap-to-trap distillation. Non volatile compound remains in an ethanol-dry ice slush and the purified HN_3 was collected into a liquid N_2 trap. The gases coming out in the initial and final few minutes were thrown away. The pressure of the HN_3 was monitored with a Pirani gauge during the distillation. Under the steady distillation conditions, the pressure was 0.15 Torr.

4. The purified HN_3 was stored in a 12 dm^3 glass bulb. HN_3 of about

10 Torr was synthesized by the method described here.

Pure HN_3 was used in the experiments. Other gases, He (99.9999 %, Nihon Sanso) and Xe (99.9 %, Takachiho Kagaku Cogyo) were used without further purification.

2.3 RESULTS AND DISCUSSION

2.3.1 Spectroscopic Study

Figure 2.2 shows a dispersed emission spectrum that was observed in the 266 nm photolysis of HN_3. Significant progression appears along with a broad background. Since the overall sensitivity of the detection system was not corrected, the decrease in the intensity at longer wavelengths does not show the correct intensity distribution but reflects the sensitivity of the detection system. Moreover, the filter used (Toshiba Y-43) was transparent only at longer wavelength than 420nm; the onset of the spectrum at short wavelength is due to the transmission of the filter. Most of the peaks were assigned to the transition $NH_2(\tilde{A}^2A_1(0,v_2',0)-\tilde{X}^2B_1(0,0,0))$. The broad background results from rotational excitation of $NH_2(\tilde{A}^2A_1)$ and/or congestion of many weak vibronic sub-bands.[11-13] The spectrum shows the excitation of the ν_2-bending vibrational levels up to at least $v_2'=15$. Figure 2.3 shows a dispersed emission spectrum in the HN_3/193 nm photolysis recorded under the same detection system. The envelope of the spectrum is very similar to that of 266 nm photolysis and the peaks can also be assigned to the transition of $NH_2(\tilde{A}^2A_1-\tilde{X}^2B_1)$.

The spectra observed with 266 nm and 193 nm are essentially the same each other. The fact suggests that the temporally averaged vibrational

distributions are not different in both photolyses.

McDonald et al.[2-4] proposed that $NH_2(\tilde{A}^2A_1)$ was produced in the reaction $NH(a^1\Delta,v=0) + HN_3 \rightarrow NH_2(\tilde{A}^2A_1) + N_3$. The maximum vibrational quantum number can be estimated from the heats of formation of all species related to the reaction on the assumption that all the exothermicity of the reaction is deposited into NH_2. The $\Delta H^\circ_{f,0}$ values, for $HN_3(\tilde{X}\ ^1A')$, $NH(X^3\Sigma^-)$, and $NH_2(\tilde{X}^2B_1)$ have been determined precisely: 300.5±0.3 kJ mol^{-1};[14] 357±1 kJ mol^{-1};[15] 192±1 kJ mol^{-1},[15] respectively. The 0-0 transition energies are known for $NH(a^1\Delta-X^3\Sigma^-)$ and $NH_2(\tilde{A}^2A_1-\tilde{X}^2B_1)$: 12589 cm^{-1};[16] 10249 cm^{-1}.[17] For N_3, unfortunately, an accurate heat of formation is not available. Although $\Delta H^\circ_{f,0}(N_3)$ = 417±21 kJ mol^{-1} [18] has been adopted for a long time, recent reliable reports using various techniques recommended higher values: 469±21 kJ mol^{-1} from ion cyclotron resonance of N_3^-;[19] <475.3 kJ mol^{-1} in the study of the reaction $F + HN_3 \rightarrow HF(v\leq4) + N_3$;[20] 457.1 kJ mol^{-1} from quantum-mechanical calculation;[21] 451.5 kJ mol^{-1} from the dissociation energy of $H-N_3$ bond.[22] These values give the maximum vibrational quantum number $v_2'_{max}$ = 0-5, <2, 4, and 5, respectively. Therefore, the production of highly excited vibrational levels at lowest $v_2'\geq10$ of $NH_2(\tilde{A}^2A_1)$ cannot be ascribed to only the reaction between $NH(a^1\Delta,v=0)$ and HN_3.

There is another mechanism for the production of the $NH_2(\tilde{A}^2A_1-\tilde{X}^2B_1)$ emission under the presence of HN_3. Kajimoto et al.[23] observed the emission from NH_2 produced in the reaction $H + HN_3 \rightarrow NH_2(\tilde{A}^2A_1, v_2'\leq15) + N_2$. The observed vibrational distribution of $NH_2(\tilde{A}^2A_1)$ was different from the present experiment in spite of the same optical devices were used (Fig. 2.4). Furthermore, the order of rate constant for the production of $NH_2(\tilde{A}^2A_1)$

obtained the present experiment was the same of $NH(a^1\Delta) + HN_3$ reaction. Hence, the hydrogen atom cannot be a candidate for production of $NH_2(\tilde{A}^2A_1)$ react with HN_3.

Since the rotational motion of nascent $NH(a^1\Delta)$ produced in the uv photolysis is not highly excitated at any wavelength,[24] there are two possible sources to produce the high vibrational levels of $NH_2(\tilde{A}^2A_1)$ in the reaction. One is a vibrational energy and the other is a translation energy of $NH(a^1\Delta)$. There have been many works on the energy partitioning in the $NH(a^1\Delta)$ produced in the HN_3 photolysis,[10,25-30] whereas the vibrational distribution of nascent $NH(a^1\Delta,v)$ is still a matter of controversy. Nelson and McDonald[25] have reported the energy partition in the HN_3 photolysis at 266 nm. According to their summary, the vibrational distribution of nascent $NH(a^1\Delta,v)$ is 1.0/(1.1±0.3)/(0.8±0.3)/(0.9±0.5) for v=0/1/2/3. Hawley et al.[26], however, have recently reported a totally different distribution: 1.0/0.3/0.02 for v=0/1/2. These data were obtained in the same laboratory; the reason for the discrepancy is unclear. The 193 nm photolysis has not been concluded, either. Misra and Dagdigian[28] reported the vibrational distribution to be 1.0/(0.66±0.05)/(0.09±0.05) for v=0/1/2. Bohn and Stuhl[29], on the other hand, reported more highly excited distribution: 1.0/(0.48±0.11)/(0.21±0.07)/(0.13±0.05) for v=0/1/2/3.

A translational energy of $NH(a^1\Delta)$, on the other hand, has been determined by Nelson and McDonald[25] to be 6000-7000 cm^{-1} from Doppler-broadening in the 266 nm photolysis. Rohrer and Stuhl[30] have reported that the nascent $NH(a^1\Delta)$ has a translational energy of 26000 cm^{-1} in the 193 nm photolysis.

The emission spectra observed in the 266 nm and 193 nm photolysis are almost the same in the present study. If translational energy is effective to produce highly excited $NH_2(\tilde{A}^2A_1)$, there must be a difference in the spectra owing to the large difference in the translational energy of $NH(a^1\Delta)$ colliding with HN_3. Thus we tentatively conclude that the vibrational energy in the $NH(a^1\Delta)$ is more effective to produce highly excited $NH_2(\tilde{A}^2A_1)$ than the translational energy.

Time resolved emission intensity should be observed to obtain information on the difference in kinetics.

2.3.2 Kinetic Study

In the photolysis at 266 nm, a laser fluence dependence and temporal profiles of dispersed emission were measured at 520, 600 and 660 nm, where the emissions were due mainly to the transitions from $NH_2(\tilde{A}^2A_1)$ v_2'=12, 9, and 7 to $\tilde{X}^2B_1$ v_2''=0, respectively. The emission intensities are linearly dependent on the laser fluence irrespective of the observation wavelengths (See Fig. 2.5). Linear dependence does not necessarily correspond to a one-photon process because two-photon process shows the first-order dependence if the first excitation is not effective and there is no process competing with the second absorption. This is not the case because HN_3 on the upper potential undergoes fast predissociation.[31] Consequently, the dependence observed shows that an only photon is associated with the production of single $NH_2(\tilde{A}^2A_1)$ molecule.

In the photolysis at 193 nm, the emission of $NH_2(\tilde{A}^2A_1–\tilde{X}^2B_1)$ was observed at 520, 600 and 630 nm, where the emission due to the transitions

from the v_2'=12, 9, and 8 levels of $NH_2(\tilde{A}^2A_1)$ state. Typical profiles observed are shown in Fig. 2.6. The emission intensity also varied linearly with laser fluence as the same as that observed in the 266 nm photolysis.

Since the emission intensity shows rise and decay (Fig. 2.6) and $NH_2(\tilde{A}^2A_1)$ produced in the system decays through radiation to the ground state and the reaction by HN_3, the reaction mechanism can be written as follows:

$HN_3 + h\nu(uv)$	$\rightarrow NH(a^1\Delta) + N_2$	(1)
$NH(a^1\Delta) + HN_3$	$\rightarrow NH_2(\tilde{A}^2A_1) + N_3$	(2a)
$NH(a^1\Delta) + HN_3$	$\rightarrow$ products	(2b)
$NH(a^1\Delta)$	$\rightarrow$ radiation, diffusion	(3)
$NH_2(\tilde{A}^2A_1) + HN_3$	$\rightarrow$ products	(4)
$NH_2(\tilde{A}^2A_1)$	$\rightarrow NH_2(\tilde{X}^2B_1) + h\nu'$(visible),	(5)

where the "products" denotes all the possible species produced in quenching and/or reactions. It should be noted that a faster process always governs the rise and a slower one relates to the fall (Fig. 2.6). In the present experiment, the rise must be related to deactivation of $NH_2(\tilde{A}^2A_1)$ because of its extraordinary large quenching rate constant,[32,33] for example, 1.45×10^{-10} cm^3 $molecule^{-1}$ s^{-1} even by helium and short radiative lifetime k_5 = 1.0×10^5 s^{-1}.[32,34] Accordingly, the fall corresponds to the overall decay of the reactions $[k_2(=k_{2a}+k_{2b})]$ for $NH(a^1\Delta) + HN_3$ and radiation or diffusion (k_3) of $NH(a^1\Delta)$.

The absorption cross-sections of HN_3 at 266 nm and at 193 nm are 7.4×10^{-20} cm^2 and 1.7×10^{-18} cm^2, respectively.[31] From the laser fluences and the sizes of the laser beams, the densities of photons at 266 nm and 193 nm

were estimated to be 3.6×10^{15} and 1.3×10^{15} photons cm^{-2}. The ratios of the initial concentration of $NH(a^1\Delta)$ to that of HN_3 are about to be 2.0×10^{-4} at 266 nm photolysis and 2.1×10^{-2} in the 193 nm photolysis with the quantum yield for the formation of $NH(a^1\Delta)$.[35] Therefore, the pseudo-first-order reaction conditions are always satisfied in both the reactions (3) and (5), thus there is little change in the concentration of HN_3 during the reaction.

In addition to the double-exponential fitting, the Simplex optimization method coupled with the Runge-Kutta-Gill numerical integration of the rate equations was adopted in the analysis of the temporal profiles. The overall rate constants $k_2(=k_{2a}+k_{2b})$ measured at different wavelengths are $k_2(520nm) = (1.2\pm0.1)\times10^{-10}$, $k_2(600nm) = (0.97\pm0.1)\times10^{-10}$, and $k_2(660nm) = (0.84\pm0.1)\times10^{-10}$ cm^3 $molecule^{-1}$ s^{-1} for the 266 nm photolysis and $k_2(520nm) = (0.92\pm0.2)\times10^{-10}$, $k_2(600nm) = (0.61\pm0.2)\times10^{-10}$, and $k_2(630nm) = (0.35\pm0.2)\times10^{-10}$ cm^3 $molecule^{-1}$ s^{-1} for 193 nm photolysis as listed in Table 1. The errors denote 2σ in the analysis. The order of the rate constants is the same of that of the NH(a) $+HN_3$ reaction recently measured by LIF of $NH(c^1\Pi-a^1\Delta)$ [$(1.2\pm0.2)\times10^{-10}$ cm^3 $molecule^{-1}$ s^{-1}][8] and much different from that for H + $HN_3\rightarrow$ $NH_2(\tilde{A}^2A_1)$ + N_2 reaction (1.1×10^{-14} cm^3 $molecule^{-1}$ s^{-1}).[36] Therefore, the $NH_2(\tilde{A}^2A_1)$ is produced by the reaction $NH(a^1\Delta)$ + HN_3 in the uv photolysis as described in previous section.

The dependence of the first-order decay rate on the pressure of buffer gas (He and Xe) was measured in the study on the 266 nm photolysis (Fig. 2.7). The temporal profiles of the emission were observed through a cut-off filter (Toshiba R-61) which is transparent for the light longer than 610 nm. Thus, the emission observed was mainly due to the transition from $NH_2(\tilde{A}^2A_1$,

$v_2'<8$). Since Xe is known to be a fast quencher of $NH(a^1\Delta)$ (1.28×10^{-11} cm^3 $molecule^{-1}$ s^{-1}),[28,37-39] the apparent first-order decay rate should increase under the presence of Xe. On the other hand, He has much less effective quencher ($<1\times10^{-15}$ cm^3 $molecule^{-1}$ s^{-1}),[10] and can hardly affect the decay rate. Figure 2.7 shows the dependence of the first-order decay rate on the pressure of the buffer gas. The first-order decay rate is affected by Xe but little by He. Since the dependence was measured with low time resolution (1 μs) under the static conditions, the data shows a qualitative result. Nevertheless, the difference between Xe and He also supports the mechanism that the $NH_2(\tilde{A}^2A_1)$ is produced by the reaction between $NH(a^1\Delta)$ and HN_3.

Hack and Mill[10] have shown that the overall rate constants for the reaction $NH(a^1\Delta,v=0\text{-}2)$ + HN_3 have little dependence on the vibrational levels of $NH(a^1\Delta)$. On the other hand, the rate constants k_2 obtained by the emission of $NH_2(\tilde{A}^2A_1-\tilde{X}^2B_1)$ in the present study show an apparent dependence on the wavelengths at which the emission was observed (Table 1).

The overall rate constants obtained for the reaction $NH(a^1\Delta)$ + HN_3 apparently depend on the photolysis wavelength. The rate constants in the 193 nm photolysis are smaller than those in the 266 nm photolysis. Since no buffer gas was used in the present study, the translational energy of $NH(a^1\Delta)$ is not relaxed until the first collision with HN_3. Therefore, collision energies for the $NH(a^1\Delta)$ + HN_3 reaction are very different between the 266 nm and the 193 nm photolysis: translational energy of the nascent $NH(a^1\Delta)$ is 6000-7000 cm^{-1} [25] and 26000 cm^{-1} [30] in the 266 nm and 193 nm photolysis, respectively. The overall rate constant of the reaction $NH(a^1\Delta)$ + HN_3 determined by $NH(c^1\Pi-a^1\Delta)$ LIF was independent of temperature,[40] hence the

reaction proceeds with no barrier. However, the apparent decrease in the rate constants was shown in the present study with an increase in the translational energy. Note that buffer gas of about 10-20 Torr was added in the LIF experiment and that no buffer gas was used in the present experiment. Since the $NH(a^1\Delta)$ has a large translational energy without buffer gas, the centrifugal potential barrier on the reaction coordinate must be taken into account.

Relation between reaction rate constant and collision energy is expressed by the next equation [Eq. (A-5) in Appendix]:[41]

$$k \propto E_T^{(s-4)/2s},$$

where E_T is a collision energy of the system and s is a parameter in the function of the potential ($V(R) \propto -1/R^s$). The overall rate constants in the present study decrease with an increase in the translational energy (Table 1); as a result, the parameter s for the potential energy at long distance must be less than 4. Potential energies whose radial distributions are consistent with our result ($2<s<4$) are those for charge-quadrupole ($s=3$) and dipole-dipole interactions ($s=3$) in a specific intermolecular orientation. No electrostatic interactions have the dependence, $2<s<4$, when being averaged over possible orientation under Boltzmann distribution. Since there is no charged reactants, the $NH(a^1\Delta)$ + HN_3 reaction system is governed mainly by dipole-dipole interaction at a specific orientation of the molecules. Hydrogen azide HN_3 has relatively large dipole moment: μ_a=0.84 and μ_b=1.48 Debey, where μ_a and μ_b denote the dipole moments along principle axes of inertia. Although the dipole moment of $NH(a^1\Delta)$ has not been reported, the ground

state $NH(X^3\Sigma^-)$ has μ=0.98 Debye. Accordingly, it can be concluded that the interaction potential between $NH(a^1\Delta)$ and HN_3 is mainly governed by the dipole-dipole interaction.

The overall rate constants for the reaction $NH(a^1\Delta)$ + HN_3 depends not only on the photolysis wavelength but also on the observation wavelength. As seen in Table 1, the smaller rate constants are obtained at longer observation wavelengths. The difference is more apparent in the 193 nm photolysis than that in the 266 nm photolysis. In other words, a large translational energy suppresses the production of lower vibrational states of $NH_2(\tilde{A}^2A_1)$. There has been no information as to whether the reaction goes through a complex mechanism or a direct mechanism in terms of the reaction dynamics. It is reasonable that the period of interaction is short in the collisions with high translational energy. If the structure of H-N-H cannot relax to quasi-linear configuration during the interaction time, $NH_2(\tilde{A}^2A_1)$ with low vibrational energy is not likely to be produced. (The equilibrium structure is quasi-linear ($\angle$HNH=144° in the $\tilde{A}^2A_1$ state and bent in the $\tilde{X}^2B_1$ state.)[42] Further experiments are needed into the problem, for example, the decay of $NH(a^1\Delta)$ produced by the photolysis without buffer gas must be directly measured.

2.4 CONCLUSION

The visible emission following the ultraviolet photolysis of HN_3 originates from the vibronically excited $NH_2(\tilde{A}^2A_1)$. All the vibrational levels of $NH_2(\tilde{A}^2A_1)$ are produced in the reaction of $NH(a^1\Delta)$ with HN_3, and highly vibrationally excited $NH_2(\tilde{A}^2A_1)$ is produced from vibrationally excited $NH(a^1\Delta)$.

From the measurement of the photolysis wavelength dependence of the overall rate constants for the reaction $NH(a^1\Delta)$ + HN_3, a long-range potential between the reactants was determined to be the form:

$$V(R) = -\frac{C}{R^s}, \qquad (2<s<4, \quad C: \text{constant})$$

The value of s indicates that the potential between reactants at long distance is mainly governed by the dipole-dipole interaction. The overall rate constants for the reaction $NH(a^1\Delta)$ + HN_3 depend also on the observed wavelengths, which suggests that $NH_2(\tilde{A}^2A_1)$ with low vibrational energy is not likely to be produced when $NH(a^1\Delta)$ has large translational energy.

2.5 APPENDIX

2.5.1 Translational energy dependence of the reaction cross section.

The relation between rate constant and collision energy is derived according to the formulation in ref. 41. The total energy E_T of the reaction system is expressed by

$$E_T = \frac{1}{2}\mu\dot{R}^2 + \frac{E_T\, b^2}{R^2} + V(R), \qquad \text{(A-1)}$$

where μ denotes reduced mass, R distance between colliding molecules, b impact parameter, and $V(R)$ potential energy. An effective potential $V_{eff}(R)$ is defined by the sum of the potential energy and the centrifugal energy:

$$V_{eff}(R) = V(R) + \frac{E_T\, b^2}{R^2}. \qquad \text{(A-2)}$$

Since the reaction $NH(a^1\Delta)$ + HN_3 has no threshold energy, the only barrier during approach of the reactants is the centrifugal barrier due to the large translational energy of $NH(a^1\Delta)$.

A parameter b_{max} is defined as the maximum impact parameter with which colliding molecules can approach within R_{max}. R_{max} is the distance where the centrifugal barrier takes its maximum. It is now defined that the reaction occurs whenever the radial distance R is smaller than R_{max}. A rate constant k is expressed by the product of the reaction-cross section and the relative velocity:

$$k = \sigma_R\, u = \pi b_{max}^2\, u. \qquad \text{(A-3)}$$

Large rate constant (1.2×10^{-10} cm^3 $molecule^{-1}$ s^{-1}) for the reaction $NH(a^1\Delta)$ + HN_3 corresponds to a large reaction cross section. The fact means that the reactants interact even at long distance and the initial stage of the reaction is governed by a long-range attractive force. The potential between

the reactants can be assumed to be the form:

$$V(R) = -\frac{C}{R^s}, \qquad \text{(A-4)}$$

The rate constant is expressed by

$$k = \pi\, q(s)\; C^{1/2} \left(\frac{2}{\mu}\right)^{2/s} E_T^{\,(s-4)/2s}. \qquad \text{(A-5)}$$

where s and C are constants.

$$q(s) = (s/2)[(s-2)/2]^{-(s-2)/s}. \qquad \text{(A-6)}$$

2.5.2 Kinetic data analysis

The emission intensity showed a sharp rise and slow decay immediately after the photolysis (Figure 2.6). The first-order rate constant was obtained by the double-exponential non-linear least-squares fit coupled with the simplex method. The reaction rate constant was determined by the weighted least squares fit for the measured first-order rate constants.

A. The form of double-exponential in the temporal profiles of the emission

The rise and decay indicate that the emissive species is a reaction intermediate. Thus, a reaction scheme can be simply constructed as follows:

$$A \xrightarrow{ka} B \xrightarrow{kb} C \qquad \text{(A-7)}.$$

A is a species initially produced in the photolysis and B is an emissive species observed. If the pseudo-first-order conditions are satisfied in the reactions, the time dependence of B is expressed by the next equation:

$$[B] = \frac{k_a[A]_0}{k_a - k_b}\left(e^{-k_b t} - e^{-k_a t}\right) \qquad \text{(A-8)}.$$

where $[A]_0$ denotes the initial concentration of the species A. The equation shows that the time dependence of B is double exponential. If A and B has another depletion path, the reaction scheme (A-7) is modified as shown next:

$$\begin{aligned} &A \xrightarrow{ka} B \xrightarrow{kb} C \\ &A \xrightarrow{ka'} D \\ &B \xrightarrow{kb'} F \end{aligned} \qquad \text{(A-7')},$$

the time dependence of B is expressed by

$$[B] = \frac{k_a[A]_0}{(k_a + k_{a'}) - (k_b + k_{b'})}\left(e^{-(k_b+k_{b'})t} - e^{-(k_a+k_{a'})t}\right) \qquad \text{(A-8')}.$$

As seen from equation (A-8'), the overall decay rate $k_a+k_{a'}$ for A can be obtained from the time dependence of B. The faster process always corresponds to the rise and the slower one relates to the decay part in equation (A-8'). If $k_b+k_{b'}$ is larger than $k_a+k_{a'}$, the time dependent term associated with $k_b+k_{b'}$ corresponds to the rise and the term having $k_a+k_{a'}$ is related to the decay. If $k_b+k_{b'}$ is smaller than $k_a+k_{a'}$, all the correspondence should be reverse.

In the present study, fitting was done by a software "NLLSQ4" programmed with PRO-FORTRAN77 to be a form expressed by

$$[B]_t = A_d \exp(-k_d t) - A_r \exp(-k_r t),$$

A is a constant and the subscripts denote which constant is related to rise and decay, respectively. In the present study, k_r and k_d are defined as follows:

$$\begin{aligned} k_r &= k_4[HN_3] + k_5 \\ k_d &= k_2[HN_3] + k_3 \end{aligned},$$

where k_2, k_3, k_4 and k_5 are defined in section 2.3.2.

B. Kinetic data analysis by SRKG fit

In addition to the double-exponential fitting, the Simplex method coupled with the Runge-Kutta-Gill integration method (SRKG fit) was applied. The procedures of the calculation of the rate constants are as follows:

1. A reaction scheme and rate equations were given, for example, by the equations (3)-(6) in section 2.3.2.

2. The appropriate rate constants roughly obtained by the double-exponential analysis were used as the initial parameters. The differential equations were numerically integrated by the Runge-Kutta-Gill method.

3. The squared difference between the calculated and the observed profiles were summed.

4. When the sum of squared residual was smaller than the tolerance, the parameters used for integration were adopted for the first-order rate constants.

The procedure 2 and 3 were repeated until the difference between calculation and observation is smaller than the tolerance.

The sensitivities of the fitting parameters were checked. The sensitivity indicates which parameter is most concerned with the change of the concentration of the observed species. The rate constant with higher sensitivity is determined more precisely. The procedure for checking the sensitivity was as follows:

1. One of the rate constants obtained by the fitting was changed by 10 %. The rate equation was numerically integrated using a new set of the rate constants for the reaction mechanism and the original set of the rate constants.

2. The sum of the squared residual was compared between the calculated data and the observed data.

3. The procedure 1. and 2. were repeated for each rate constant.

The difference of the sum of squared residual calculated with and without change of the rate constant was defined to be sensitivity. The most sensitive rate constant had the largest difference.

The rate constants of the elementary reaction is determined by weighted least-squares fit of the first-order rate constants. The weight are estimated as follows:

1. The error of mean square σ_i is estimated for the measured first-order rate constants, that is,

$$\sigma_i = \sqrt{\frac{F_i}{(n_i - 1)}} \quad .$$

The subscript i denotes the turn of i th measurement, F_i is the minimum of the sum of the squared residual in the SRKG fit and n_i is the number of the analysis points.

2. The squared ratio of the minimum error σ_{min} and each σ_i is defined as weight P_i, that is,

$$P_i = \left(\frac{\sigma_i}{\sigma_{min}}\right)^2 .$$

The errors of mean square σ for the rate constants is estimated by the normal statistical treatments using the weight. The error σ is expressed by

$$\sigma = \sqrt{\frac{\sum_i P_i \left(\bar{k} - k_i\right)^2}{n-1}} ,$$

$\bar{k}$ is the mean value of the rate constant, and n is the number of the

measurement. In the present study, the errors of the rate constants were expressed by 2σ.

REFRENCES

1. H. Okabe, *J. Chem. Phys.* **49**, 2726 (1968).
2. J. R. McDonald, R. G. Miller, and A. P. Baronavski, *Chem. Phys. Lett.* **51**, 57 (1977).
3. A. P. Baronavski, R. G. Miller, and J. R. McDonald, *Chem. Phys.* **30**, 119 (1978).
4. J. R. McDonald, R. G. Miller, and A. P. Baronavski, *Chem. Phys.* **30**,133 (1978).
5. L. G. Piper, R. H. Krech, and R. L. Taylor, *J. Chem. Phys.* **73**, 791 (1980).
6. F. Rohrer and F. Stuhl, *Chem. Phys. Lett.* **111**, 234 (1984).
7. J. W. Cox, H. H. Nelson, and J. R. McDonald, *Chem. Phys.* **96**, 175 (1985).
8. W. Hack and A. Wilms, *Z. Phys. Chem.* **161**, 107 (1989).
9. F. Freitag, F. Rohrer, and F. Stuhl, *J. Phys. Chem.* **93**, 3170 (1989).
10. W. Hack and Th. Mill, *J. Phys. Chem.* **95**, 4712 (1991).
11. K. Dressler and D. A. Ramsay, *Phil. Trans. Roy. Soc.*(London) **A251**, 553 (1959).
12. S. C. Ross and F. W. Briss, M. Vervloet, and D. A. Ramsay, *J. Mol. Spectrosc.* **129**, 436 (1988).
13. F. W. Birss, M. -F. Merienne-Lafore, D. A. Ramsay, and M. Vervloet, *J. Mol. Spectrosc.* **85**, 493 (1981).
14. D. D. Wagman, W. H. Evans, V. B. Parker, R. H. Schumm, I. Halow, S. M. Bailey, K. L. Churney, and R. L. Nuttall, *J. Phys. Chem. Ref. Data* **11** Suppl.2 (1982).
15. W. R. Anderson, *J. Phys. Chem.* **93**, 530 (1989).

16. K. P. Huber and G. Herzberg, *Molecular spectra and molecular structure, Vol.4. Constants of diatomic molecules* (Van Nostrand Reinhold, New York, 1979).

17. G. Herzberg, *Molecular spectra and molecular structure, Vol.3. Electronic spectra and electronic structure of polyatomic molecules* (Van Nostrand Reinhold, New York, 1966).

18. T. C. Clark and M. A. A. Clyne, *Trans. Faraday. Soc.* **66**, 877 (1970).

19. M. J. Pellerite, R. L. Jackson, and J. I. Brauman, *J. Phys. Chem.* **85**, 1624 (1981).

20. J. Habdas, S. Wategaonkar, and D. W. Setser, *J. Phys. Chem.* **91**, 451 (1987).

21. J. M. L. Martin and J. P. François, *J. Chem. Phys.* **93**, 4485 (1990).

22. T. Haas, K. -H. Gericke, C. Maul, and F. J. Comes, *Chem. Phys. Lett.* **202**, 108 (1993).

23. O. Kajimoto, T. Kawajiri and T. Fueno, *Chem. Phys. Lett.* **76**, 315 (1980)

24. K. -H. Gericke, T. Haas, M. Lock, R. Theinl, and F. J. Comes, *J. Phys. Chem.* **95,** 6104 (1991).

25. H. H. Nelson and J. R. McDonald, *J. Chem. Phys.* **93**, 8777 (1990).

26. M. Hawley, A. P. Baronavski, and H. H. Nelson, *J. Chem. Phys.* **99**, 2638 (1993).

27. W. Hack and Th. Mill, *J. Phys. Chem.* **97**, 5599 (1993).

28. D. P.-Misra and P. J. Dagdigian, *J. Chem. Phys.* **97**, 4871 (1992).

29. B. Bohn and F. Stuhl, *J. Phys. Chem.* **97**, 4891 (1993).

30. F. Rohrer and F. Sthul, *J. Chem. Phys.* **88**, 4788 (1988).

31. J. R. McDonald, J. W. Rabalais, and S. P. McGlynn, *J. Chem. Phys.* **52**, 1332 (1970).

32. J. B. Halpern, G. Hancock, M. Lenzi, and K. H. Welge, *J. Chem. Phys.* **63**, 4808 (1975).

33. I. J. Wysong, J. B. Jeffries, and D. R. Crosley, *J. Chem. Phys.* **93**, 237 (1990).

34. S. Koda, *Bull. Chem. Soc. Jpn.* **50**, 1683 (1977).

35. K. -H. Gericke, M. Lock, and F. J. Comes, *Chem. Phys. Lett.* **186**, 427 (1991).

36. G. Le Bras and J. Combourieu, *Int. J. Chem. Kinetics.* **5**, 559 (1973).

37. H. H Nelson, J. R. McDonald, and M. H. Alexander, *J. Phys. Chem.* **94**, 3291 (1990).

38. W. Hack and A. Wilms, *J. Chem. Phys.* **93**, 3540 (1989).

39. W. Hack and K. Rathmann *J. Phys. Chem.* **96**, 47 (1992).

40. W. Hack and K. Rathmann, *J. Phys. Chem.* **94**, 3636 (1990).

41. R. D. Levine and R. B. Bernstein, *Molecular Reaction Dynamics and Chemical Reactivity* (Oxford University Press, New York, 1987), Chap. 2, pp. 58-59.

42. R. N. Dixon, S. J. Irving, J. R. Nightingale, and M. Vervloet, *J. Chem. Soc. Faraday Trans.* **87**, 2121 (1991).

Table 1. The overall rate constants for the reaction $NH(a^1\Delta)$ + HN_3 determined by the analysis of temporal profiles of the emission from $NH_2(\tilde{A}^2A_1)$. The rate constants are in units of 10^{-10} cm^3 $molecule^{-1}$ s^{-1}. The errors denote 2σ.

Photolysis wavelength	Observed wavelength			
	520nm	600nm	630nm	660nm
266nm	1.2 ± 0.1	0.97 ± 0.1	-	0.84 ± 0.1
193nm	0.92 ± 0.2	0.61 ± 0.2	0.35 ± 0.2	-

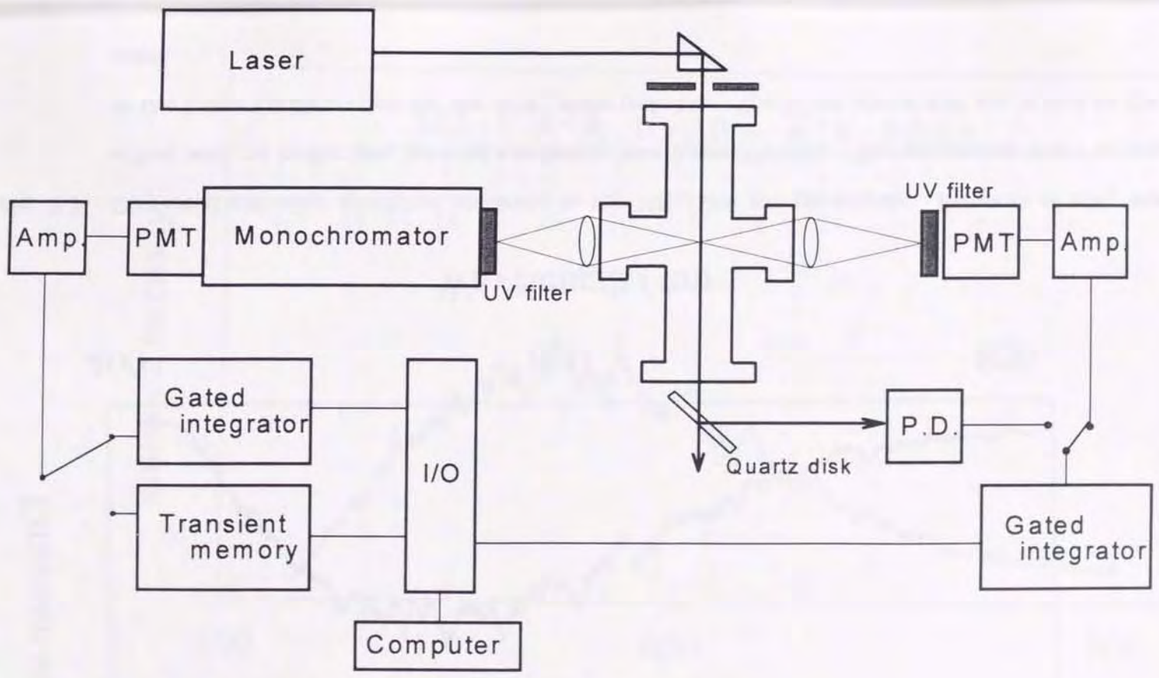

Fig. 2.1. A schematic diagram of experimental apparatus.

I/O : computer interface. Amp. : home made Op-amplifier.
PMT : photomultiplier. P.D. : photodiode.

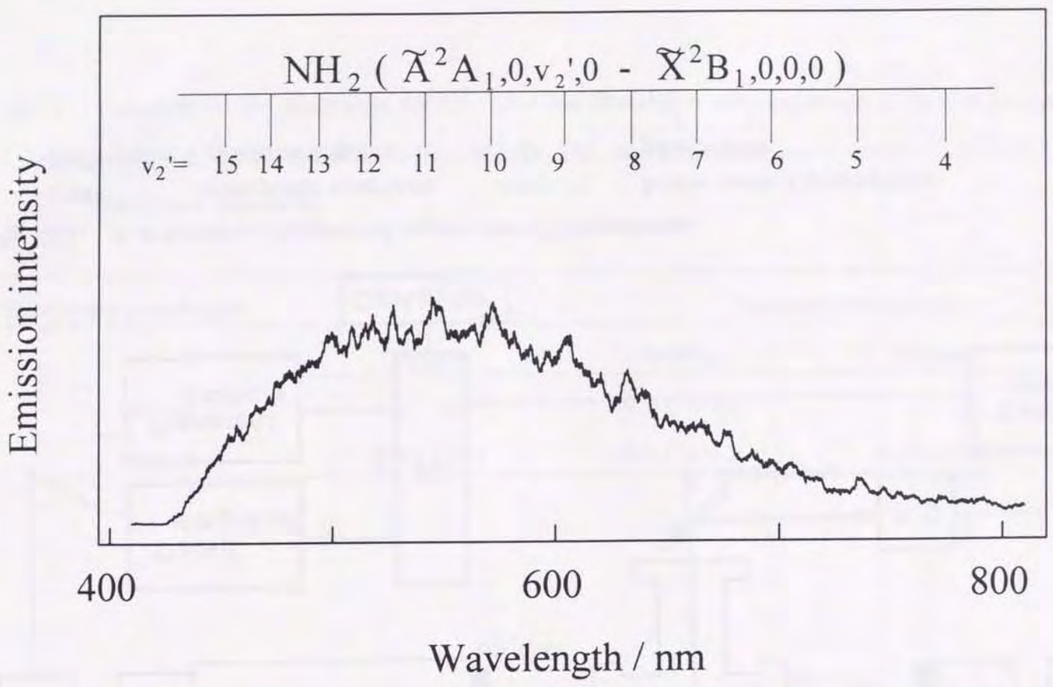

Fig. 2.2. Dispersed emission spectrum observed in the HN_3/266 nm photolysis. Pressure of HN_3 was 150 mTorr with no buffer gas; spectral resolution was 3 nm (FWHM). The assignments are appropriate to the linear configuration for the $\tilde{A}^2A_1$ state (ref. 11). The onset about 420 nm is due to the filter used.

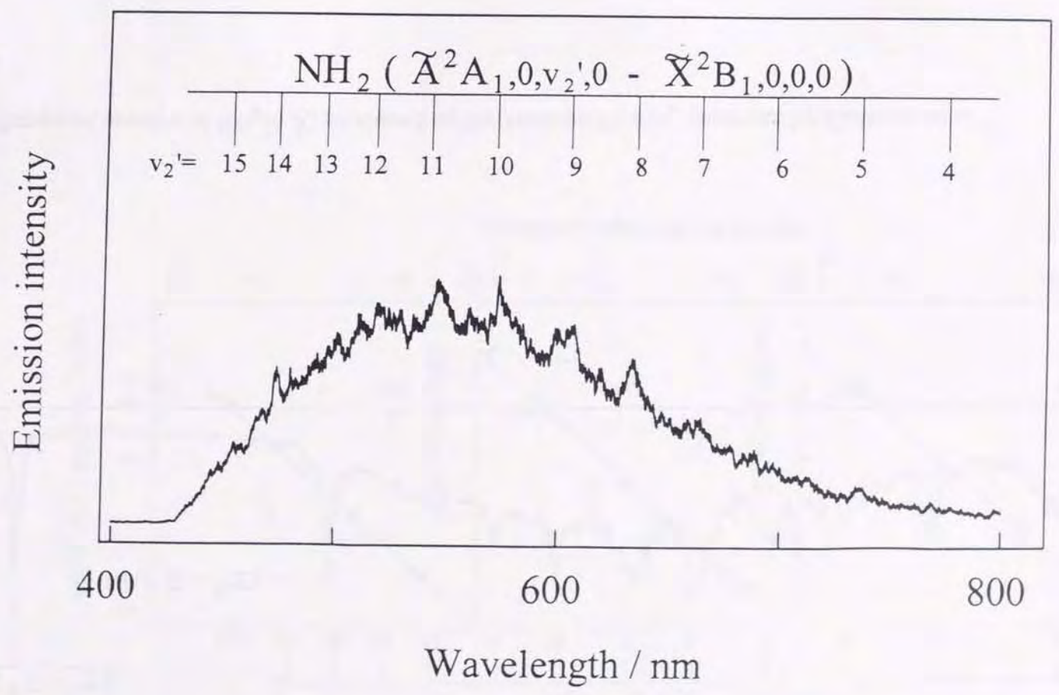

Fig. 2.3. Dispersed emission spectrum observed in the HN_3/193nm photolysis. The pressure of HN_3 was 18 mTorr with no buffer gas; the spectral resolution was 3 nm (FWHM).

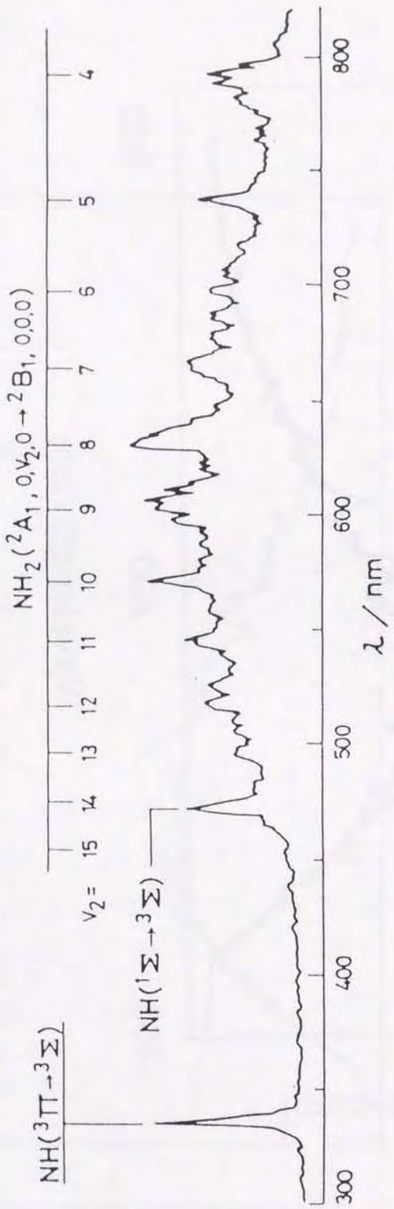

Fig. 2.4. Emission spectra of $NH_2(\tilde{A}\text{-}\tilde{X})$ produced in the reaction H+HN_3 observed by Kajimoto *et al.*[23].

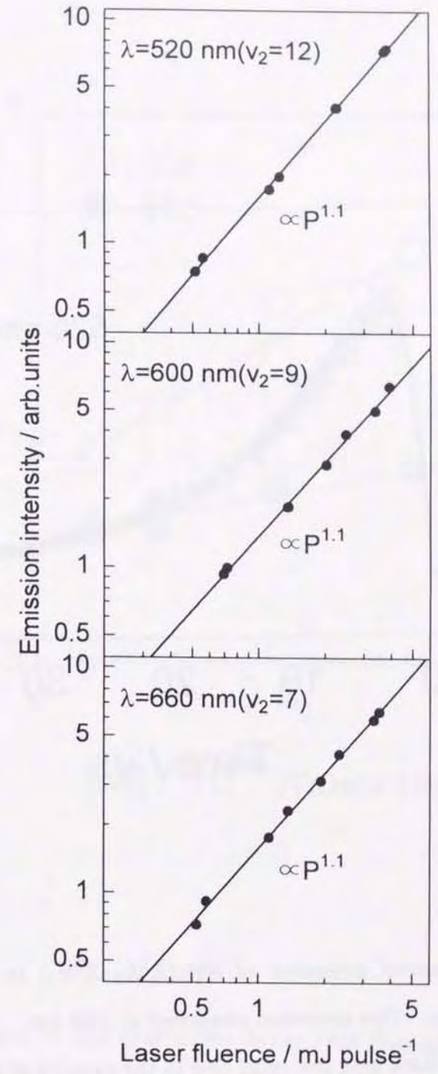

Fig. 2.5. Laser fluence dependence of the emission intensity in the 266 nm photolysis. The pressure of HN_3 was 150 mTorr

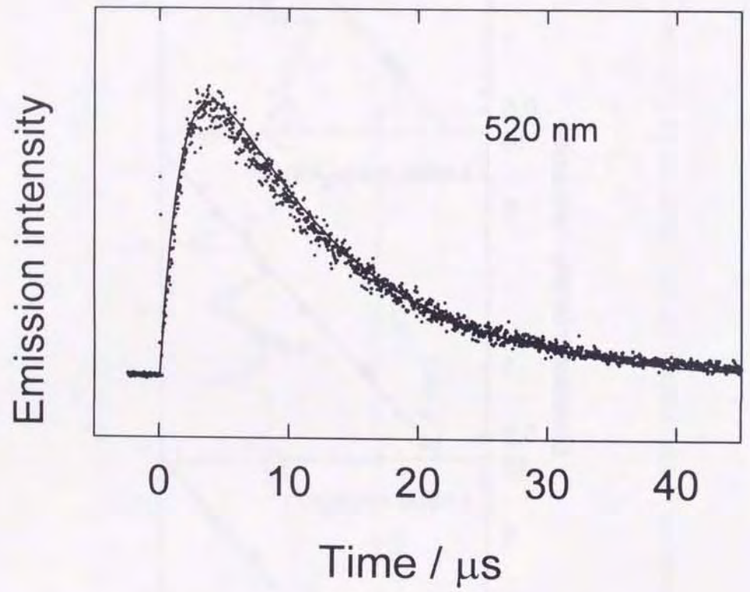

Fig. 2.6. Time resolved emission of $NH_2(\tilde{A}^2A_1-\tilde{X}^2B_1)$ in the HN_3/193 nm photolysis. The emission observed at 520 nm. The dot denote the observed data and the solid line is the results of SRKG fit.

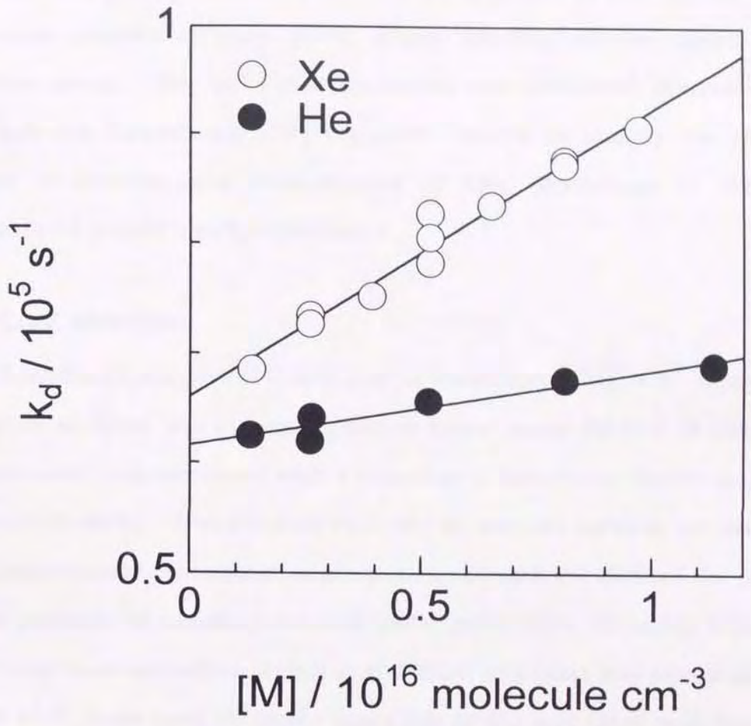

Fig 2.7. Dependence of the first-order decay rate (k_{decay}) on the buffer gas pressure (P_M). Pressure of HN_3 was 20 mTorr. The time resolution was 1μs. Closed circle ● denotes the results of He and open circle ○ denotes the effect of Xe.

CHAPTER 3 EXPERIMENTAL APPARATUS

Common parts in all the experiments are described in this chapter. The apparatus consists of three parts; a gas handling system, lasers, and detection system. Two types of measurement were performed: observation of laser-induced fluorescence (LIF) excitation spectra to identify the radical species of interest, and measurement of time dependence of the LIF intensities to extract kinetic information.

3.1 FLOW SYSTEM

A schematic diagram of flow system is illustrated in Fig. 3.1. A reaction cell made of Pyrex was evacuated with a rotary pump (ULVAC D-950) and total pressure was monitored with a capacitance manometer (Baratron 122A, 10 Torr full scale). A trap cooled by liquid N_2 was set between the cell and the pump to avoid contamination of reaction cell with the oil from the pump. Partial pressure of sample gases and buffer gases were controlled with flow controllers: flow controllers (Koflok model 2204) and mass flow sensor (Koflok model 3810) were used for buffer gases (He or N_2) and other samples were controlled with mass flow controllers (STEC SEC-400 mark3 and Tylan FC-260KZ, 10 - 30 CCM full scale).

The partial pressure of the samples were estimated using the following expression:

$$P_{sample} = \frac{f_{sample}}{f_{total}} \times P_{total}\,, \qquad (1)$$

where the pressure of a species i is expressed P_i and flow rate is f_i in unit of $cm^3\ min^{-1}$. Total flow rate was obtained from the sum of the flow rates of all the gases. The flow rates of samples were obtained by the following equation:

$$f_i = a \cdot V_i + b, \quad (2)$$

where V_i is the voltage output from the flow controller of a species i and a and b are the constants which are given to each sample gas. The constants were determined by the following procedure:

1. A vessel whose volume was correctly obtained was filled with sample gas of interest. Its initial pressure is defined to be P_0.
2. The gas was evacuated at a constant output voltage from a controller. Total pressure (buffer gas) was kept the same as that in the actual experiment.
3. The pressure of the vessel (P_1) was recorded after an appropriate time (t). The actual flow rate (f) of sample gas was obtained by the following expression;

$$f = \frac{(P_0 - P_1)}{t}. \quad (3)$$

These procedure were done at other voltages, and then the constants were obtained from a plot of measured flow rate versus voltage. A typical example of the plot is shown in Fig. 3.2 and the constants for various sample gases obtained the present experiment are listed in table 1. The constants of buffer gases were determined by the same way of the sample gases at various experimental conditions (Table 2).

Another way for determination of the flow rates of samples was applied when the constants were not able to obtain experimentally. The flow rate was estimated by the equation of

$$f = \frac{V_i}{V_{full\ scale,i}} \times f_{full\ scale,i} \times C.F., \quad (4)$$

where i is the numerical name of the flow meter (or controller) and $C.F.$ is a conversion factor given by vendors.

The flowing system in the present experiment can be utilized for the study on reactions between radical and atom. Atoms are generated by microwave discharge and radicals are generated by pulse laser photolysis. In the present apparatus, the wall loss of atoms can be measured with a sliding injector and the concentration of atoms are determined by the improved titration. Details of the study on radical - atom reaction are described in chapter 4 (reaction between CF_2 + O).

3.2 LASERS AND DETECTION SYSTEM

Figure 3.3 shows a schematic diagram of the lasers and detection systems. Reactions were initiated by pulse laser photolysis of parent molecules and radical species in the system were probed by the laser-induced fluorescence (LIF) technique.

An excimer laser (Lambda Physik Lextra-50SL, 193 nm (ArF) or 248 nm (KrF)) was used for photolysis. The wavelength was decided to produce more radicals: absorption cross section of parent molecules and yield of the radicals. The fluence of the excimer laser beam was monitored with joule meters (Gentec ED-500, ED-100A, and built-in excimer laser). The beam of excimer laser was reflected with two 90° quartz prisms and directed in the reaction cell after trimmed with some apertures.

In order to detect radical species, a Nd^{3+}:YAG laser (Continuum YG-660-20) pumped dye laser (Lambda Physik LPD3001Y) was used to excite LIF. A frequency doubled beam was generated to detect CF_2 and OH. The Pellin-Broca prism was used to separate the frequency doubled beam from the fundamental beam from the dye laser. Output beam from the dye laser through the Pellin-Broca prism, was aligned with two aluminum-coated mirrors. The absolute fluence of the dye laser beam was measured with joule

meter (Gentec ED-100A), and was monitored with the photodiodes (Hamamatsu S-1722-02 and S-1336-5BQ) after reflected with quartz windows. The lasers were operated at 20 Hz repetition rate.

Two irises were set on both sides of reaction cell for trimming the laser beams and checking the light path. The reaction cell has quartz Brewster windows and two baffles were set to reduce scattered light and the fluorescence from the Pylex cell itself. All optical devices (prisms and windows) used in the present experiment were made of synthetic quartz to prevent uv light absorbing.

Fluorescence was collected with a lens and focused on the anode of the photomultipliers (Hamamatsu R928 and R374) through appropriate optical filters to reduce stray light. The filters were replaced with monochromator (JEOL, JSG-125S and Nikon, P-250) when dispersed LIF spectra were recorded. The signals from PMT's were amplified and averaged with gated integrators (Stanford Research SR-250). The signals from integrators were digitized with A/D converter (Stanford Research, SR-245) for processing with a computer and the data was stored on a disk.

3.3 MEASUREMENT WITH LASER-INDUCED FLUORESCENCE TECHNIQUE

Two types of measurement were performed in the present study; laser-induced fluorescence (LIF) excitation spectra and time dependence of LIF signals.

Radicals on a specific quantum state was identified by the excitation spectra recorded with an appropriate fixed delay time between pump and probe laser. The wavelength was scanned with a computer interface module (SR-245) and a control unit of dye laser.

Temporal profiles of LIF signals gave kinetic information on reactions and relaxation. The delay time between pump and probe laser was scanned with SR-245 and timing devices. In the present study, boxcar integrator (SR-250) and gated photon counter (Stanford Research, SR-400) were used as gate scanning devices.

Table 1. Calibrated constants for determination of flow rates of samples.

Sample[a]	a ($cm^3\ min^{-1}$/volts)[b]	b ($cm^3\ min^{-1}$)[b]	flow controller
NH_3	1.14	0.0424	Tylan 10 CCM
CH_4	3.28	0.151	Tylan 30 CCM
NO	1.4	0.0371	STEC 10 CCM

a. Flow rates of other sample gases (O_3, NO_2, CF_4, O_2, and CF_2Br_2) were determined with conversion factors given by vendors.

b. Flow rate of samples is expressed by

$$f_i = a \cdot V_i + b.$$

Table 2. Conversion factors of buffer gases at various experimental conditions.

Buffer gas	Total pressure /Torr	velocity / $m \cdot s^{-1}$	conversion factor
N_2	1	1	0.720
N_2	5	1	0.727
N_2	10	1	0.693
N_2	10	0.2	0.728
He	5	1	1.03
He	10	1	1.03

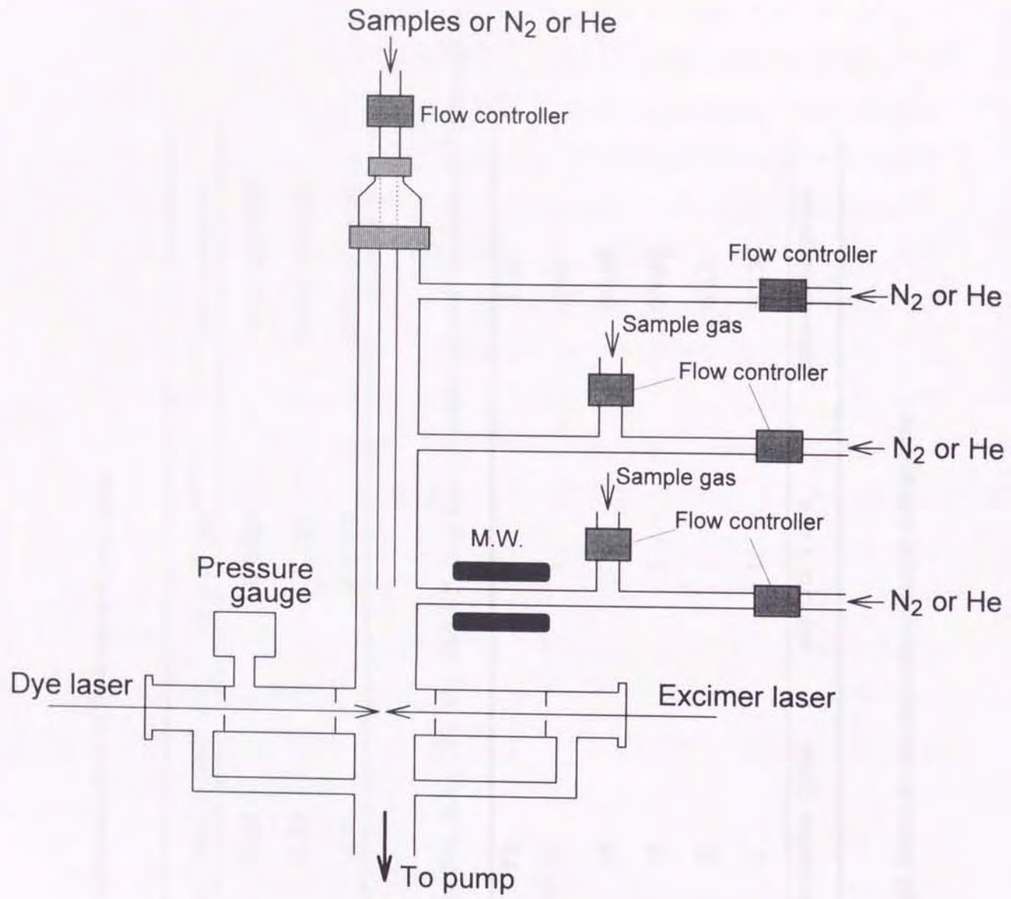

Fig. 3.1. A schematic diagram of the flow system. A buffer gas of N_2 or He can be selected. M.W. is a microwave cavity for generation of atoms. A sliding injector is used for the study of the radical - atom reaction.

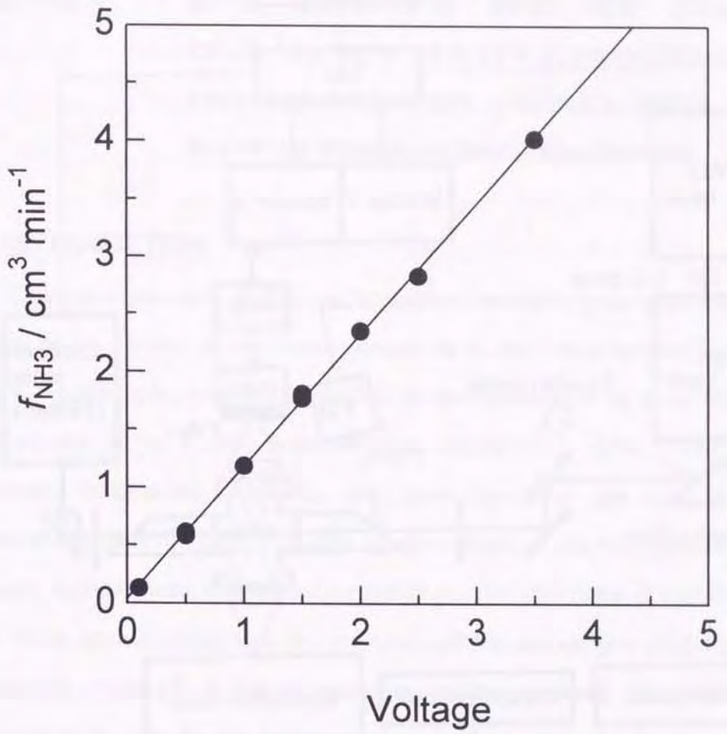

Fig. 3.2. Result of calibration of NH_3 flow rate. Dots denotes the values obtained by experiment, and solid line denotes a result of least squares fit for $y=ax+b$. A Slope of this plot is 1.14 $cm^3 \cdot min^{-1} \cdot volt^{-1}$ and intercept is 0.0424 $cm^3 \cdot min^{-1}$.

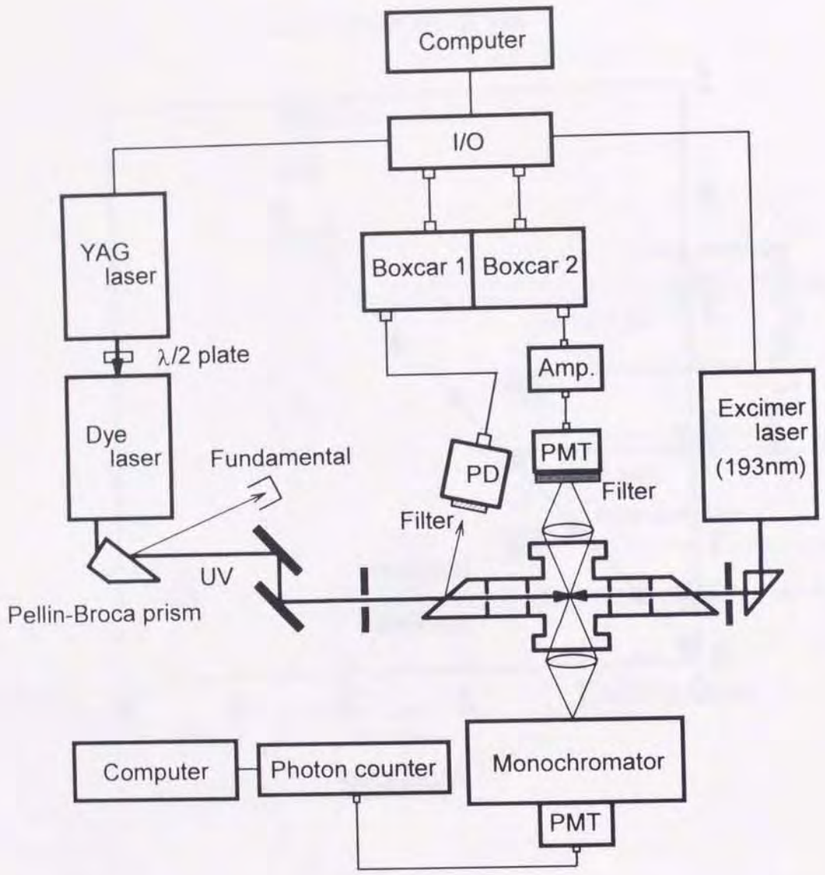

Fig. 3.3. A schematic diagram of the lasers and detection systems.

CHAPTER 4 RATE CONSTANTS FOR THE REACTIONS $CF_2(\tilde{X}\ ^1A_1, V_2=0$ AND 1) + O DETERMINED BY A PHOTODISSOCIATION COUPLED WIITH LASER-INDUCED FLUORESCENCE TECHNIQUE

4.1 INTRODUCTION

Chlorofluorocarbon (CFC) and bromofluorocarbon (halon) have been well known to be causes of the ozone depletion in the stratosphere.[1] Chlorine atoms, for example, emitted from CFC in the photolysis by solar flux in the stratosphere initiate the chain reaction called ClO_x cycle. The counter products, halocarbon radicals, are also produced in the photolysis. Trihalomethyls or dihalomethylenes are generated by the release of one or two halogen atom(s) from CFC's and/or halons. The reactions of trihalomethyls with such stable molecules in the atmosphere as oxygen (O_2) have been intensively studied.[2] A few propensities for the reactions have been found: trihalomethyls, CF_mX_n (X: halogen atom, m+n=3, m=0-3), simply recombine with oxygen, producing trihalomethyl peroxide ($CF_mX_nO_2$); the reaction rate constants are larger for the molecules containing more fluorine atoms. Dihalomethylenes, CF_mX_n (m+n=2, m=0-2), on the other hand, are non-reactive with stable molecules such as O_2, N_2, NO, and N_2O at around room temperature; thus, they appear to be *inert*. Only the upper limits of the rate constants for the reactions have been reported so far.[3-6]

Reactions of atomic species with dihalomethylene CF_mX_n, however, have recently been reported to be relatively fast and one of the reaction products is a halogen atom originating from the dihalomethylene.[7-9] The halogen atoms

emitted in the reaction could also be an initiator of the ClO_x (or BrO_x) cycle in the ozone depletion. Accordingly, precise measurements of the rate constants for the reactions of dihalomethylene with atomic species are now valuable to propose as an additional mechanism for the production of halogen atoms followed by the ozone depletion cycle.

The photolysis in the stratosphere is due to the solar flux in the so called "solar window" whose wavelength is over 185-220 nm between the Schumann-Runge bands (λ < 185 nm) of O_2 and Hartley bands (λ > 220 nm) of O_3.[10] Since the dissociation energies of C-Cl and C-Br bonds are small, large excess energy can be deposited into the molecules generated in the photolysis even with a release of two atoms, e.g., E_{excess} = 45 kJ mol^{-1} for the photolysis CF_2Cl_2(CFC-12) + hυ(200 nm) $\rightarrow$ CF_2 + 2Cl.

Vibrational relaxation rate is fast even in the stratosphere (< 50 Torr), whereas some unrelaxed molecules can directly proceed to reactions. The vibrational excitation possibly accelerates the reaction rates or opens new reaction paths to the products which cannot be produced in the reactions of vibration-less radicals. In the present work, a reaction CF_2 ($\tilde{X}^1A_1$) + $O(^3P)$ have been studied and determined the overall rate constants not only for the reaction $CF_2(v_1v_2v_3=000)$ + $O(^3P)$ but also for the vibrationally excited $CF_2(v_1v_2v_3=010)$ + $O(^3P)$ by uv pulsed laser photolysis and tunable pulsed laser probe technique coupled with a conventional discharge-flow method.

The CF_2 + O reaction has also attracted a great deal of attention in the field of dry etching of semiconductors with plasma processes. Addition of small amount of O_2 into CF_4 plasma effectively improves the etching rate of Si and SiO_2 substrates.[11-14] Two groups employed discharge-flow systems with

mass spectrometry in order to measure the overall rate constant for the reaction CF_2 + O and to identify the reaction products. Ryan and Plumb[7] reported the rate constant [$(1.8\pm0.4)\times10^{-11}$ cm^3 $molecule^{-1}$ s^{-1}] and concluded the path CF_2 + O $\rightarrow$ FCO + F was dominant over another channel CF_2 + O $\rightarrow$ CO + 2F(F_2). Tsai and McFadden[9] also determined the rate constant [$(2.0\pm0.4)\times10^{-11}$ cm^3 $molecule^{-1}$ s^{-1}] almost the same as that reported by Ryan and Plumb. Hancock *et al.*[8] employed the infrared laser multi-photon dissociation (IRMPD) to produce CF_2 radical from CF_2HCl and detected the CF_2 radical by LIF, and obtained a rate constant to be [$(1.75\pm0.35)\times10^{-11}$ cm^3 $molecule^{-1}$ s^{-1}]. All the groups reported almost the same rate constant for the reaction CF_2(v=0) + O. There, however, have been no reports on the reaction $CF_2(v_2=1)$ + O and the effect of vibrational excitation.

The reactions between atoms and/or radicals, in most cases, have been studied by the discharge-flow method. The technique has the advantages of producing high concentration of atoms or radicals and of measuring the absolute concentrations especially of atomic species, which is conventionally known as titration. A crucial disadvantage of the method is low time resolution; the onset (t=0) of the reaction is not defined precisely and the effect of the wall cannot be negligible; correction for the wall loss of active species like atoms and radicals is cumbersome. A pulsed method, on the other hand, by pulsed laser photolysis is a more reliable technique to measure the rate constants for the reactions between atoms or radicals and stable molecules. The technique enables high time resolution; however, it is not suitable for determination of absolute concentrations of atoms or radicals. In the present study, an apparatus that makes the best use of the advantages of

two methods have been constructed to determine the rate constants for the reactions between dihalomethylene and atoms. Parent molecules flowing with atoms are irradiated with a laser pulse and then the radical-atom reaction of interest proceeds in a cell. Concentration of the radical in question is probed in real time by the LIF technique at high sensitivity and with high time resolution.

4.2 EXPERIMENT

The uv photolysis at 193 nm (ArF laser) can effectively produce vibrationally excited CF_2 radicals and demonstrate the production of CF_2 from CFC's or halons in the stratosphere within the "solar window". Vibrational excitation of CF_2 initially prepared can be achieved by the uv laser photolysis but not by microwave discharge. The experimental set-up is schematically shown in Fig. 4.1(a) for the flow system and Fig. 4.1(b) for signal detection and acquisition. Oxygen atoms were produced by the microwave discharge (2.45GHz, 80W) in the mixture of O_2/He. The flow of oxygen atom was mixed with that of dibromodifluoromethane CF_2Br_2 and admitted into a reaction cell made of a Pyrex tube with quartz windows. Concentrations of each stable component of the reaction mixtures were determined from the mass flow rates measured with mass flow controllers (STEC SEC-400 mark3) and the total pressure was monitored with a capacitance manometer (Baratron 122A, 10 Torr full scale). The reaction of CF_2Br_2 with oxygen atom has been reported to be sufficiently slow;[9] there was no difference in the concentration of $O(^3P)$ with and without CF_2Br_2 in our titration.

The mixture of CF_2Br_2/O was then irradiated with a 193 nm ArF

excimer laser (Lambda Physik LEXtra 50, 20 Hz, 500 $\mu J\ cm^{-2}$ just before the cell) producing CF_2 radicals from the parent molecule CF_2Br_2. The onset of the reaction CF_2 + O was defined with the irradiation of the 193 nm laser. The CF_2 radical was probed with a Nd^{3+}:YAG laser (Continuum YG660-20, 40 mJ/pulse at 355nm) pumped frequency doubled (BBO) dye laser (Lambda Physik LPD-3001, Coumarin-522 dye, resolution 0.5 cm^{-1}). The output light from the dye laser went through a Pellin-Broca prism to separate the uv (≈262 nm) beam from the fundamental light and then counterpropagated with the ArF beam. A rectangular pulse of the sampling gate of a boxcar integrator (Stanford Research Systems SR250) was utilized for generating the delay of the dye beam from the excimer laser. The delay was fixed when the LIF excitation spectra were recorded and was continuously scanned when the temporal profiles of the LIF from CF_2 were observed.

Although Franck-Condon factors for the transitions from $v_2''=0$ is large for around[15] $v_2'=5$ or 6, emission from the upper levels appears too near the excitation wavelength to block the scattered laser light. The fluorescence via the transitions $\tilde{A}^1B_1 \leftarrow \tilde{X}^1A_1$ 020-000 (261.7 nm) and 030-010 (262.9 nm) were excited because the emissions appear over a wide range of wavelengths (300-370 nm). The LIF from CF_2 was detected with a photomultiplier (Hamamatsu R374) with a uv filter (TOSHIBA UV-D35 and UV-29). The signal from R374 was fed into a homemade boxcar and averaged over 10 laser shots and the data was stored in a computer. The reflection of the dye beam on the incident Brewster window was monitored with a photodiode (Hamamatsu S1722-02). The signal was also averaged with another homemade boxcar integrator and used to normalize the LIF signal to obtain

good S/N ratio. Fluence of the ArF laser fluctuated very little because the laser was operated in a constant power mode.

Absolute concentration of the oxygen atoms was determined by an improved conventional titration. Chemiluminescence in a slow reaction O + NO → NO_2^* (400-800 nm) following a fast reaction O + NO_2 → NO + O_2 was dispersed with a monochromator (JEOL JSG-125S, f=125 cm) at 505 nm and detected with a photomultiplier (Hamamatsu R928). Pulse signals were processed with a photon counter (Brookdeal 5C1 and 5C14). Since NO_2 is an effective adsorbent on the metal surface (stainless steel) inside the flow controller, it was very difficult to measure the absolute flow rates of the NO_2. Accordingly, an end point where the chemiluminescence is extinguished (added [NO_2] is equal to the initial [O]) was not found precisely. Since *relative* flow rates of NO_2 were controlled with the flow controller, a two-step titration was employed.[16] Details of two step titration will be descried in later section. The rate of wall loss of oxygen atom measured with the sliding injector was negligibly small.

CF_2Br_2 was obtained from Kanto Chemicals and had analyzed purities of >99.0 %. High grade NO_2 and NO in glass ampoules were supplied by Takachiho Cogyo with purities 99.5 % and 99.9 %. He (>99.9999%) and O_2 (99.9995%) were used and supplied by Nihon Sanso. All the sample gases were used without further purification.

4.3 RESULTS AND DISCUSSION

4.3.1 A Photolysis Laser Power Dependence of the Yield of CF_2.

In general, lower pressure of the parent molecule is better for kinetic study of radicals because undesirable side reactions should be suppressed. The photolysis of CF_2Br_2 at 193 nm was applied to the present study for several reasons. First, a larger absorption cross section (σ) is better for the efficient excitation of molecules with low concentration. Absorption cross sections of CF_2Br_2 ($\sigma = 1.05\times10^{-18}$ cm^2 and 7.3×10^{-19} cm^2 at 193 nm and 248 nm, respectively) are larger than those of CF_2Cl_2 ($\sigma = 3.76\times10^{-19}$ cm^2 at 193nm and negligibly small at 248 nm).[17] Second, a higher quantum yield for the radical of interest is preferable. There have, unfortunately, been no reports on the quantum yield for the production of CF_2 (ϕ_{CF_2}) in 193 nm photolysis. Talukdar *et al.*[18] measured the primary quantum yields for the formation of Br atoms (ϕ_{Br}) from CF_2Br_2. They reported $\phi_{Br} = (1.99 \pm 0.24)$ at 193 nm and $\phi_{Br} = (1.01 \pm 0.15)$ at 248 nm and suggested the quantum yields for dissociation were unity. Assuming that the production of Br_2 is a minor process, their results indicate that CF_2 is cleanly produced in the single photon process at 193 nm photolysis of CF_2Br_2. Another disadvantage of the photodissociation at 248 nm is that the CF_2 molecule produced in the primary photolysis promptly absorbs one more 248 nm photon via the $\tilde{A}^1B_1 \leftarrow \tilde{X}^1A_1$ 060-000 efficient resonant transition,[19,20] resulting in intense undesirable emission. Hence, the photolysis of CF_2Br_2 at 193 nm was employed as the best source of CF_2 in the present experiment.

Figure 4.2 shows the almost first-order dependence of the intensity of

the LIF [$CF_2(\tilde{A}^1B_1 \leftarrow \tilde{X}^1A_1)$] on the photolysis laser fluence. The fluorescence was excited at 261.7 nm (020-000 transition) with 25 μs delay from the photolysis. It, however, should be noted that the apparent first-order dependence is not necessarily evidence of a single photon process. Wampler *et al.*[21] also reported a linear dependence of the LIF intensity on the photolysis (193 nm) laser fluence. They concluded that all the absorption processes but one was saturated in a three-photon process. Their result cannot directly be compared with ours, because they input a much larger power (200 mJ cm^{-2}) than that in the present study (500 μJ cm^{-2}).

Linear dependence could be observed if one of the absorption processes is saturated in a multi-photon process, for example,

$$CF_2Br_2 + h\nu(193\ nm) \rightarrow CF_2Br^{\ddagger} + Br \quad (1)$$

$$CF_2Br^{\ddagger} + h\nu(193\ nm) \rightarrow CF_2 + Br. \quad (2)$$

The photolysis laser fluence in the present study was in the range of 150-700 μJ cm^{-2} , i.e., photon density $\Phi = 1.5\times10^{14}-6.8\times10^{14}$ photons cm^{-2}. Since the cross section for the absorption (1) is reported to be $\sigma = 1.05\times10^{-18}$ cm^2,[17] the first absorption is not saturated at all ($\sigma\Phi = 1.6\times10^{-4}-7.1\times10^{-4}$). The cross section for the second absorption (2), $\sigma = 6.2\times10^{-19}$ cm^2, [22] is smaller than that for the first absorption. Therefore, both processes (1) and (2) cannot be saturated under the present conditions. In conclusion, the CF_2 molecules are cleanly produced with a single-photon process in the present experiment, although it is difficult to distinguish simultaneous elimination from sequential decomposition of the two Br atoms in CF_2Br_2.

4.3.2 Vibrational Relaxation of $CF_2(\tilde{X}^1A_1, v_1v_2v_3 = 010)$.

Figure 4.3(a) shows an LIF excitation spectrum of $CF_2(\tilde{A}^1B_1 \leftarrow \tilde{X}^1A_1)$ recorded with 300 μs delay from the photolysis. Clear K-structure in the 020-000 band[15] is seen and a small peak assigned to the 030-010 hot band is also observed. Fine spiky peaks in the spectrum are not noise but reproducible rotational transitions in the vibronic transitions. The LIF excitation spectrum observed at a shorter (25 μs) delay is depicted in Fig. 4.3(b). The spectrum shows additional transitions due to hot vibronic bands; the 030-010 band appears larger than that observed with a longer delay. The spectra indicate that the nascent CF_2 molecules are vibrationally excited at least in the low-frequency bending (ν_2) mode.

The rate of vibrational relaxation was obviously dependent on the total pressure (He). The temporal profiles of the population on the $v_1v_2v_3$=010 vibrational level are shown in Fig. 4.4 observed at various total (He) pressures without changing the partial pressure of parent molecule CF_2Br_2. Higher pressures are more effective at vibrational relaxation as expected. Figure 4.5 is a relaxation curve of the temperature of the ν_2-vibrational mode evaluated from relative LIF intensities of 020-000 and 030-010 on the assumption that vibrational temperatures can be defined in the course of relaxation. Back-extrapolation gives about 1100 K as the nascent vibrational temperature. The ratio of the population of v_2=1 to that of v_2=0 is estimated to be 0.42:1.00. The rate constant for the vibrational relaxation by He was determined to be $(1.0\pm0.3)\times10^{-13}$ cm^3 $molecule^{-1}$ s^{-1} from the total pressure dependence of the decay rate of the LIF intensity (Fig. 4.4). To the best of our knowledge, the value obtained in the present experiment is the first one for the vibrational

relaxation rate of CF_2 in the electronic ground state.

Akins *et al.*[23] measured the rate constant for the vibrational relaxation of electronically excited $CF_2(\tilde{A}^1B_1, v_2'=1\text{-}6)$ in collisions with He, Ne, N_2, and SF_6. They reported that the efficiency of relaxation goes in the order of $Ne<N_2<He<SF_6$ and that the relaxation rates increased monotonically but faster than proportional to the vibrational quantum number v_2 irrespective of the collision partners. They speculated that the relaxation rate of the electronic ground state $CF_2(\tilde{X}^1A_1)$ was smaller by about a factor of 10 by the analogy with triatomic molecules such CO_2, N_2O, NCO, and O_3. The rate constant for the total deactivation rate of $CF_2(\tilde{A}^1B_1, v_2'= 1)$ by He, determined by Akins *et al.*, was 1×10^{-12} cm^3 $molecule^{-1}$ s^{-1}, which is, as they expected, a factor of 10 larger than that for the electronic ground state $CF_2(\tilde{X}^1A_1, v_2 = 1)$ determined by the present study.

4.3.3 Titration for determination of the concentration of atomic oxygen

A two steps titration[16] was employed to determine the concentration of oxygen atom. The first step is to add NO_2 to the O atom stream. The titration reactions with NO_2/O system are the following schemes:

$$O + NO_2 \rightarrow NO + O_2 \qquad k_1 : 10^{-11}\ cm^3\ molecule^{-1}\ s^{-1} \quad (3)$$

$$O + NO + M \rightarrow NO_2^* + M \qquad k_2 : 10^{-31}\ cm^6\ molecule^{-2}\ s^{-1} \quad (4)$$

$$NO_2^* \rightarrow NO_2 + h\nu\,(400 - 600\ nm) \qquad k_3 : 5\times10^3\ s^{-1} \quad (5)$$

Reaction (3) is 10^3-10^4 times faster than reaction (4) under the present experimental conditions (M=0.5 - 5 Torr). Accordingly, the concentration of NO in the system is equal to the initial concentration of NO_2 as long as the amount of added NO_2 is less than that of atomic oxygen: $[NO] = [NO_2]_0$. The

time dependence of $[NO_2^*]$ is given by the following expression:

$$\frac{d[NO_2^*]}{dt} = k_2[NO][O][M] - k_3[NO_2^*] \ . \qquad (6)$$

The NO_2^* produced in reaction (4) converts to NO_2 by reaction (5) which is 10^4-10^5 times faster than reaction (4) under the present experiment conditions. As a result, steady-state approximation can be applied to $[NO_2^*]$ ($d[NO_2^*]/dt = 0$). A steady-state concentration of NO_2^*, $[NO_2^*]_{ss}$, is expressed by the following equation.

$$[NO_2^*]_{ss} = k_2[NO][O][M] \ / \ k_3. \qquad (7)$$

On the other hand, the intensity of NO_2^* ($I_{NO_2^*}$) is given by

$$I_{NO_2^*} \propto k_3[NO_2^*]. \qquad (8)$$

After the $[NO_2^*]$ in (8) is substituted with $[NO_2^*]_{ss}$ given by eq. (7), the following expression is derived:

$$I_{NO_2^*} \propto k_2[NO][O][M]. \qquad (8)'$$

Because the [NO] can be replaced with $[NO_2]_0$ as described above, and because [O] is equal to $[O]_0$-$[NO_2]_0$, the following equations are obtained:

$$I_{NO_2^*} \propto k_2[NO_2]_0\{[O]_0 - [NO_2]_0\}[M]$$

$$= -k_2[M]\left\{[NO_2]_0 - \frac{1}{2}[O]_0\right\}^2 + \frac{1}{4}k_2[M][O]_0^2, \qquad (9)$$

where $[O]_0$ represents the initial concentration of atomic oxygen. The parabolic feature between $I_{NO_2^*}$ and $[NO_2]_0$ is clearly seen in Fig 4.6(a). Thus, the maximum emission intensity of NO_2^* is achieved when $[NO_2]_0 = (1/2)[O]_0$ as expected by eq. (9), and the maximum intensity is expressed by

$$I_{NO_2^*}^{max} \propto \frac{1}{4}k_2[M][O]_0^2. \qquad (10)$$

The intensity of emission from NO_2^*, $I_{NO_2^*}$, reached the maximum at 2.5 cm^3

min^{-1} of NO_2. It, however, was very difficult to measure the accurate flow rate of the NO_2 in the present experiment, because NO_2 adsorbs on the internal wall of the flow controllers and because complicated corrections for the $2NO_2 \Leftrightarrow (NO_2)_2$ equilibrium are needed to derive flow rate of NO_2. Accordingly, the following process using NO is adopted next.

After we recorded the maximum intensity of emission from NO_2^* in the first step, the flow of NO_2 was stopped, and then only NO was added into the O atom stream. Since the emission from NO_2^* in the 2nd step is due only to (4) and (5), $I_{NO_2^*}$ is proportional to [NO], $[O]_0$, and [M]: $I_{NO_2^*} \propto k_2[O]_0[NO][M]$. Reaction (4) is so slow that there is no actual change of the concentration of NO in the system ($[NO]=[NO]_0$ and thus $I_{NO_2^*} \propto = k_2[O]_0[NO]_0[M]$). Therefore, $I_{NO_2^*}$ increase in proportion to $[NO]_0$. Figure 4.6(b) demonstrates the expected relation between $I_{NO_2^*}$ and $[NO]_0$. The detection systems were the same in both steps, and the proportionally constants for emission of NO_2^* are same. Hence, the following equations are satisfied when the NO was added until the maximum intensity of NO_2^* in the first step was reproduced.

$$I^{max}_{NO_2^*} \propto \frac{1}{4} k_2[M][O]_0^2 = k_2[NO]_0[O]_0[M]. \quad (11)$$

Therefore, the relation between the initial concentration of O atom and added NO is obtained by

$$[NO]_0 = \frac{1}{4} [O]_0 . \quad (12)$$

The concentration of NO added in the second step equals a quarter of the initial O atom concentration.

4.3.4 Reaction Rate Constant for $CF_2(\tilde{X}^1A_1, v_2=0)$ + O.

Fast thermalization (vibrational relaxation) is preferable to study the reaction $CF_2(v_2=0)$ + O, because vibrational relaxation produces the $v_2=0$ level for the reaction. However, the apparent yield of the oxygen atoms in the microwave discharge reduced too low a value at 10 Torr to perform the experiments. We, thus, adopted 5 Torr of total pressure with linear velocity of 5 m s^{-1} as a compromise between fast vibrational relaxation and effective production of oxygen atoms to study the reaction $CF_2(v_2 = 0)$ + O. At 5 Torr total pressure, the vibrational temperature decreases to ambient temperature (294 K) about 150 μs after the photolysis (Fig. 4.5).

The LIF from CF_2 was easily detected with only 0.41 mTorr of CF_2Br_2. Fluence of the photolysis laser was 500 μJ cm^{-2}, i.e., 4.9×10^{14} photons cm^{-2} and the photoabsorption cross section of CF_2Br_2 is 1.05×10^{-18} cm^2.[17] The upper limit of the concentration of CF_2 is roughly estimated to be 6.7×10^9 molecule cm^{-3} on the assumption that the quantum yield of the production of CF_2 is unity. Since about 5 mTorr of oxygen atoms (1.6×10^{14} atoms cm^{-3}) can be produced with the microwave discharge in the present experiment, the pseudo-first-order conditions ($[CF_2] \ll [O]$) was readily achieved. The concentration of the oxygen atoms was determined by the two step titration using NO_2 and NO as stated in the experimental section.

Figure 4.7 shows typical semi-logarithmic plots of the temporal profiles of the LIF [$CF_2(\tilde{A}^1B_1$-$\tilde{X}^1A_1$, 020-000)] intensities at different concentrations of oxygen atoms. The rise in the first 70 μs reflects the vibrational relaxation by He. Hancock *et al.*[8] employed the IRMPD of CF_2HCl to generate CF_2. Stephenson and King[24] measured the vibrational distributions in CF_2 formed

by IRMPD from CF_2HCl/Ar mixture and reported that the nascent vibrational temperature of the ν_2-mode was 1160 K. Nevertheless, Hancock *et al.*[8] observed no pronounced rise in the profiles of $CF_2(v_2=0)$ and tentatively concluded that cascading of population did not occur in their system. There might be several reasons for the difference in the vibrational relaxation between their observation and the present study : (1) While Hancock *et al.* used Ar as a flowing buffer gas, Helium was used in the present study. According to the semiclassical estimate of V-T energy transfer,[25] the V-T probability decreases with an increase in the masses of colliding molecules at the same temperature; (2) Vibrational distributions of CF_2 generated by IRMPD and by uv photolysis could be different. The nascent temperature of the ν_2-vibrational mode are almost the same (≈1100 K) in both experiments. The population in the three vibrational states, however, might not necessarily be the same in the different methods of the photolysis.

The decay rates of $CF_2(v_2=0)$ increase with the concentration of oxygen atoms (Fig. 4.7). The linearity after t = 150 μs of the plots indicates that the pseudo-first-order conditions were satisfied. A plot of the first-order apparent decay rate versus the concentration of oxygen atoms is shown in Figure 4.8. It can easily be seen that the rate increases in proportion to the oxygen concentration. The linear regression gives the second-order rate constant for the reaction between $CF_2(v_2=0)$ and O: $k = [1.63\pm0.3(2\sigma)]\times10^{-11}$ cm^3 $molecule^{-1}$ s^{-1}. The error denoted is due mainly to the uncertainty of the concentration of oxygen atoms. The rate constant is in excellent agreement with those previously reported [$(1.4\text{-}2.4)\times10^{-11}$ cm^3 $molecule^{-1}$ s^{-1}][7-9] within the error limits. There is an insignificant difference between the

rate constants previously reported and that in the present experiment, although the latter seems slightly smaller than the former. It might be suggested that the small but perceived rise in the temporal profiles might lower the decay rate, giving a somewhat smaller rate constant. However, this is not the case. The analysis by non-linear double-exponential least-squares fit of temporal profiles was also performed in order to clearly separate the rates for the rise and the decay. The analysis did not give a different rate constant.

The intercept in Fig. 4.8 corresponds to the decay without oxygen atoms (natural decay) that is mainly due to diffusion loss of CF_2 radicals from the observation zone defined by the probe laser beam. Higher pressures suppress the diffusion effect; however, it is hard to keep the oxygen atoms at an appropriate concentration at higher total pressures.

4.3.5 Reaction Rate Constant for $CF_2(\tilde{X}^1A_1, v_2=1) + O$.

The goal of the present experiment is not only to measure the rate constant for the reaction $CF_2(v_2=0) + O$ but also to examine the effect of vibrational excitation on the reaction. In contrast to the case of vibration-less ($v_2=0$) state, $CF_2(v_2=1) + O$ must be studied under the conditions of slow vibrational relaxation. Cascading of population due to vibrational relaxation by He competes with reaction and then the net effect of reaction on the decay profiles are almost canceled. While low total pressures are preferred for slow vibrational relaxation, diffusion loss is too fast to observe the effect of reaction on the decay profiles. As a result, oxygen atoms at very high concentration must be prepared to observe a distinctive change in the decay profiles of the

LIF intensities. After much preliminary work, a total pressure of 0.5 Torr with linear flow velocity of 5 m s^{-1} was found that the best experimental condition to study the reaction $CF_2(v_2=1)$ + O.

Another essential finding was that the rate of natural decays, which was observed without oxygen atoms but with oxygen molecules, decreased with an increase in the partial pressures of oxygen molecules: 4700 s^{-1} with no O_2 to 3300 s^{-1} at 170 mTorr of O_2. This was not the case for the reaction $CF_2(v_2=0)$ + O studied at higher total pressures (5 Torr). The change in the rate of natural decays is tentatively ascribed to the vibrational relaxation induced by O_2. Higher or energetically close vibrational levels, not only of the v_2-bending mode but other vibrational modes, are relaxed to the v_2=1 level to some extent. Since the partial pressure of O_2 (0-166 mTorr) in the flowing gas was not negligibly small at total pressure of 0.5 Torr, the effect of relaxation by O_2 showed itself.

It should also be noted that the experiments for v_2=1 were performed at total pressure of 0.5 Torr which is different from that in the experiments for v_2=0. There is a possibility that vibrationally excited $O_2(X^3\Sigma_g^-)$ and/or $O_2(a^1\Delta_g)$ are produced in the microwave discharge. Transit time from the discharge to the reaction zone was 80 ms, thus most of the vibrationally excited species might be relaxed to the vibrational ground state. We cared about whether vibrationally excited $O_2(X^3\Sigma_g^-)$ or $O_2(a^1\Delta_g)$ affected the population of $CF_2(v_2=1)$ due to relaxation. Accurate measurement of relative population of $CF_2(v_2=1)$ is disturbed in two cases: (1) CF_2 relaxation by vibrationally excited O_2 is greater than by ground state O_2; (2) excitation of CF_2 to v_2=1 from v_2=0 in a V-V energy transfer is effective by vibrationally

excited O_2. There have unfortunately been no data on vibrationally energy transfer between CF_2 and O_2. Vibrational quantum energies of low vibrational levels of $O_2(X^3\Sigma_g^-)$ and $O_2(a^1\Delta_g)$ are around 1500 and 1400 cm^{-1} which exceed that of CF_2 in v_2-mode (667 cm^{-1}) by more than a factor of 2. V-V energy transfer might be inefficient because of large energy mismatch but slow T-V energy transfer is an only way to energy exchange between CF_2 and O_2. Concentration of vibrationally excited states of O_2 must be much lower than that of vibration-less O_2. Therefore, vibrational relaxation and/or excitation of CF_2 by vibrationally excited O_2 can be negligible in determination of the rate constant for $CF_2(v_2=1)$ + O.

Temporal profiles of LIF (030-010) intensities were recorded at each O_2 pressure with and without the microwave discharge, i.e., with and without oxygen atoms. The differences in the decay rates correspond to the net effect of the reaction with oxygen atom on the decay of $CF_2(v_2=1)$. The dissociation ratio of oxygen, which is defined by $[O]/[O_2]$, was at most 3.5 %: hence, the difference in the concentration of oxygen molecules with and without microwave discharge was neglected. The apparent first-order decay rates were obtained from semi-logarithmic plots of the decay profiles. Figure 4.9 shows the dependence of the net decay rates on the concentration of oxygen atoms. Its slope corresponds to the second-order rate constant for the reaction $CF_2(v_2=1)$ + O: $k = [1.44\pm0.3(2\sigma)]\times10^{-11}$ cm^3 $molecule^{-1}$ s^{-1}. The intercept with error is (-120 ± 164) s^{-1}; hence, the small negative intercept does not have a physical meaning. The value is nearly identical as that for the reaction $CF_2(v_2=0)$ + O within the error limit. In other words, the FCF bending motion is not effective in promoting the chemical reaction between

CF_2 and O.

The rate constant obtained here is, to be exact, total removal rate of $CF_2(v_2=1)$ by oxygen atoms. If the vibrational relaxation by atomic species is simply dependent on their masses,[25] the rate constant of relaxation by oxygen atoms does not exceed that for He: $[1.0\pm0.3(2\sigma)]\times10^{-13}$ cm^3 $molecule^{-1}$ s^{-1}. The total removal rate constant obtained is larger than the vibrational relaxation rate constant by He by more than two orders of magnitude. This fact suggests that the reactive process is predominant over relaxation.

4.3.6 Quantum Mechanical Calculation of the Reaction Path

There has been no report on the temperature dependence of the reaction rate constant or activation barrier along the reaction path. An *ab initio* calculation was performed to discuss the results on the rate constants and to make clear the correlation between reactants and products. Figure 4.10 shows the calculated enthalpy diagram of the system CF_2 + O. $CF_2(\tilde{X}^1A_1)$ + $O(^3P)$ correlates with the triplet intermediate $F_2CO(^3A''$ or $^3A')$ but not with stable singlet $F_2CO(\tilde{X}^1A_1)$. Both F_2CO of $^3A''$ and $^3A'$ proceed to the products $F(^2P)$ + $FCO(\tilde{X}^2A')$ via respective transition states. There is no barrier throughout the reaction path via the $^3A''$ intermediate; another intermediate $^3A'$, however, does not smoothly proceed to the products at 294 K because of high barrier on the reaction path.

These triplet intermediates belong to Cs point group; singlet $F_2CO(\tilde{X}^1A_1)$ belongs to C_{2v}. The structures of the $F_2CO(^3A''$ and $^3A')$ are depicted in Fig. 4.11. The oxygens are positioned on opposite sides of the F atoms and above the planes defined by FCF; the angles of elevation are 52.2° and 51.5° for $^3A''$

and $^3A'$, respectively. The result suggests that the approach of oxygen to CF_2 out-of-plane, not perpendicularly, but with about 50 degree is effective for the reaction. Accordingly, little effect of vibrational excitation on the reaction rate is observed, consistent with the structure of the intermediates. The antisymmetric stretching mode (v_3) of CF_2 might show some effect on the reaction, whereas neither uv absorption nor emission associated with the v_3-mode has been observed yet. The products $F + FCO(\tilde{X}^2A')$ are expected in the present calculation, which is consistent with the conclusion that FCO predominates as drawn by Ryan and Plum[7] and Tsai and McFadden.[9] Hancock and Heard[26,27] observed infrared chemiluminescence near 2000 cm^{-1} from the mixture of CF_2HCl/O irradiated with a CO_2 laser. They ascribed the chemiluminescence to the emission from vibrationally excited $CO_2^{\ddagger}$ produced in the reaction $FCO + O \rightarrow CO_2^{\ddagger} + F$, following $CF_2 + O \rightarrow FCO + F$.

4.4 CONCLUSION

The rate constants for the reactions between $CF_2(v_2=0$ and $v_2=1)$ and oxygen have been determined: $[1.63\pm0.3(2\sigma)]\times10^{-11}$ cm^3 $molecule^{-1}$ s^{-1} for $v_2=0$ and $[1.44\pm0.3(2\sigma)]\times10^{-11}$ cm^3 $molecule^{-1}$ s^{-1} for $v_2=1$, respectively. The value for $v_2=0$ is in excellent agreement with the those previously reported. The rate constant for $v_2=1$ in the present study is the first report to our knowledge. There is no distinctive effect of the excitation of FCF bending (v_2) vibration, consistent with the structures of the triplet intermediates F_2CO. Theoretical calculation predicts the oxygen atom in the intermediate is placed on opposite side of the F atoms and the axis through C and O atom is not in

the plane defined by FCF.

The rate constant for vibrational relaxation in collisions with He, CF_2 ($\tilde{X}^1A_1$, v_2=1) + He → CF_2($\tilde{X}^1A_1$, v_2=0) + He, has also been determined: $[1.0\pm0.3(2\sigma)]\times10^{-13}$ cm^3 $molecule^{-1}$ s^{-1}. The value is smaller than that for the electronically excited state CF_2($\tilde{A}^1B_1$, v_2=1 → v_2=0) by an order of magnitude.

REFERENCES

1. M. J. Molina and F. S. Rowland, *Nature*, **249**, 810 (1974)
2. R. Atkinson, D. L. Baulch, R. A. Cox, R. F. Hampson, Jr., J. A. Kerr, and J. Troe, *J. Phys. Chem. Ref. Data*, **21**, 1125 (1992)
3. F. W. Dalby, *J. Chem. Phys.*, 41, 2297 (1964)
4. J. J. Tiee, F. B. Wampler, and W. W. Rice, Jr., *Chem. Phys. Lett.*, **73**, 519 (1980)
5. H. Meunier, J. R. Purdy, and B. A. Thrush, *J. Chem. Soc. Faraday Trans. 2*, **76**, 1304 (1980)
6. S. E. Biaklowski and W. A. Guillory, *J. Phys. Chem.*, **86**, 2007 (1982)
7. K. R. Ryan and I. C. Plumb, *Plasma Chem. Plasma Proc.*, **4**, 271 (1984)
8. G. Hancock, P. D. Harrison, and A. J. MacRobert, *J. Chem. Soc. Faraday Trans. 2*, **82**, 647 (1986)
9. C.-P. Tsai and D. L. McFadden, *Chem. Phys. Lett.*, **173**, 241 (1990)
10. P. Warneck, "*Chemistry of the Natural Atomosphere*," Academic Press, 1987.
11. C. J. Mogab, A. C. Adams, and D. L. Flamm, *J. Appl. Phys.*, **49**, 3769 (1978)
12. D. L. Flamm, V. M. Donnelly, and D. E. Ibbotson, *J. Vac. Sci. Thchnol.*, **B1**, 23 (1983)
13. H. Kawata, T. Shibano, K. Murata, and K. Nagami, *J. Appl. Phys.*, **54**, 2720 (1983)
14. Y. Horiike and M. Shibagaki, Suppl. to Jpn. *J. Appl. Phys.*, **15**, 13 (1976)

15. D. S. King, P. K. Schenck, and J. C. Stephenson. *J. Mol. Spectrosc.*, **78**, 1 (1979)

16. R. R. Reeves, G. Mannella, and P. Harteck, *J. Chem. Phys.*, **32**, 632 (1960)

17. W. B. DeMore, S. P. Sander, D. M. Golden, R. F. Hampson, M. J. Kurylo, C. J. Howard, A. R. Ravishankara, C. E. Kolb, and M. J. Molina, "*Chemical Kinetics and Photochemical Data Use in Stratospheric Modeling*," No. 10; JPL (NASA), 1992.

18. R. K. Talukdar, G. L. Vaghjiani, and A. R. Ravishankara, *J. Chem. Phys.*, **96**, 8194 (1992)

19. G. Dornhöfer, W. Hack, and W. Langel, *J. Phys. Chem.*, **87**, 3456 (1983)

20. W. Hack and W. Langel, *J. Phys. Chem.*, **87**, 3462 (1983)

21. F. B. Wampler, J. J. Tiee, W. W. Rice, and R. C. Oldenborg, *J. Chem. Phys.*, **71**, 3926 (1979)

22. T. R. Gosnell, A. J. Taylor, and J. L. Lyman, *J. Chem. Phys.*, **94**, 5949 (1991)

23. D. L. Akins, D. S. King, and J. C. Stephenson, *Chem. Phys. Lett.*, **65**, 257 (1979)

24. J. C. Stephenson and D. S. King, *J. Chem. Phys.*, **69**, 1485 (1978)

25. J. T. Yardley, "*Introduction to Molecular Energy Transfer*," Academic Press: New York, 1980; Chapter 4.

26. G. Hancock and D. E. Heard, *J. Chem. Soc. Faraday Trans.*, **87**, 1039 (1991)

27. G. Hancock and D. E. Heard, *J. Chem. Soc. Faraday Trans.*, **87**, 1045 (1991)

28. Gaussian 92, Revision C, C. M. Frisch, G. W. Trucks, M. Head-Gordon, P. M. W. Gill, M. W. Wong, J. B. Foresman, B. G. Johnson, H. B. Schlegel, M. A. Robb, E. S. Replogle, R. Gomperts, J. L. Andres, K. Raghavachari, J. S. Binkley, C. Gonzalez, R. L. Martin, D. J. Fox, D. J. Defrees, J. Baker, J. J. P. Stewart, and J. A. Pople, Gaussian, Inc., Pittsburgh, 1992.

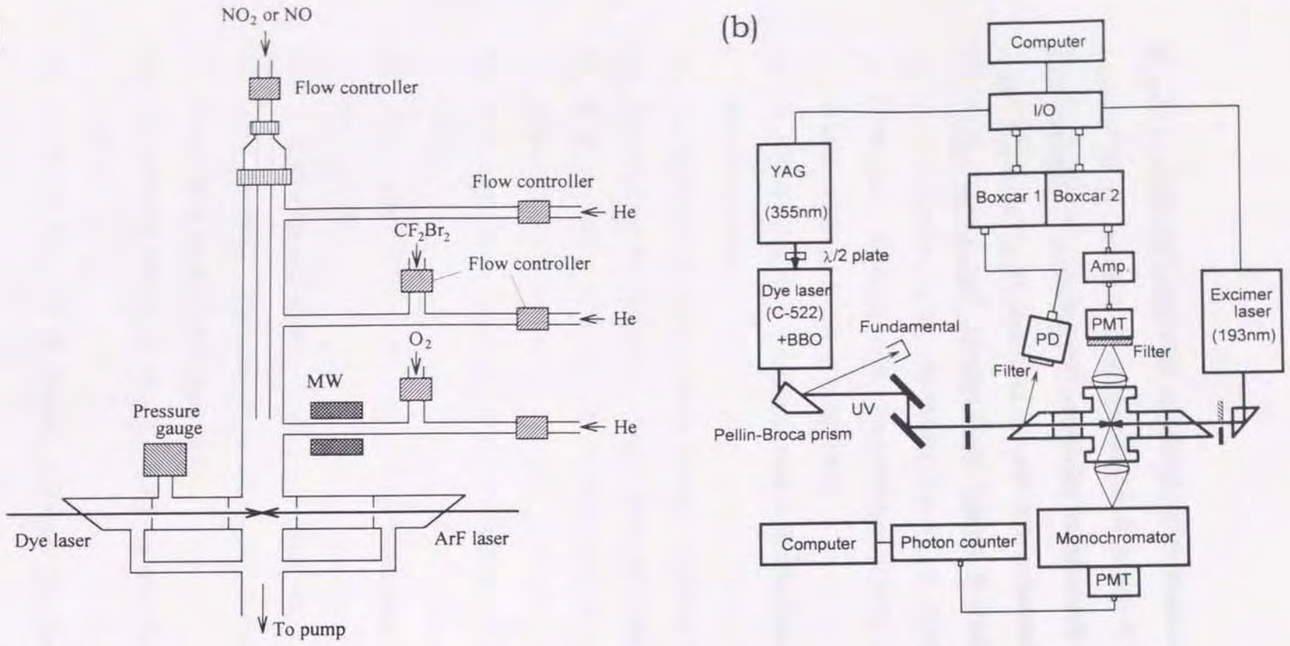

Fig. 4.1. Schematic diagram of the experimental apparatus: flow system; (a) detection and acquisition of the signals; (b). All the gases are controlled with the mass flow controller or the mass flow sensor with fine-metering valves. NO_2 and NO are admitted in the cell through the sliding injector. Mixture of oxygen and CF_2Br_2 is irradiated with 193 nm beam from the ArF laser. The photomultiplier (PMT) detects the LIF from $CF_2(\tilde{A}^1B_1–\tilde{X}^1A_1)$ excited with the frequency-doubled dye laser.

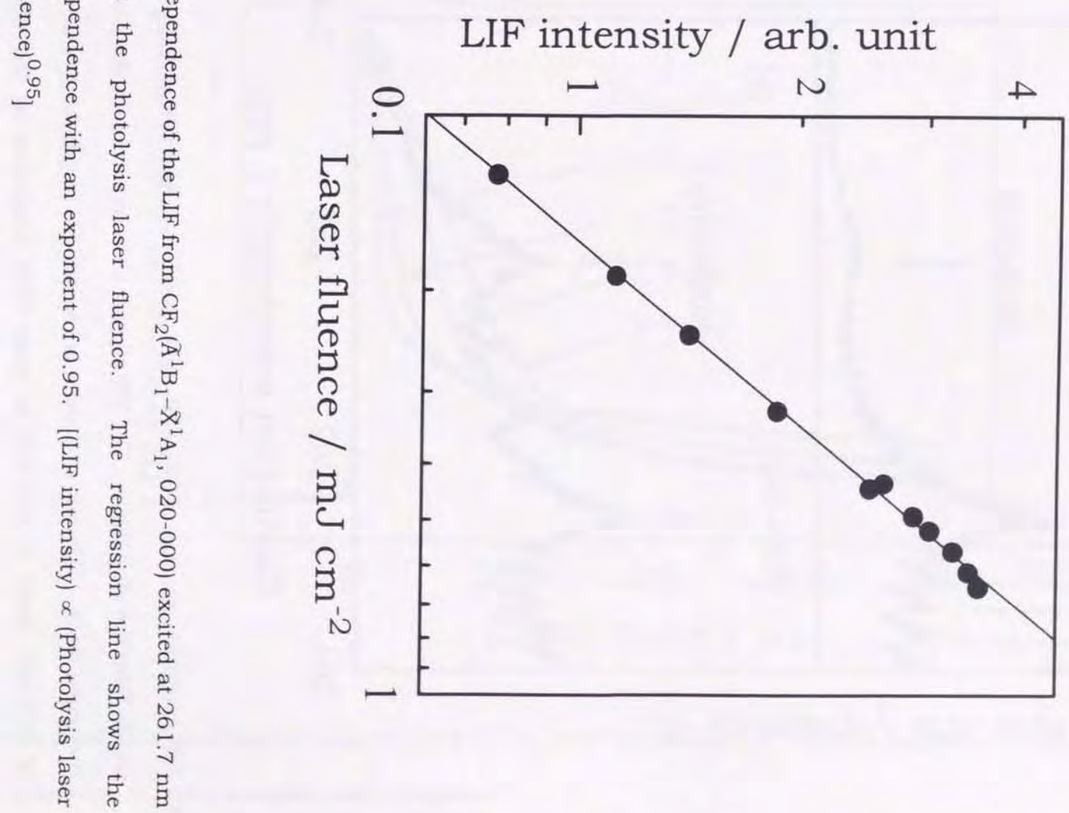

Fig. 4.2. Dependence of the LIF from $CF_2(\tilde{A}^1B_1–\tilde{X}^1A_1$, 020-000) excited at 261.7 nm on the photolysis laser fluence. The regression line shows the dependence with an exponent of 0.95. [(LIF intensity) ∝ (Photolysis laser fluence)$^{0.95}$]

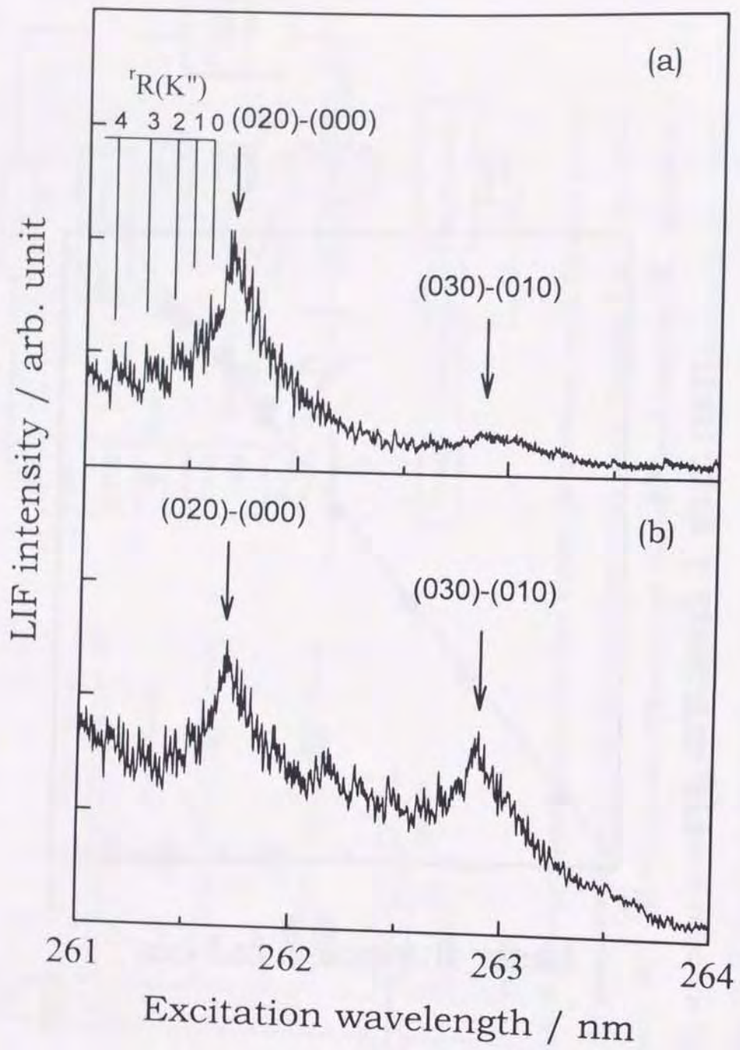

Fig. 4.3. LIF excitation spectra of $CF_2(\tilde{A}^1B_1–\tilde{X}^1A_1)$ with delays of 300μs; (a) and 25 μs; (b) from the photolysis. The LIF signals were corrected for the power of the probe laser. Vibronic excitation is remarkable in (b); relative intensity of 020-000 band to 030-010 is large after relaxation to the ambient temperature (294 K) (a).

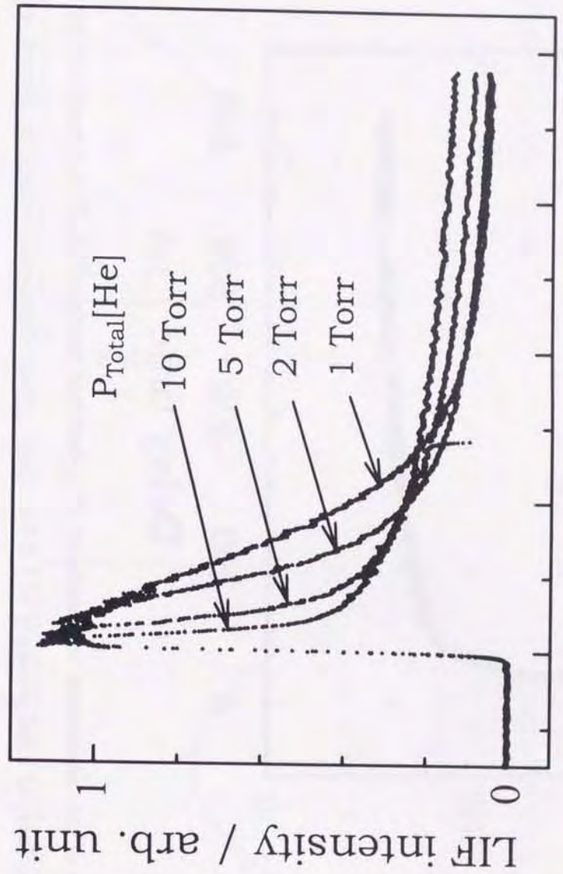

Fig. 4.4. Temporal profiles of the LIF from $CF_2(\tilde{A}^1B_1–\tilde{X}^1A_1$, 030-010) at various total (He) pressures. Vibrational relaxation is faster at higher total pressures.

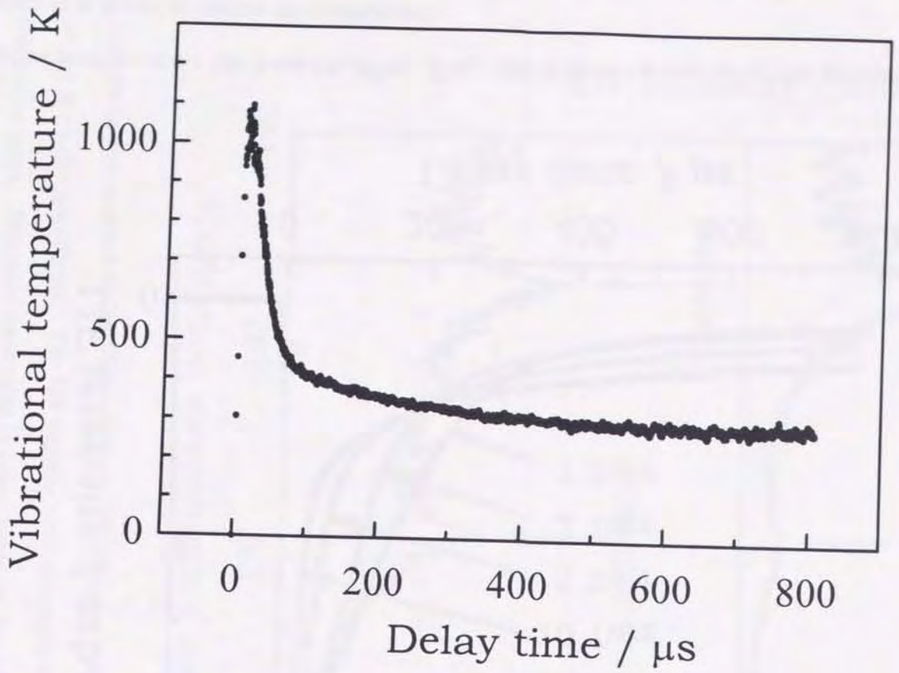

Fig. 4.5. Temporal profile of the vibrational temperature of ν_2-bending mode of $CF_2(\tilde{X}^1A_1)$ produced by 193 nm photolysis of CF_2Br_2 (0.41 mTorr) at total pressure of 5.0 Torr (He). Fast vibrational relaxation almost terminates at ca. 150 μs after the photolysis.

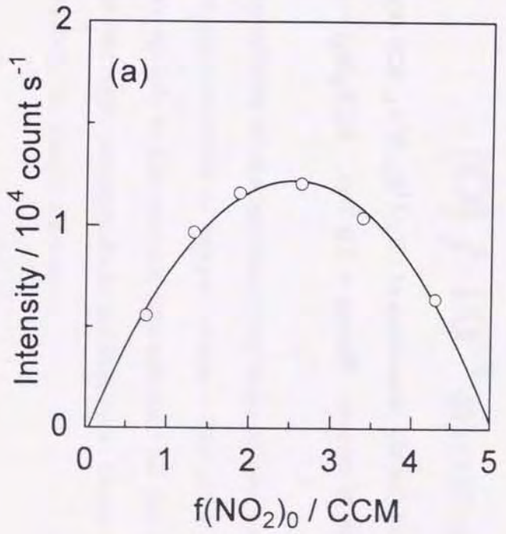

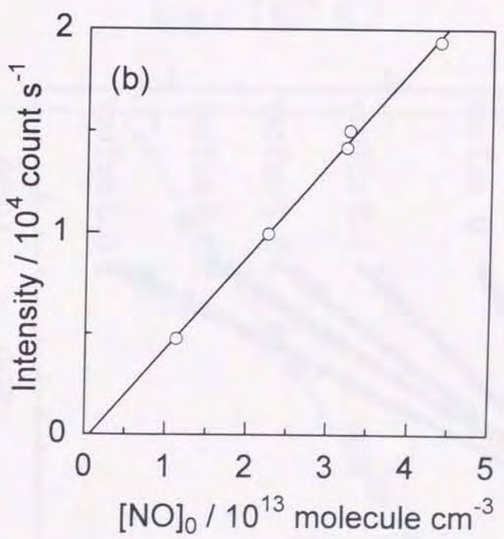

Fig. 4.6. Dependence of the emission intensity of NO_2^* on the flow rate of NO_2;(a) and concentration of NO;(b).

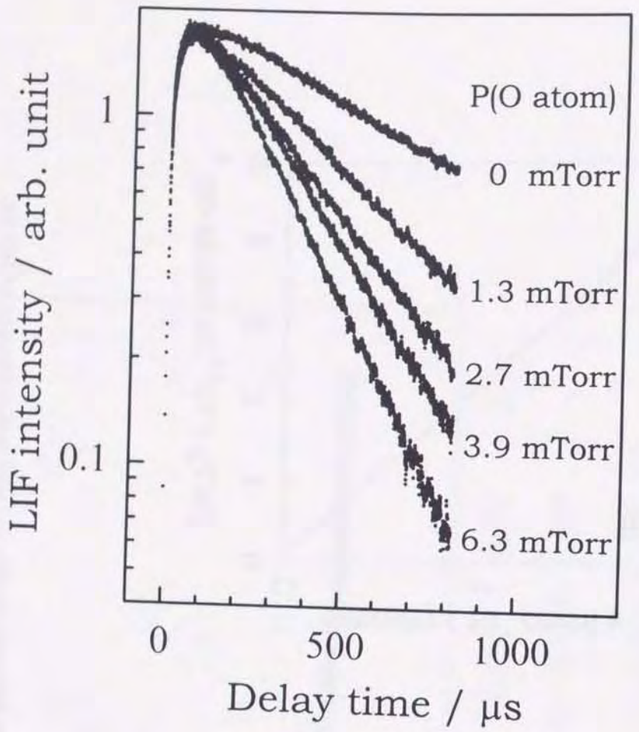

Fig. 4.7. Semilogarithmic plot of the LIF intensities of $CF_2(\tilde{A}^1B_1-\tilde{X}^1A_1, 020\text{-}000)$ at various concentrations of oxygen. P(total) = 5.0 Torr. $P(CF_2Br_2)$ = 0.41 mTorr.

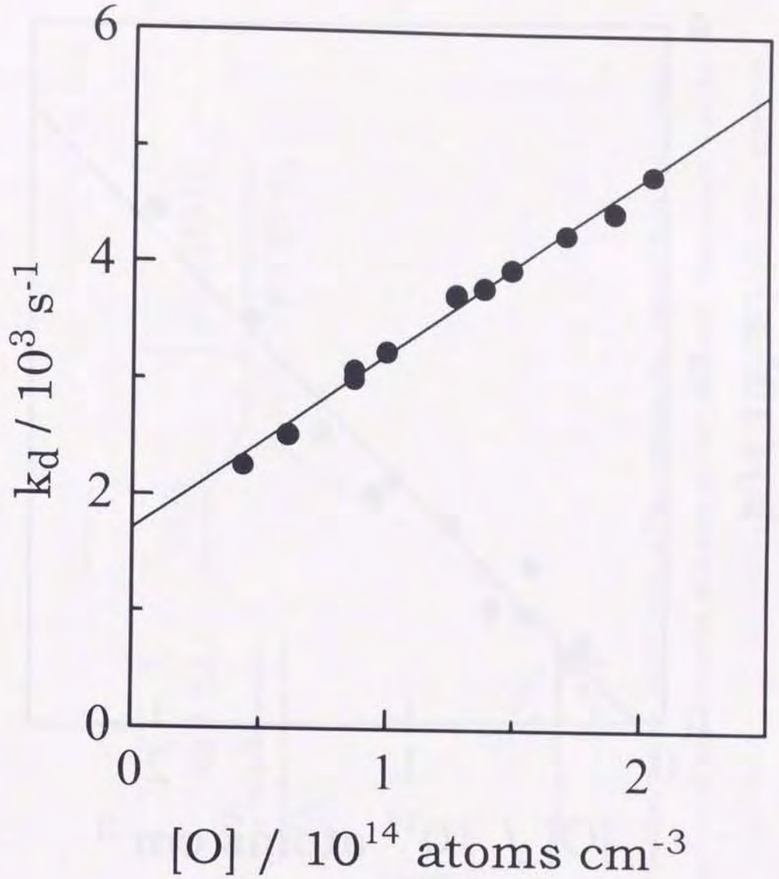

Fig. 4.8. Dependence of the apparent first-order decay rates k_d for $CF_2(v_2=0)$ on the concentration of oxygen atoms. The slope of the regression line corresponds to the reaction rate constant for the reaction $CF_2(v_2=0)$ + O. The intercept corresponds to the first-order decay due mainly to diffusion loss from the observation zone.

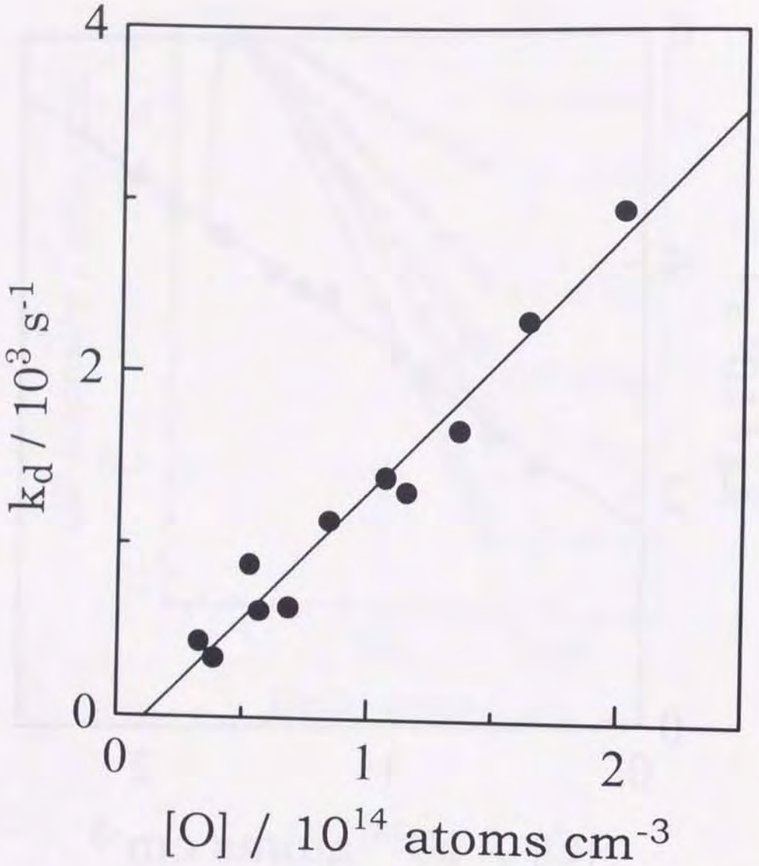

Fig. 4.9. Dependence of the first-order decay rates k_d for $CF_2(v_2=1)$ on the concentration of oxygen atoms. The k_d is defined with the difference of the first-order apparent decay rates with and without oxygen atoms at the same partial pressure of O_2.

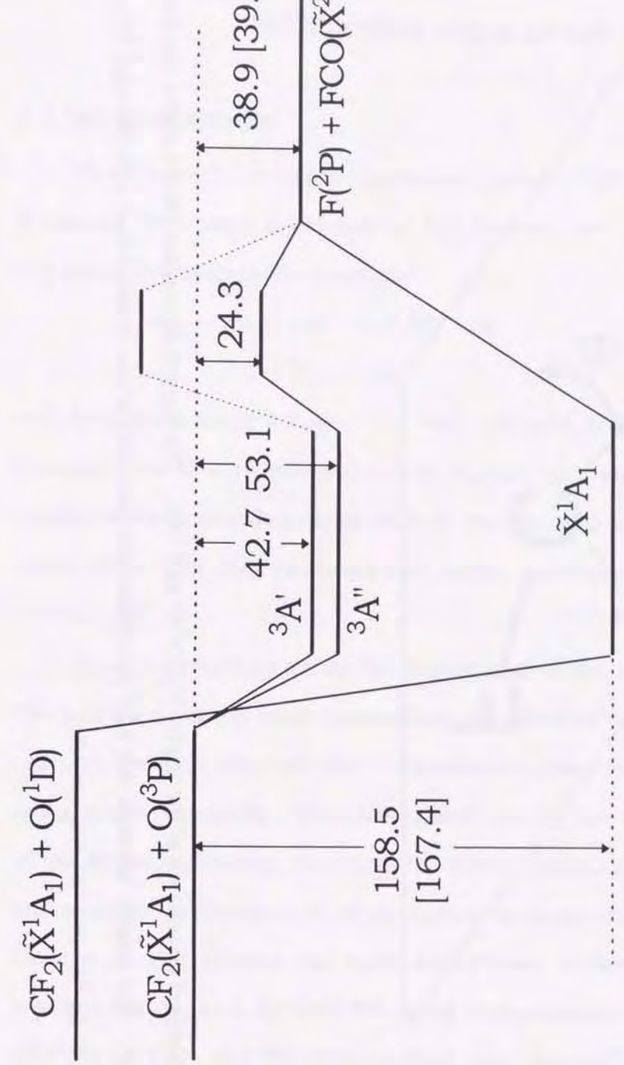

Fig. 4.10. Calculated enthalpy diagram of the reaction system of CF_2 + O. The energies (in units of kcal mol^{-1}) were obtained by Gaussian 92 (ref. 28) at the level of spin projected MP2 with 6-31G* basis set. The numbers in the parentheses are experimental values. $CF_2(\tilde{X}^1A_1) + O(^3P)$ proceeds to the triplet $F_2CO(^3A'')$ and to the products $F(^2P) + FCO(\tilde{X}^2A')$ on the surfaces with triplet electronic spin (S=1).

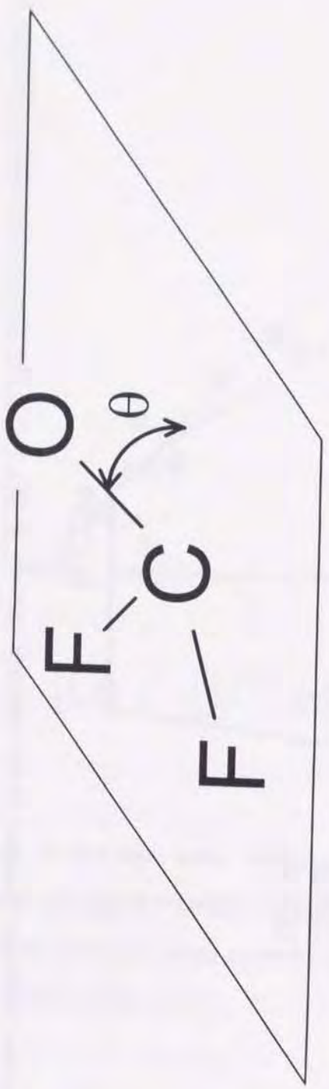

Fig. 4.11. Optimized structures of the triplet $F_2CO(^3A''$ and $^3A')$. The oxygen atoms are placed above the plane defined by FCF. The angles between the FCF plane and the direction of the internuclear axis through CO are 52.2° and 51.5° for $^3A''$ and $^3A'$, respectively.

CHAPTER 5 STUDY ON THE REACTION OF $NH_2(v)$ + NO: RATE CONSTANT OF THE REACTION AND VIBRATIONAL RELAXATION OF $NH_2(v)$ AND PRODUCTION YIELD OF OH.

5.1 INTRODUCTION

The reaction between amidogen radical, $NH_2(\tilde{X}^2A)$, and nitrogen monoxide (NO) plays a key role in the thermal $DeNO_x$ process.[1] There are two major channels in the reaction:

$$NH_2 + NO \rightarrow OH + N_2H\ (H_2 + N) \quad (1a)$$

$$\rightarrow N_2 + H_2O, \quad (1b)$$

and branching ratio between the two channels has been widely studied. Reaction (1a) is a radical-generation channel that contributes to the chain reactions via production of the radical species, and reaction (1b) is a chain-termination step that produces two stable molecules with exothermicity of 517 kJ mol^{-1}.

It is of interest to study the dependence of the removal rate of NH_2 on the various quantum state, particularly the effect of vibrational energy on the reaction between NH_2 and NO. Vibrational motion may accelerate reactions or open new channels. Translation and rotation are thermalized at the rate of gas kinetic collisions; vibrationally excited states, on the other hand, have longer lifetimes because of larger energy spacing between quantized levels. Gericke *et. al.*[2] studied the state dependence of the removal rate of state selected $NH_2(0_0$ and $2_1)$ with NO using infrared multiple photon dissociation (IRMPD) of N_2H_4 and CH_3NH_2 coupled with laser-induced fluorescence (LIF)

technique for detecting $NH_2(2_v)$. They, however, did not refer to the branching between reaction (1a) and (1b). Here, the labels X_n^m indicate transitions between the vibrational mode (X) with m quanta in the excited state and n quanta in the ground state.

In the present study, NH_3/193nm photolysis was applied to generate the vibrationally excited NH_2. The NH_3/193nm photolysis is easy to produce higher vibrational excited NH_2 because of its large available energy (170 kJ mol^{-1}). The reaction mechanism of NH_2 + NO was discussed on the basis of the experimental results: (1) Detection of highly excited NH_2 ($2_{v>1}$) by LIF technique; (2) The rate constant for vibrational relaxation of $NH_2(2_v)$ by collision partners (CF_4 and N_2) and for the reaction between $NH_2(2_v)$ and NO; and (3) Production yield of OH in the reaction of NH_2+NO using original technique for calibration of LIF intensities.

5.2 EXPERIMENT

Since details of the experiment apparatus were described in the previous chapter (Chapter 3), a special feature was written in the present here. A schematic diagram of the apparatus is shown in Fig.5.1.

Photolysis of NH_3 at 193 nm ($NH_3 + h\nu$ (193 nm) $\rightarrow NH_2(\tilde{X}^2A_1,2_v) + H$) was applied to generate NH_2 in the observation of LIF excitation spectra of NH_2. A fast reaction $O(^1D) + NH_3 \rightarrow OH + NH_2$ initiated by O_3/NH_3/248 nm photolysis was used to calibrate the LIF intensities of $NH_2(\tilde{A}^2A_1 - \tilde{X}^2B_1)$ and $OH(A^2\Sigma - X^2\Pi_i)$. Because the reaction between $O(^1D)$ and NH_3 generates the same amount of OH and NH_2 as products:

$$O(^1D) + NH_3 \rightarrow OH + NH_2, \qquad (2)$$

the ratio of LIF detectivities between NH_2 and OH was obtained. The production yield of OH in reaction (1) was obtained from this calibration.

Free radicals (NH_2 and OH) of interest were detected by LIF after an appropriate delay time from the photolysis. A solution of DCM dye (0.175 g/l) was used for detecting $NH_2(\tilde{X}^2B_1,0_0)$ and $OH(X^2\Pi_i,v=0)$. Typical dye laser fluence were 40 μJ for observing $NH_2(0_0)$ and 10 μJ for OH. Fortunately, the dye DCM covered the whole range of transitions of NH_2 ($\tilde{A}$-$\tilde{X}$, 2_0^8) and OH (A-X, 0-0 and 1-1) as shown in Fig. 5.2. Therefore, the wavelengths appropriate for the radicals (NH_2 or OH) were obtained easily by on or off the second harmonic generation of the dye laser. In order to detect vibrationally excited NH_2, Coumarin 522 dye (0.55 g/l) was used, and typical laser fluence was 20-30 μJ (A gain curve of Coumarin 522 is shown in Fig.5.3).

The LIF from NH_2 was detected with a photomultiplier (Hamamatsu R-928) through optical filters (HOYA R-62 and C-500S). Neutral density filters (Toshiba ND-50 and ND-10, transparency at 627.4 nm was 4.56%) were used in the experiment of NH_3/193 nm photolysis. Another photomultiplier (Hamamatsu, R374) with a uv filter (Toshiba UV-35) was set on opposite side of R928 for the detection of OH.

Ozone was synthesized by electric discharge of oxygen and residual oxygen was thoroughly degassed. Molecular oxygen of 7 Torr was the best for the electric discharge. If the pressure of oxygen molecule was higher than 7 Torr, the electric discharge could not occur. Since O_3 of at highest of 4.7 Torr was synthesized in a single run, replacement and discharge of O_2 were repeated twice or three times to generate about 10 Torr in a 3 litter glass bulb. Highly pure grade gases, NO (Takachiho Kagaku Cogyo, 99.9% and

Sumitomo-Seika, 99.9%), O_2 (Toyo-Sanso, 99.9995 %), N_2(Nihon-Sanso, 99.9999 %), and NH_3(Nihon-Sanso, 99.999 %) were used without further purification.

5.3 RESULT AND DISCUSSION

5.3.1 Spectroscopic study on the NH_2 produced in NH_3/193 nm photolysis.

Figures 5.4 and 5.5 show the LIF excitation spectra of $NH_2(v_2''=0)$[3-5] produced in the NH_3/193 nm photolysis. Since the excess energy in the NH_3 /193 nm photolysis system is large (ca. 170 kJ/mol), vibrationally or electronically excited NH_2 can be produced. Figure 5.6 shows a dispersed emission spectrum of the NH_3/193 nm system. Most of the peaks are assigned to the vibronic transitions of $NH_2(\tilde{A}\text{-}\tilde{X})$ system. The observed $NH_2(\tilde{A})$ might be produced in a single photon process (NH_3 + 193 nm → $NH_2(\tilde{A})$ + H), because no vibrational levels having more energy than excess energy of single-photon process was produced, and because the spectrum shown in Fig. 5.6 is almost identical with that recorded by Donnelly *et al.* who also concluded that the emission was due to a single photon process.[6] Furthermore, Donnelly *et al.* obtained branching fraction of NH_3/193 nm photolysis as follows:

$$NH_3 + h\nu\,(193\text{ nm}) \rightarrow NH_2(\tilde{X}) + H \qquad \Phi=0.965 \qquad (3a)$$

$$\rightarrow NH_2(\tilde{A}) + H \qquad \Phi=0.024 \qquad (3b)$$

$$\rightarrow NH(a^1\Delta) + H \qquad \Phi\leq 0.008. \qquad (3c)$$

Ground state of NH_2 is a dominant product and has a large internal energy.

Nadtochenko *et. al.*[7] observed that the 75±10 % of NH_2 radicals are formed in vibrationally excited states in the uv photolysis of NH_3. In order to

detect vibrationally excited $NH_2(\tilde{X})$, the LIF excitation spectra were recorded at various delay times between the photolysis and probe laser. Since the transition dipole moments of the 2_1^{13} and 2_2^{14} of NH_2 are larger than 2_1^9 and 2_2^{10},[8] the wavelength was scanned over the range of Coumarine-522 dye (Fig. 5.3). The LIF excitation spectra are shown in Fig. 5.7 at various delay times. The peaks observed at the longest delay (Fig. 5.7(d)) were assigned to the transitions $NH_2(\tilde{A}\text{-}\tilde{X}, 1_0^1 2_0^7)$, and those which had a maximum intensities at 80 μs (Fig. 5.7(c)) were assigned to $NH_2(\tilde{A}\text{-}\tilde{X}, 2_1^{13})$. Figure 5.8 shows a magnified spectrum of $NH_2(\tilde{X}, 2_1)$ in Fig. 5.7(c). The transition energies of $NH_2(\tilde{A}\text{-}\tilde{X}, 2_1^{13})$ observed was in excellent agreement with those calculated from the vibrational energy (E_{vib}=1490 cm^{-1}) of $NH_2(\tilde{X}, 2_1)$ and the transition energy of $NH_2(\tilde{A}\text{-}\tilde{X}, 2_0^{13})$.[3-5] The other peaks have a maximum at 50 and 20 μs were not assigned because no information of LIF excitation spectra of $NH_2(2_{v>1})$ had been reported in the range of the wavelengths shown in Fig. 5.7. The unassigned peaks are tentatively assigned to 2_2 and 2_3 as will be shown in the next section for convenience's sake.

5.3.2 Kinetic study on vibrationally excited $NH_2(2_v, v=0,1, \text{and } 2)$

A. Vibrational Relaxation of $NH_2(2_v)$

Time dependent profiles of populations on several vibrational levels were recorded as shown in Fig. 5.9. The abscissa corresponds to the delay time between the photolysis and probe lasers. The decay rate of the profiles in Fig.5.9(a) is faster than that of $NH_2(2_1)$ as seen in Fig 5.9(b). Since higher vibrational levels have shorter life times in generally, the peaks of Fig. 5.9(a) is

tentatively called as 2_2. The peaks whose decay rate is faster than that of 2_2, are also called as 2_3. The signals were not normalized by the laser fluence, because the LIF intensities of $NH_2(0_0)$ were saturated even with the fluence of about 40 μJ (Fig. 5.10). Since the relaxation rate of rotation is about 10^2 - 10^3 times faster than that of vibration,[9] the intensity of LIF due to a single rotational line is in proportional to the population on the vibrational level. The decay of the profiles shown in Figs. 5.9(a) and (b) represents the relaxation of vibrationally excited $NH_2(2_v$, v = 2 and 1).

First, consider the next relaxation scheme

$$A \xrightarrow{k_1} B \xrightarrow{k_2} C \qquad (4)$$

$$A,\ B,\ C \xrightarrow{k_d} \text{diffusion loss}, \qquad (5)$$

where A, B, and C are different vibrational levels: for example A denotes a vibrational level v=2, B is v=1, and C is v=0. Temporal profiles of the concentrations of B and C are given under the initial conditions:$[A]_{t=0}=[A]_0$, $[B]_{t=0}=[C]_{t=0}=0$, (Equations (4) and (5) were solved analytically as is done in textbooks.[10,11])

$$[B] = \frac{k_1[A]_0}{k_1 - k_2}\left\{\exp\left[-(k_2 + k_d)t\right] - \exp\left[-(k_1 + k_d)t\right]\right\} \qquad (6)$$

$$[C] = [A]_0\left\{\exp(-k_d t) - \frac{1}{k_1 - k_2}\left\{k_1 \exp\left[-(k_2 + k_d)t\right] - k_2 \exp\left[-(k_1 + k_d)t\right]\right\}\right\}, \qquad (7)$$

where k_d is the first-order rate constant for the diffusion loss. It can be assumed that the rate constant for the diffusion is the same for all the vibrational levels, because different vibrational levels have the same mass and

they must have almost identical diffusion rates.[12] Hence, the diffusion rate can be obtained from the semilogarithmic analysis of the profile of C (v=0). The equations multiplied by $\exp(+k_d t)$ are obtained from equations (6) and (7):

$$[B'] = [B]\exp(+k_d t) = \frac{k_1[A]_0}{k_1 - k_2}\left[\exp(-k_2 t) - \exp(-k_1 t)\right] \qquad (8)$$

$$[C'] = [C]\exp(+k_d t) = [A]_0\left\{1 - \frac{1}{k_1 - k_2}\left[k_1 \exp(-k_2 t) - k_2 \exp(-k_1 t)\right]\right\}, \qquad (9)$$

where [B′] and [C′] are corrected profiles. The corrected profiles of $NH_2(2_1$ and $0_0)$ are normalized by their maxima and shown in Fig. 5.11. The decay rates of B′ is correspond to the growing rate of C′, which indicates that the species C is actually produced from B. A mathematical formulation of the procedure will be shown in Appendix.

Figure 5.12 shows the corrected profiles of $NH_2(2_1)$ at various pressures of tetrafluoromethane (CF_4). The decay rates of 2_1 and growing rates of 0_0 increase with the pressures of CF_4(note the scales of abscissas). The fact indicates that vibrational relaxation $2_1 \rightarrow 0_0$ by CF_4 occurred. Production yield of NH_2 in the NH_3/193 nm photolysis was approximately 0.5% of NH_3 under the present experimental conditions: absorption cross section of NH_3 was 2.1×10^{-17} cm^2,[13] the density of ArF laser was 300 μJ cm^{-2} , the quantum yield of NH_2 was 0.965 (Eq. (3)), and the pressure of NH_3 was 13 mTorr. Hence, the pseudo-first-order condition ($[NH_2]$ << $[CF_4]$) was satisfied. The first-order decay rates were obtained by semilogarithmic analysis of the profiles of $NH_2(2_v)$ in the range where the plot was linear. The rate constants for the vibrational relaxation by CF_4 were obtained from a plot of the first-order decay rates versus pressures of CF_4 (Fig. 5.13): $(6.1\pm1.0) \times 10^{-11}$ and

$(2.7\pm0.5) \times 10^{-11}$ cm^3 $molecule^{-1}$ s^{-1} for $NH_2(2_2)$ and $NH_2(2_1)$, respectively.

The intercept in Fig. 5.13 represents the rate for the vibrational relaxation of $NH_2(2_v)$ by N_2 and NH_3. Although each rate constant for N_2 and NH_3 cannot be obtained, upper limit can be estimated on the assumption that collision partner was only N_2. Rate constant for the vibrational relaxation determined in the present study are listed in Table 1. Xiang *et al.*[14] determined the vibrational relaxation rate constant of $NH_2(2_1)$ by N_2 as $(4.3\pm0.3)\times10^{-13}$ cm^3 $molecule^{-1}$ s^{-1} by LIF/IRMPD (infrared multi-photon dissociation) technique. Their value is consistent with the upper limit obtained in the present study.

The frequency of NH_2 bending vibration is 1497 cm^{-1};[3] that of N_2 is 2359 cm^{-1}.[15] Since the difference of vibrational energy between NH_2 and N_2 is too large for efficient V-V vibrational energy transfer, the relaxation is mainly governed by slow V-T energy transfer. The fact that ratio of the rate constants for $NH_2(2_2)/NH_2(2_1)$ is close to 2 is consistent with Landau-Teller transition probability.

Since the vibrational relaxation by CF_4 is 100 times faster than that of N_2, the V-V energy transfer is a dominant process in the relaxation of $NH_2(2_v)$. In fact, the frequency of ν_3-mode of CF_4 is 1281 cm^{-1} and this value is relatively close to the frequency of ν_2-mode of NH_2. The fact that the ratio of rate constants for $NH_2(2_2)/NH_2(2_1)$ equals 2 is also consistent by V-V Landau-Teller probability of vibrational transition, because the low vibrational levels of NH_2 and CF_4 can be approximated to be harmonic oscillator.

B. Over All Rate Constant for Reaction of $NH_2(2_v)$ + NO

In measurement of the $NH_2(0_0)$ decay by NO, CF_4 of 250 mTorr was added to accelerate and terminate the vibrational relaxation from $NH_2(2_1)$ in early time. If the rate constants were measured without vibrational relaxant, the decay rate of $NH_2(0_0)$ was affected by growing rate which originated in vibrational relaxation of $NH_2(2_1)$ and may be underestimated as reported by Carrington.[16] Semilogarithmic plots of the profiles of $NH_2(0_0)$ are shown in Fig. 5.14, and the first order rate constants for the decay of $NH_2(0_0)$ were obtained from the slopes of the plots. The rate constants for the reaction of $NH_2(0_0)$ with NO are determined to be $(2.0\pm0.1) \times 10^{-11}$ cm^3 $molecule^{-1}$ s^{-1} from the dependence of first order rate constants on the pressures of NO.

The rate constant for $NH_2(0_0)$ is a little larger than a recommended value of NASA/JPL:[17] 1.7×10^{-11} cm^3 $molecule^{-1}$ s^{-1}. The recommended value was obtained from the average of the disconnected values from 8.3 to 27.0×10^{-12} cm^3 $molecule^{-1}$ s^{-1} determined by various experimental techniques. Furthermore, the values are classified into two groups: The averaged value of 1.9×10^{-11} cm^3 $molecule^{-1}$ s^{-1} from flash photolysis technique, while that of 0.9×10^{-11} cm^3 $molecule^{-1}$ s^{-1} obtained using the discharge flow technique. Although the reason for the discrepancy is not clear, the rate constant determined in the present experiment is in excellent agreement with the averaged value of the flash photolysis technique. In the present experiment, CF_4 was added to suppress the effect of the vibrational relaxation from 2_1 to 0_0. Therefore, the rate constant determined in the present experiment is more reliable than others.

The decay of $NH_2(2_v)$ were also accelerated with an increase in the

pressure of NO. Since the first-order rate constants for the rise and fall were almost the same, rate constant is not safely obtained by non-linear double-exponential analysis.[16] The overall rate constant for the reaction of $NH_2(2_v)$ + NO were determined from linear regression analysis shown in Fig. 5.15. The obtained rate constants are $(2.6\pm0.3) \times 10^{-11}$ for $NH_2(2_1)$, and $(2.4\pm0.3) \times 10^{-11}$ cm^3 $molecule^{-1}$ s^{-1} for $NH_2(2_2)$ and also listed in Table 2. Because too much acceleration of the decay of $NH_2(2_v)$ lowers the reliability of the results, no CF_4 was added in the experiments on vibrationally excited NH_2.

The rate constants for the vibrationally excited $NH_2(2_v)$ are little larger than that of $NH_2(0_0)$. The rate constants for $NH_2(2_{v>0})$ obtained in the present experiment are not the values for reactive process but those for total removal by NO. Whether or not the chemical processes of 2_2 and 2_1 are faster than that of 0_0 cannot be concluded. Gericke *et al.*[2] determined the rate constant for $NH_2(2_1)$ + NO as $(3.2\pm0.2) \times 10^{-11}$ cm^3 $molecule^{-1}$ s^{-1} with CH_3NH_2/IRMPD. The small difference of the rate constants is caused by the difficulties in determining the rate constant. Since the rate constants of $NH_2(2_v$, v=0,1, and 2) + NO reactions are almost the same, non-linear analysis is likely to fail to obtain the correct values and the semilogarithmic analysis is better to obtain more reliable constants.

5.3.3 Yield for the Production of OH in the Reaction of NH_2 + NO

The product $OH(X^2\Pi_i$, v=0) in the reaction (1) was detected by LIF: an example of excitation spectrum is shown in Fig. 5.16. Although OH(v=1) was also detected by LIF via $A^2\Sigma^+$-$X^2\Pi_i$, 1-1 transition, the population on v=1 was negligibly small (less than 3%).

The absolute yield of OH was determined on the basis of the calibration of the detectivities of LIF from NH_2 and OH. The calibration was performed using a reaction $O(^1D)$ + NH_3 → NH_2 + OH which was initiated by the irradiation of KrF (248 nm) laser to a mixture of O_3/NH_3. There are several advantages of the calibration: (1) Precise concentration of O_3 does not need to be measured, because equal quantities of NH_2 and OH are always formed; (2) There is little effect by side reactions. The reactions of NH_2 or OH with O_3 or NH_3 are much slower than the calibration reaction by more than three orders of magnitude; (3) Although vibrationally excited OH is produced in the calibration reaction, fast relaxation occurs by the NH_3 in the system, (4) Because the NH_2 and OH can be detected with a single laser dye (DCM, see Fig.5.2), artificial errors in changing the laser wavelengths are fairly small.

In order to calibrate for the LIF detectivities, measured temporal profiles were corrected by the first-order decay rate of diffusion loss [Fig. 5.17] as described in section 5.3.2.A. Since there is no process governing the decay of OH or NH_2 except physical diffusion, values of the plateaus correspond to the concentration of the radicals produced in the reaction $O(^1D)$ + NH_3. In the present experiment, LIF calibration were performed at two concentrations of O_3, and obtained the ratio was $I_{NH_2}/I_{OH}=0.95 \pm 0.10$.

The profiles of the OH produced in the reaction of NH_2 + NO are shown in Fig. 5.18 at various concentrations of NO. Since the LIF intensity of OH increases with increase of [NO], the reaction mechanism for production of OH can be thought as follows:

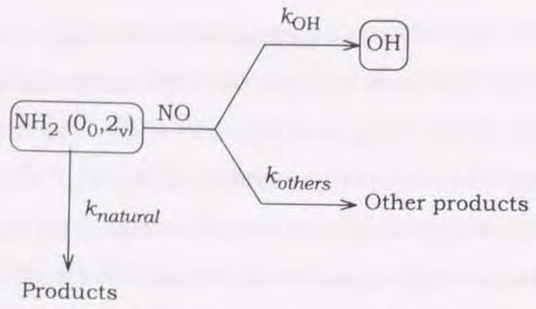

where k_{OH} is a rate constant for the production of OH, k_{others} is a constant for the path proceeding to other products in the reaction $NH_2(2_v)$ + NO, and $k_{natural}$ is a non-reactive removal rate of $NH_2(2_v)$ without NO. The production yield of OH is defined by the following equation:

$$\frac{[OH]}{[NH_2]_0} = \frac{k_{OH}[NO]}{(k_{OH} + k_{others})[NO] + k_{natural}} . \qquad (10)$$

The yield of OH in the reaction NH_2+NO, $\alpha = k_{OH}/(k_{OH}+k_{others})$, is given as $[NO] \rightarrow \infty$ in equation (10). Figure 5.19 shows a plot of $[OH]/[NH_2]_0$ versus concentrations of NO. The plot shows a fall-off feature, and an asymptotic value is determined to be 35.1 %.

Previously reported production yield of OH at various temperature was summarized by Park and Lin[18] (See Fig. 5.20). Although the yield of OH was measured at 297K, the value obtained by the present experiment (α=0.35) corresponds to that at 1000-1200K. The discrepancy is not surprising because NH_2 produced in the present NH_3/193nm photolysis is vibrationally excited. As seen in Fig. 5.9(c), the produced NH_2 are vibrationally excited because no vibration-less state of NH_2 is produced at t=0. The vibrational distribution of NH_2 might be thermalized to ambient temperature in the

experiments of other groups at room temperature. In the present experiment, however, vibrationally excited NH_2 react with NO before relaxation when the concentration of NO is large. Hence, the difference of α between the present experiment and other studies, both performed at room temperature, indicates that the production of OH is accelerated by vibrational excitation of NH_2.

5.3.4 A Mechanism for the Production of OH in NH_2 + NO

From a kinetic analysis described in section 5.3.1, the rate of the growth of the profile of OH is expected to coincide with that of decay of the reactant which produces the OH. As can be seen in Fig. 5.21., the decay rates of 0_0 and 2_1 of NH_2 are slower than those of the growth of the OH; however, the decay of 2_2 nicely fits to the growth of the OH. When CF_4 which is an effective relaxer of NH_2 was added to the system, the yield of OH decreased with an increase in the amount of CF_4 (Fig. 5.22.). The results also suggest that the OH is produced more effectively by higher vibrational levels of NH_2.

Walch[19] performed an *ab initio* calculation of the potential surface of the reaction between NH_2 and NO as depicted in Fig. 5.23. The dominant products in the reaction between NH_2 + NO is expected as H_2O and N_2 because the reaction path has no barrier, but a energy barrier of 2.9 kJ/mol is present on the channel producing OH. Since the vibrational energy of $NH_2(2_1)$ (=17.9 kJ/mol) is sufficiently larger than the energy barrier, the production yield of OH increases with vibrational energy of NH_2. If the first intermediate keeps a bending motion of NH_2, the migration of H atom (H_1) to O atom is accelerated. Hence, the vibrational excited NH_2 can effectively produce OH, and has a large rate constant.

APPENDIX

In this section, it is proved that the decay of B′ is identical with the growth of C′ in equations (8) and (9), by normalization with maxima of each profile.

$$[B'] = \frac{k_1[A]_0}{k_1 - k_2}\left[\exp(-k_2 t) - \exp(-k_1 t)\right] \tag{8}$$

$$[C'] = [A]_0\left\{1 - \frac{1}{k_1 - k_2}\left[k_1 \exp(-k_2 t) - k_2 \exp(-k_1 t)\right]\right\}. \tag{9}$$

First, the time when the profile of B reaches the maximum (t_{max}) is obtained by $d[B']/dt=0$:

$$t_{max} = \frac{1}{k_2 - k_1}\ln\left(\frac{k_2}{k_1}\right). \tag{A-1}$$

The value of profile B′ ($[B']_{max}$) at t_{max} is obtained to be

$$[B']_{max} = \left(\frac{k_2}{k_1}\right)^{\frac{-k_1}{k_2 - k_1}}\left(\frac{k_2 - k_1}{k_2}\right). \tag{A-2}$$

The normalized profile of B′ by $[B']_{max}$ is expressed by

$$[B']_{norm} = \frac{[B']}{[B']_{max}} = \left(\frac{k_1}{k_2}\right)^{\frac{k_1}{k_2 - k_1}}\left(\frac{k_1}{k_1 - k_2}\right)(\exp(-k_2 t) - \exp(-k_1 t)). \tag{A-3}$$

Because the profile of C′, on the other hand, reaches $[A]_0$ as $t\to\infty$, normalized [C′] is given by ($[C']_{norm}$) $[C']/[A]_0$. The maxima and minima of $[B']_{norm}$ and $[C']_{norm}$ are 1 and 0.

In order to check whether the growth of C′ is identical with the decay of B′ graphically, normalized profile of C′ is drawn upside down and expressed by the following equation:

$$1\text{-}[C']_{norm} = \exp(-k_2 t) + \frac{k_2}{k_1 - k_2}[\exp(-k_2 t) - \exp(-k_1 t)]. \tag{A-4}$$

And again, we obtain the corrected profile of C′ from substituting t for t-t_{max} and equation (A-1),

$$\begin{aligned}
1\text{-}[C']_{norm} &= \exp(-k_2(t - t_{max})) + \frac{k_2}{k_1 - k_2}\left\{\exp\left[-k_2(t - t_{max})\right] - \exp\left[-k_1(t - t_{max})\right]\right\} \\
&= \exp\left[\frac{k_2}{k_1 - k_2}\ln\left(\frac{k_1}{k_2}\right)\right]\exp(-k_2 t) \\
&\quad + \frac{k_2}{k_1 - k_2}\left\{\exp\left[\frac{k_2}{k_1 - k_2}\ln\left(\frac{k_1}{k_2}\right)\right]\exp(-k_2 t) - \exp\left[\frac{k_2}{k_1 - k_2}\ln\left(\frac{k_1}{k_2}\right)\right]\exp(-k_1 t)\right\} \\
&= \left(\frac{k_1}{k_2}\right)^{\frac{k_1}{k_2 - k_1}}\left(\frac{k_2}{k_1 - k_2}\right)\left[\exp(-k_2 t) - \exp(-k_1 t)\right].
\end{aligned} \tag{A-5}$$

The last expression is completely the same as (A-3).

REFERENCES

1. P. Glarborg, K. D.- Johansen, J. A. Miller, R. J. Kee, and M. E. Coltrin, Int. J. Chem. Kinet. **26**, 421 (1994)
2. K. -H. Gericke, L. M. Torres and W. A. Guillory, J. Chem. Phys., 80, 6134 (1984)
3. K. Dressler and D. A. Ramsay, Phil. Trans. Roy. Soc. Ser. A., **251**, 553 (1959)
4. J. W. C. Johns, D. A. Ramsay, and S. C. Ross, Can. J. Phys., **54**, 1804 (1976)
5. S. C. Ross, F. W. Birss, M. Vervloet, and D. A. Ramsay, J. Mol. Spectrosc., **129**, 436 (1988)
6. V. M. Donnelly, A. P. Baronavski, and J. R. McDonald, Chem. Phys., **43**, 271 (1979)
7. V. A. Nadtochenko, O. M. Sarkisov, M. P. Frolov, R. S. Tsanava, and S. G. Cheskis, Kinet. Catal. USSR **22**, 670 (1981)
8. C. Jungen, K. -E. J. Hallin, and A. J. Merer, Mol. Phys., **40**, 25 (1980)
9. R. D. Levine and R. B. Bernstein, "Molecular Reaction Dynamics and Chemical Reactivity," Oxford University Press (1987).
10. S. W. Benson, "The Foundations of Chemical Kinetics," Robert E. Kriger (1982)
11. K. J. Laidler, "Chemical Kinetics",3rd ed, Harper & Row (1987)
12. J. T. Yardley, "Introduction to Molecular Energy Transfer", Academic Press, New York (1980)
13. J. G. Calvert, and J. N. Pitts, Jr., "Photochemistry," John Wiley & Sons, Inc. , New York (****)

14. T. X. Xiang, K.-H. Gericke, L. M. Torres, and W. A. Guillory, Chem. Phys. Lett. **101**, 157 (1986)
15. K. P. Huber and G. Herzberg, "Molecular Spectra and Molecular Structure IV, Constants of Diatomic Molecules," Van Nostrand Reinhold, New York, 1979.
16. W. B. DeMore, S. P. Sander, D. M. Golden, R. F. Hampson, M. J. Kurylo, C. J. Howard, A. R. Ravishankara, C. E. Kolb, and M. J. Molina, "Chemical Kinetics and Photochemical Data for Use in Stratospheric Modeling JPL Publication 94-26," Jet Propulsion Laboratory, California Institute of Technology, Pasadena, 1994.
16. T. Carrington, Int. J. Chem. Kinet., **14**, 517 (1982)
18. J. Park and M. C. Lin, J. Phys. Chem., **100**, 3317 (1996)
19. S. P. Walch, J. Chem. Phys., **99**, 5295 (1993)

Table 1. Rate constants for vibrational relaxation of $NH_2(2_v)$.

Collision partner	k_1 [a]	k_2 [a]
CF_4	$(3.0\pm0.4) \times 10^{-11}$	$(6.3\pm1.0) \times 10^{-11}$
N_2 [b]	$< 6.0 \times 10^{-13}$	$< 1.4 \times 10^{-12}$

a. k_v denotes the rate constant for the vibrational relaxation from $NH_2(2_v)$ to $NH_2(2_{v-1})$. The values are in units of cm^3 $molecule^{-1}$ s^{-1}.

b. Upper limits determined from the intercept of Fig. 5.13 on the assumption that collision partner is only N_2.

Table 2. Rate constants for the total removal of $NH_2(2_v)$ by NO.

	k_0 [a,]	k_1 [a]	k_2 [a]
Gericke *et al.* [b]	$(1.4\pm0.1) \times 10^{-11}$	$(3.2\pm0.2) \times 10^{-11}$	-
NASA/JPL	1.7×10^{-11} [c]	-	-
	1.9×10^{-11} [d]	-	-
	0.9×10^{-11} [e]	-	-
This work	$(2.0\pm0.1) \times 10^{-11}$	$(2.6\pm0.3) \times 10^{-11}$	$(2.4\pm0.3) \times 10^{-11}$

a. k_v denotes the rate constant for the total removal of $NH_2(2_v)$ by NO. These values are in units of cm^3 $molecule^{-1}$ s^{-1}.

b. Reference 2. The value of k_0 agrees with the range of the average for the recommended value (NASA/JPL).[17]

c. Reference 17. Recommended value (T=298K) based on the average from 8.3 to 27.0×10^{-12} cm^3 $molecule^{-1}$ s^{-1} obtained various experimental technique.

d. Reference 17. Recommended value (T=298K) based on the results obtained by flash photolysis technique.

e. Reference 17. Recommended value (T=298K) based on the results obtained by the discharge flow technique.

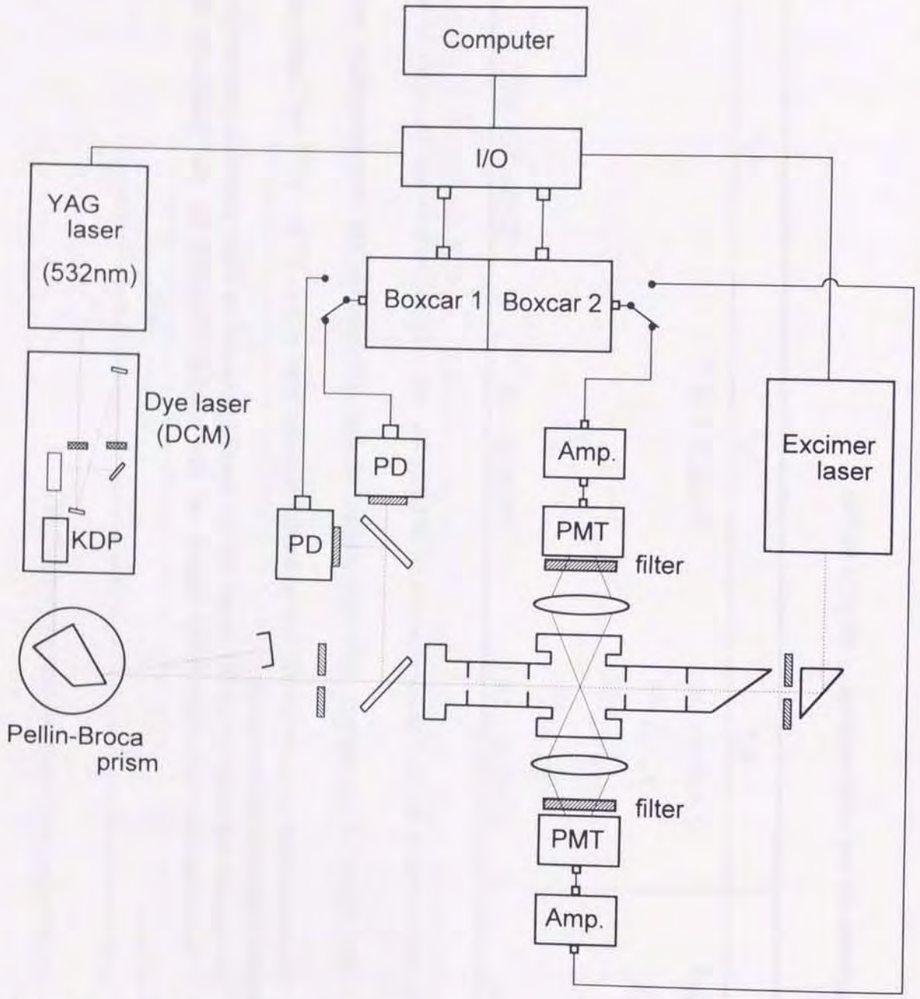

Fig. 5.1. A schematic diagram of the experimental apparatus.
I/O : computer interface, Amp. : home made amplifier, PMT : Photomultiplier, PD : Photodiode, and KDP : crystal for second harmonic generation.

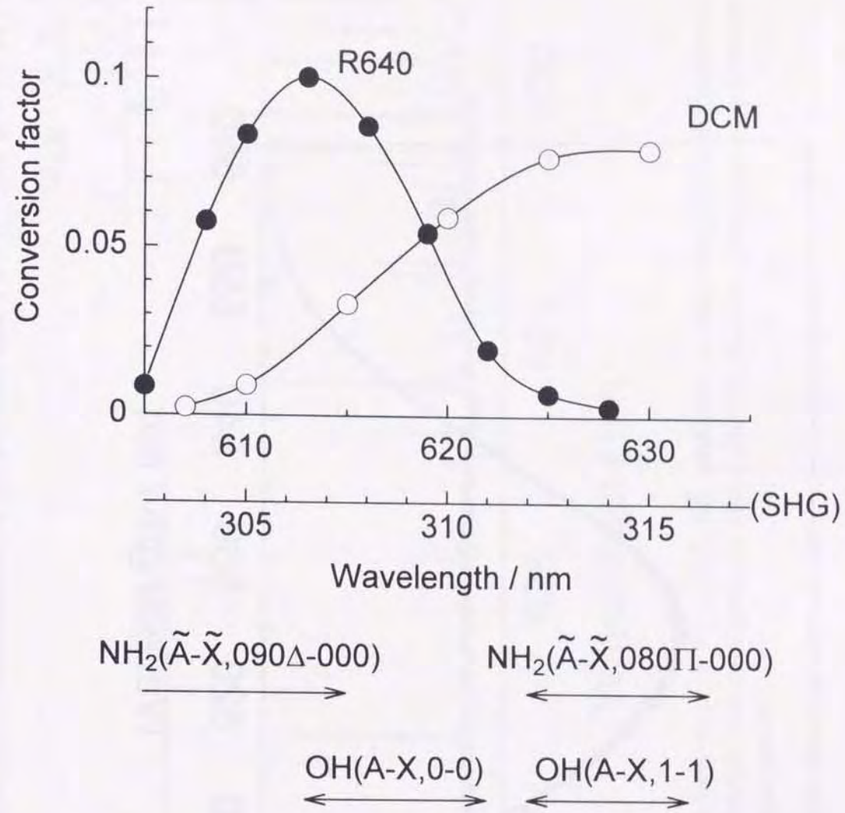

Fig. 5.2. Gain curves of DCM and Rhodamine 640 (R640) along with the range of excitation wavelengths of OH and NH_2. Concentrations of dye solutions were 0.175 g/l for DCM and 0.140 g/l for R640. The fluence of the pump laser (Nd^{3+}:YAG laser) was 80 mJ at 532 nm.

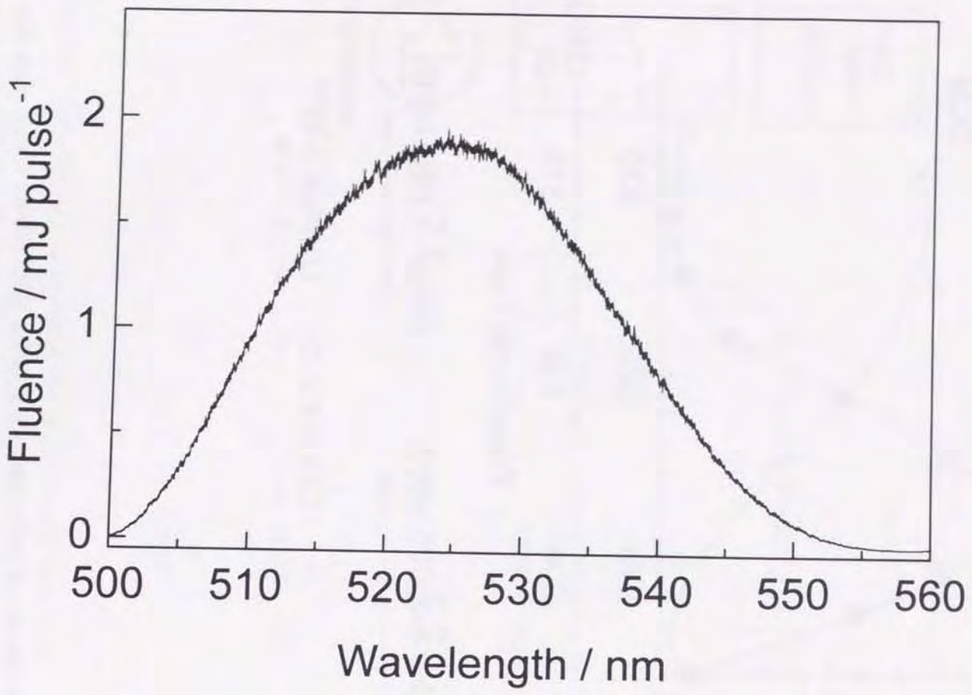

Fig. 5.3. A gain curve of Coumarine-522. Concentration of the solution was 1.4 g/l. The fluence of the pump laser (ND^{3+}:YAG laser) was 34 mJ pulse^{-1} at 355 nm.

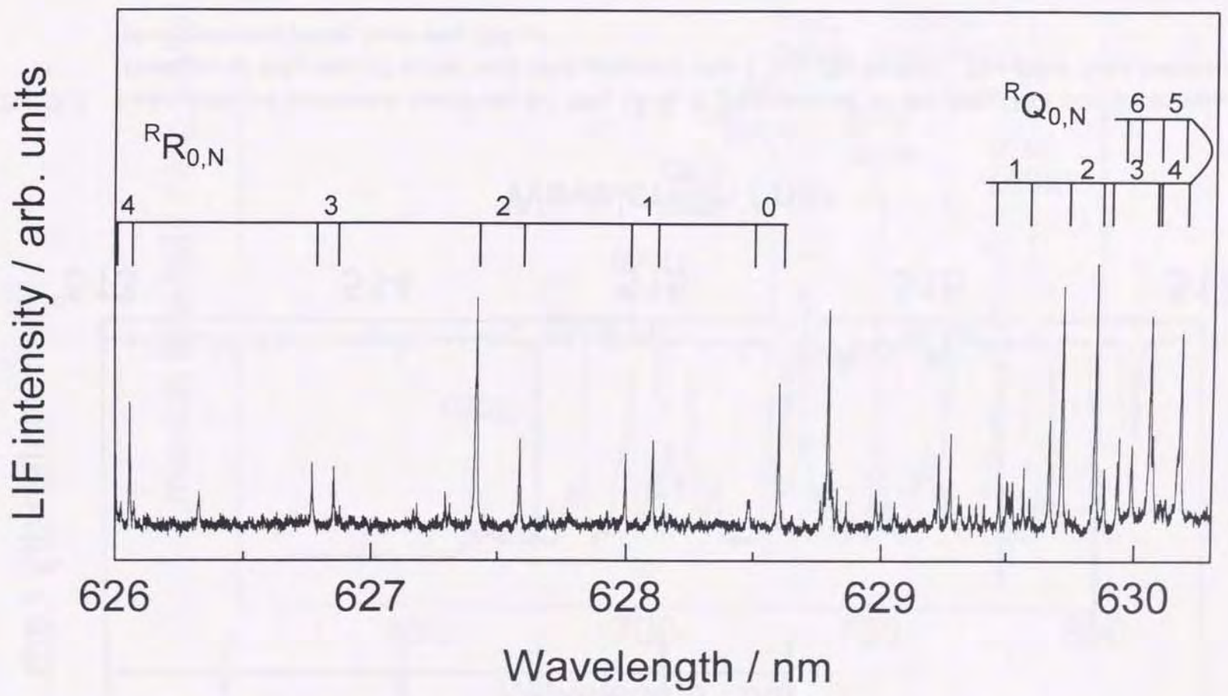

Fig. 5.4. Laser-induced excitation spectrum of NH_2 [$\tilde{A}$-$\tilde{X}$, 2^{8}_{0}] produced in the NH_3/193 nm photolysis. Pressure of NH_3 was 13 mTorr and total pressure was 1 Torr (N_2 buffer). The delay time between photolysis and probe lasers was 50 μs.

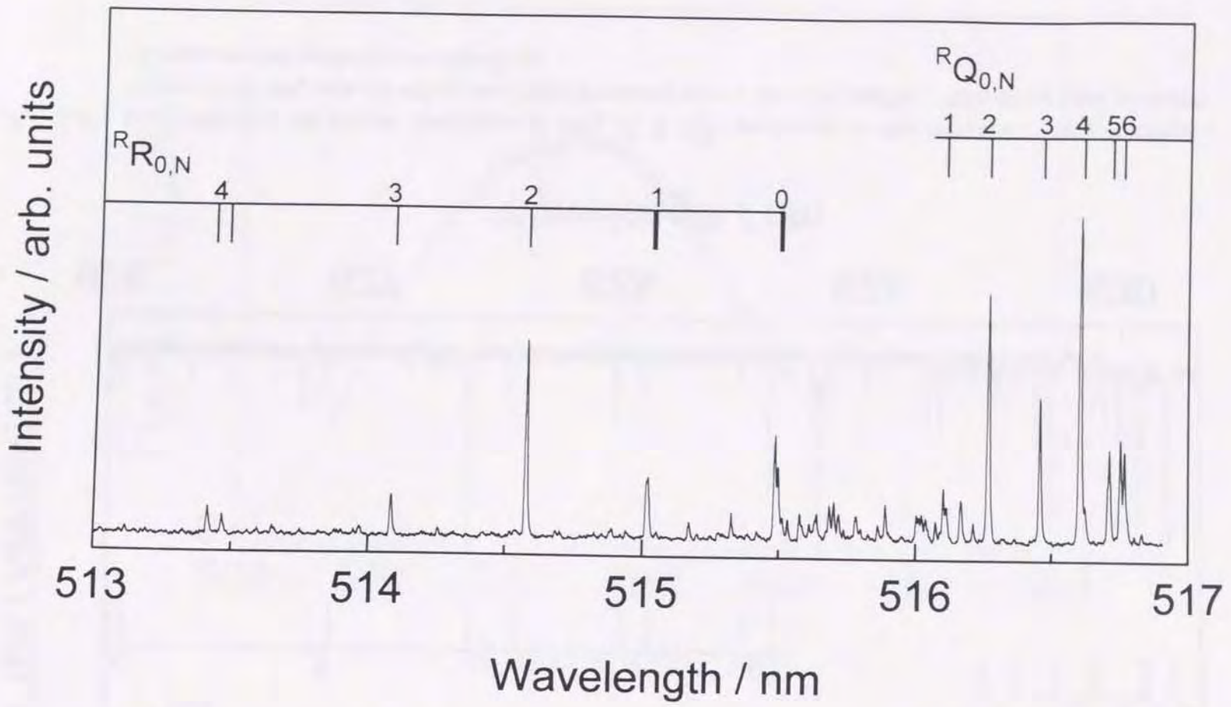

Fig. 5.5. Laser-induced excitation spectrum for NH_2 [$\tilde{A}$-$\tilde{X}$, 2^{12}_{0}] produced in the NH_3/193 nm photolysis. Pressure of NH_3 was 13 mTorr and total pressure was 1 Torr (N_2 buffer). The delay time between photolysis and probe laser was 100 μs.

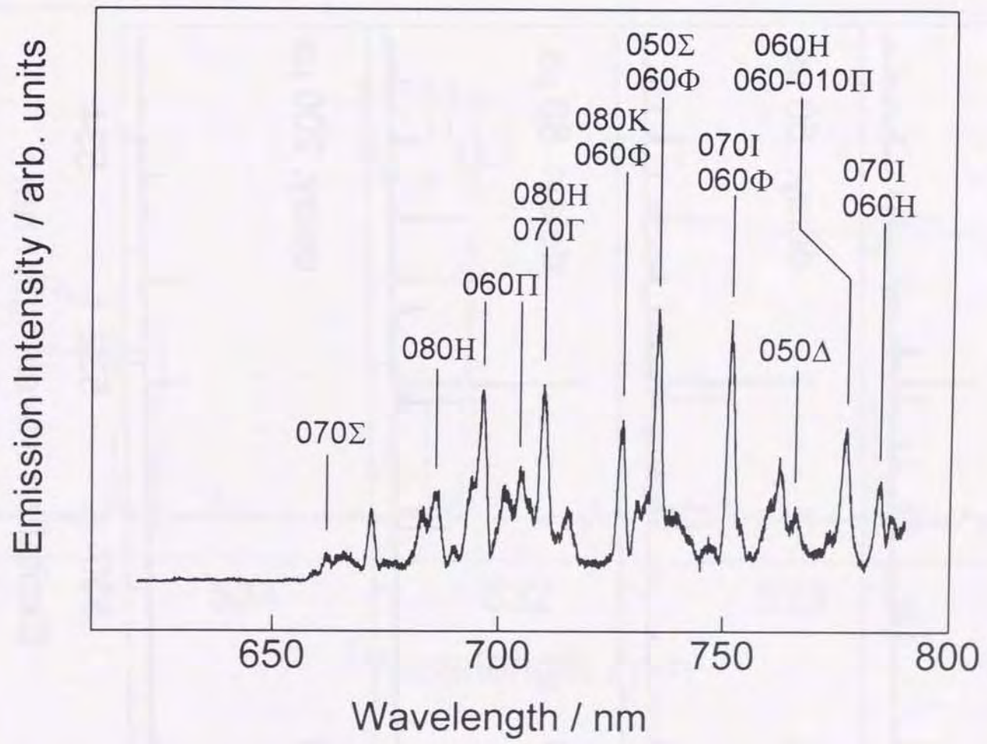

Fig. 5.6. Dispersed emission spectrum of the system of the NH_3/193 nm photolysis. The assignments, 0v0, correspond to the transitions NH_2($\tilde{A}$-$\tilde{X}$, 0v0-000). Pressure of NH_3 was 13 mTorr. Resolution of the monochromator was 5 nm (FWHM).

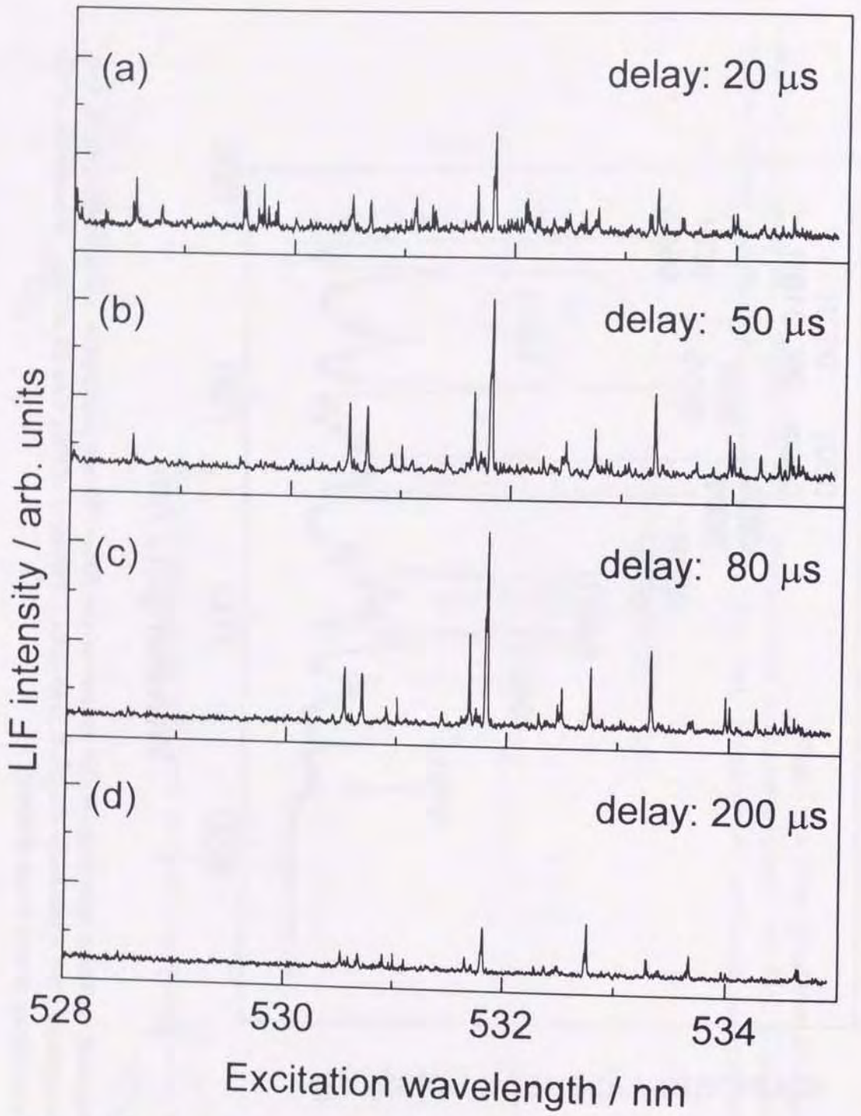

Fig. 5.7. LIF excitation spectra recorded at various delay time. Pressure of NH_3 was 13 mTorr. The delay time between photolysis and probe lasers were (a) 20 μs; (b) 50 μs; (c) 80 μs; (d) 200 μs.

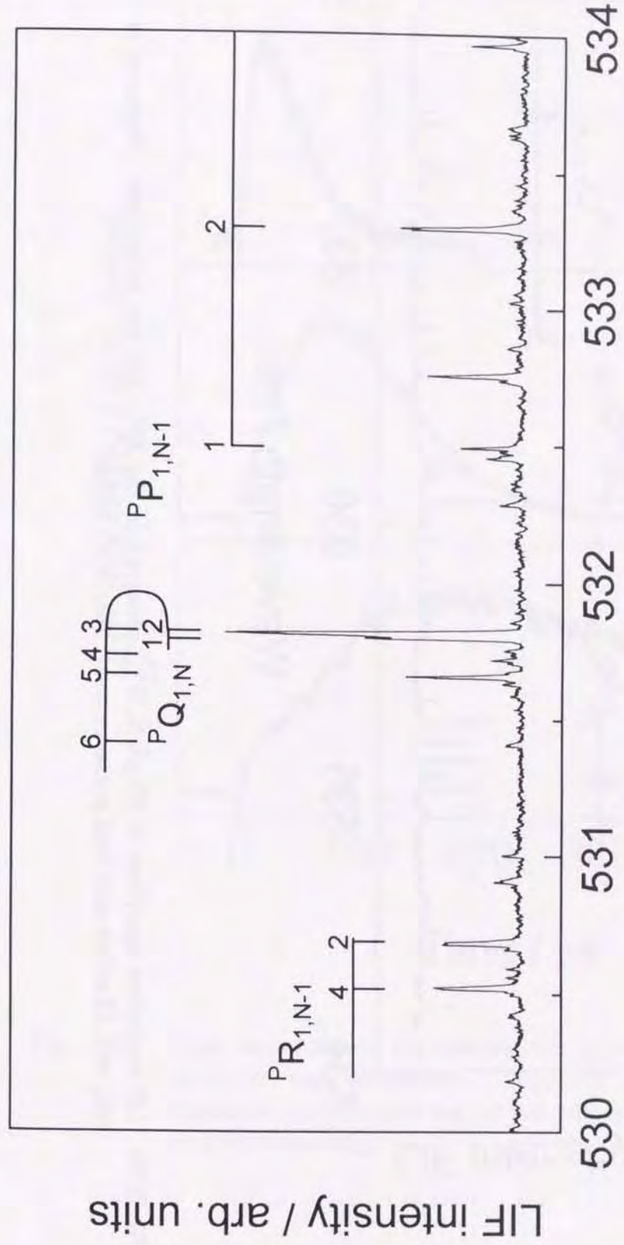

Fig. 5.8a. LIF excitation spectrum of $NH_2(\tilde{A}\text{-}\tilde{X}, 2_1^{13})$ observed in the NH_3/193 nm photolysis. Pressure of NH_3 was 13 mTorr and total pressure was 1 Torr of N_2 buffer.

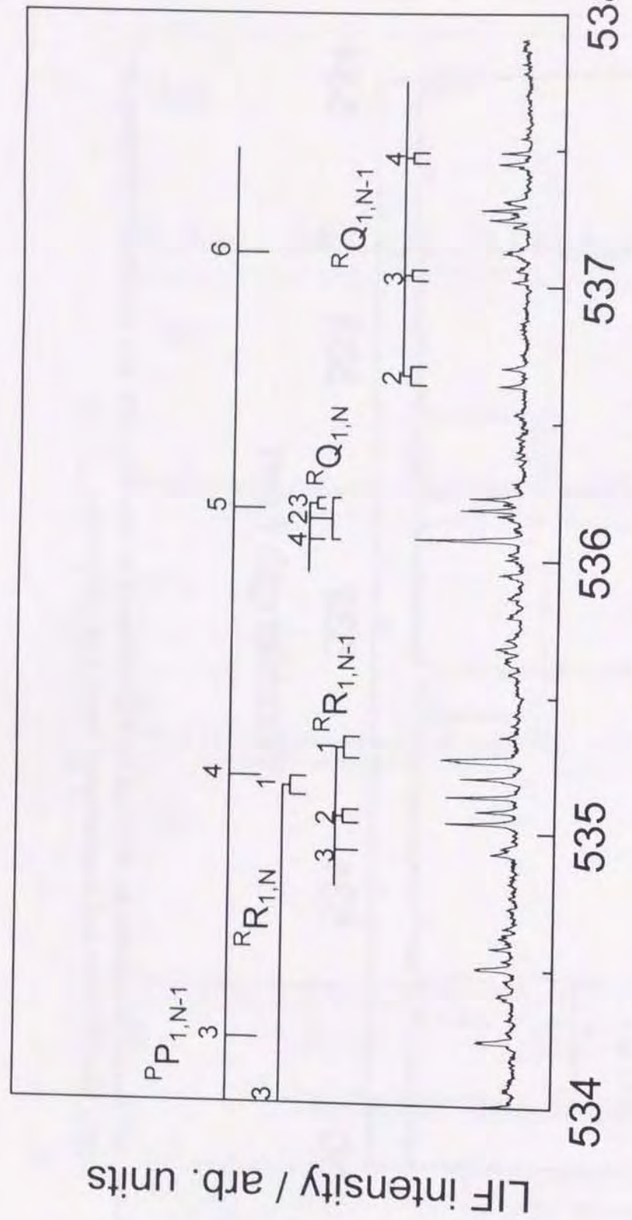

Fig. 5.8b. LIF excitation spectrum of $NH_2(\tilde{A}\text{-}\tilde{X}, 2_1^{13})$ observed in the NH_3/193 nm photolysis. Pressure of NH_3 was 13 mTorr and total pressure was 1 Torr of N_2 buffer.

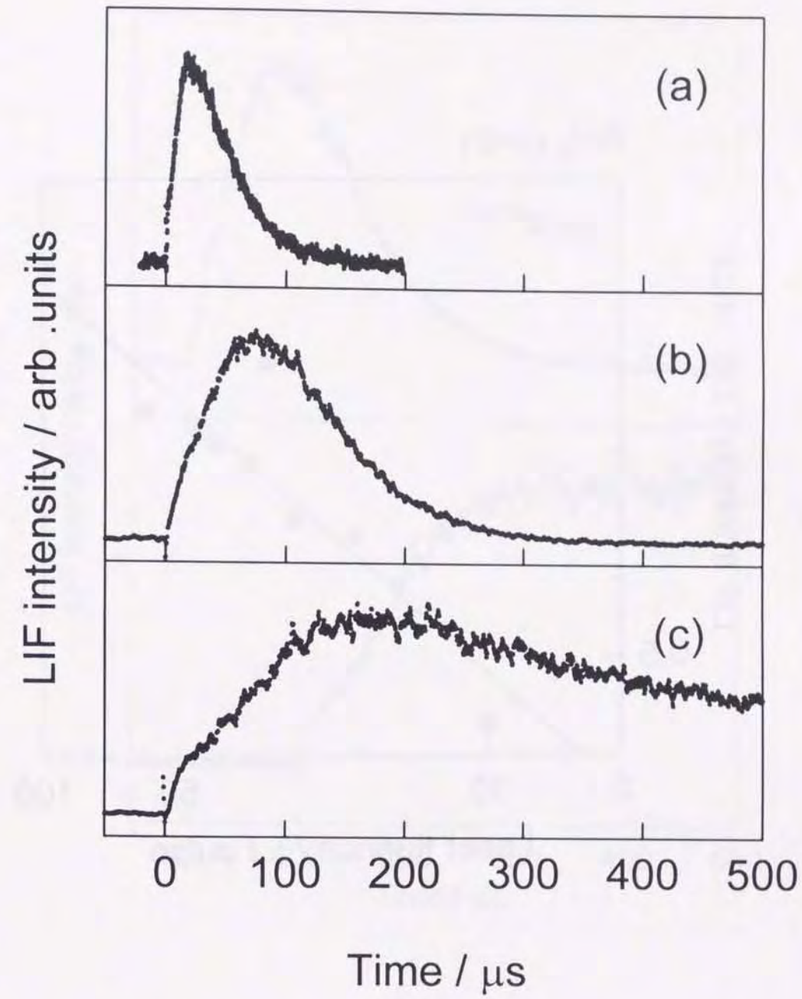

Fig. 5.9. Time dependence of vibrationally excited $NH_2(2_v)$ produced in NH_3/193 nm photolysis. Pressure of NH_3 was 13 mTorr. Excitation wavelengths are (a) 528.560 nm (2_2); (b) 531.818 nm (2_1); (c) 514.570nm (0_0).

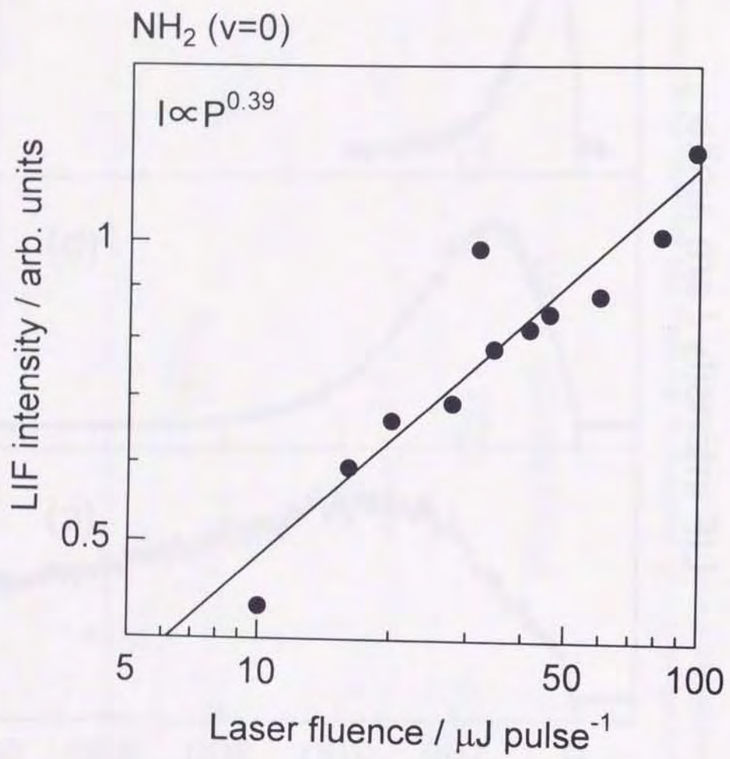

Fig. 5.10. Laser fluence dependence of the LIF signals of NH_2 [$\tilde{A}$-$\tilde{X}$, 2^8_0]. Excitation wavelength was 627.428 nm ($^RR_{0,2}$)

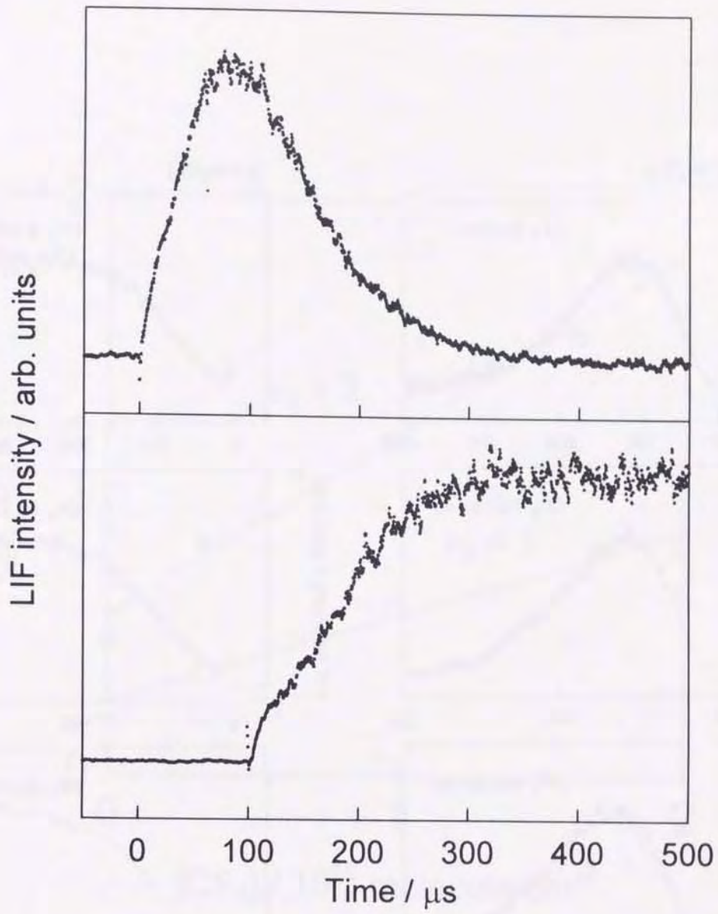

Fig. 5.11. Corrected profiles of $NH_2(2_1$ and $0_0)$ multipled by $\exp(k_d t)$. Upper is $NH_2(2_1)$; lower is $NH_2(0_0)$. Both profiles are so drawn that they have the same maximum intensity.

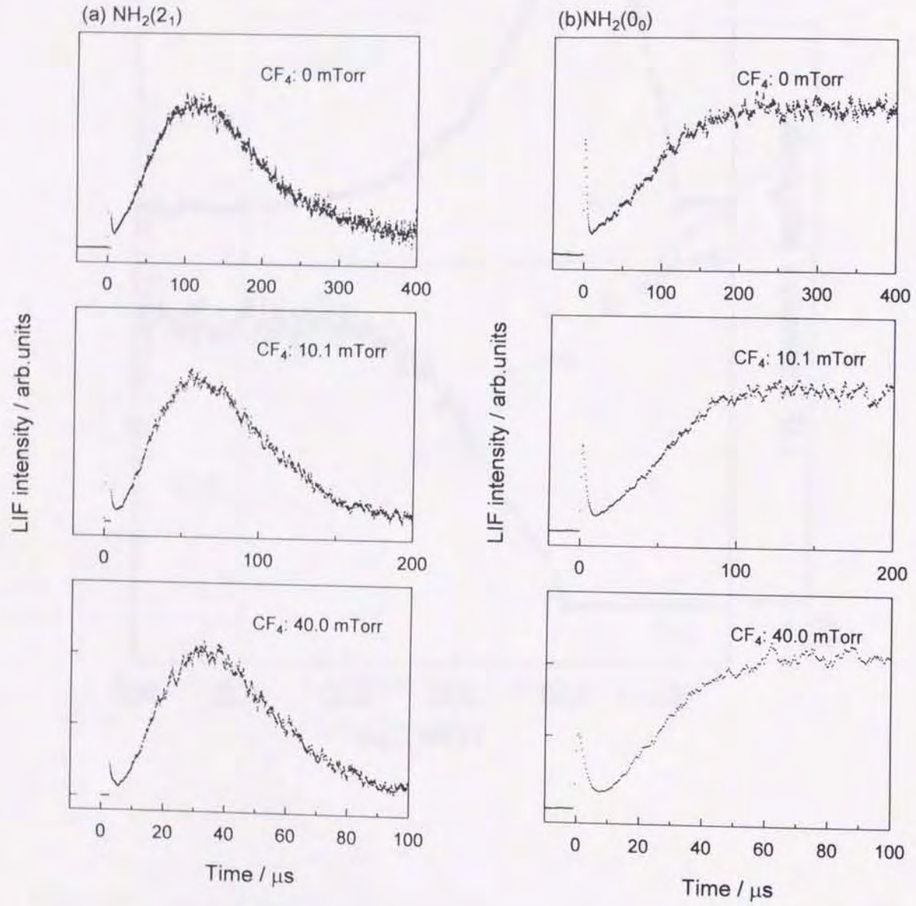

Fig. 5.12. Time dependent profiles of (a) $NH_2(2_1)$ [left column] and (b) $NH_2(0_0)$ [right column] at various pressures of CF_4. The pressures of CF_4 are 0 mTorr(upper); 10.1 mTorr (middle); 40.0 mTorr (lower) of each plot.

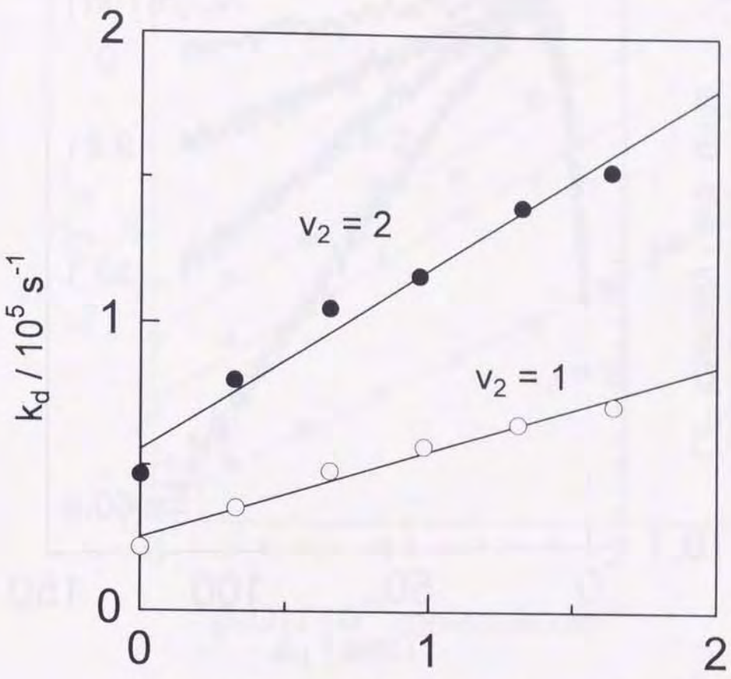

Fig. 5.13. Plot of the first-order decay rates of LIF ($NH_2(2_2$ and $2_1)$) versus concentration of CF_4.

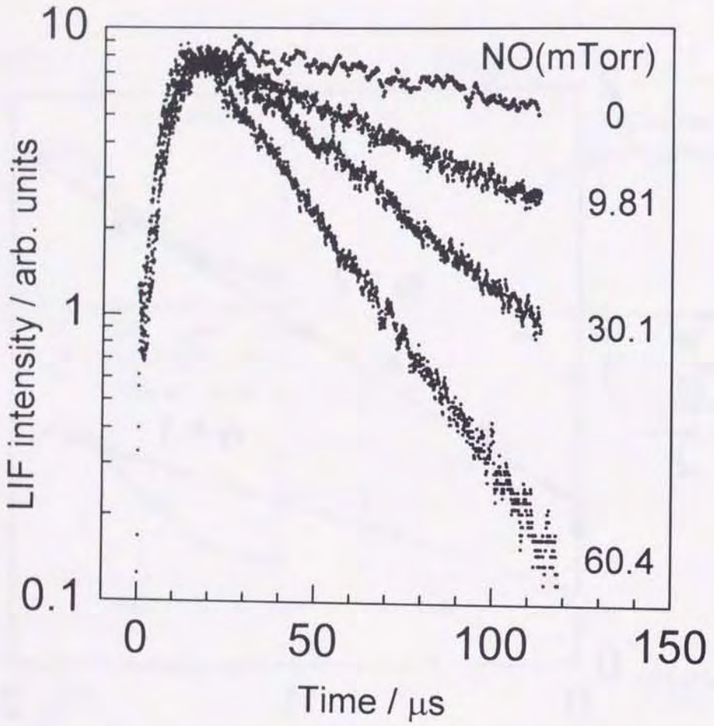

Fig. 5.14 Time dependence of temporal profiles of $NH_2(0_0)$ at various concentrations of NO. Pressure of NH_3 was 13 mTorr. CF_4 of 250 mTorr was added to accelerate the relaxation of upper vibrational levels of NH_2.

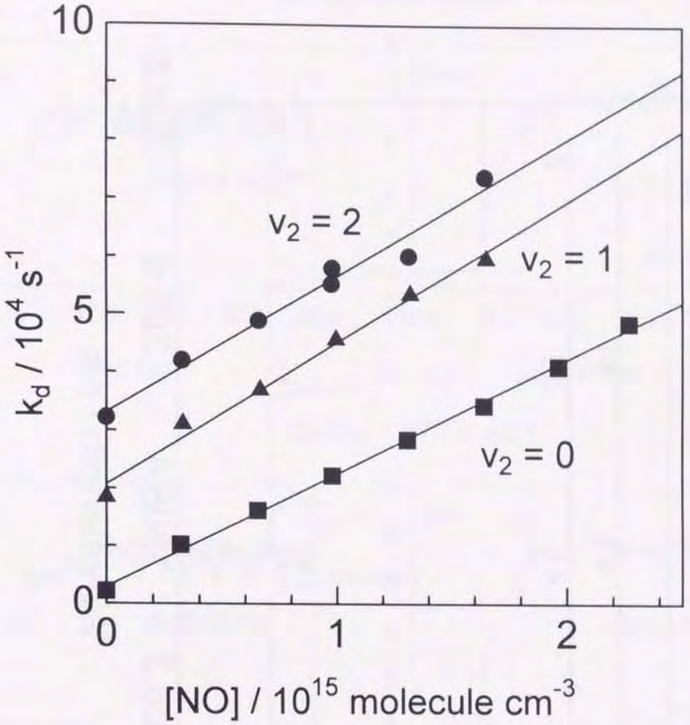

Fig. 5.15 Dependence of the first-order decay rates of $NH_2(2_v)$ on the concentration of NO.

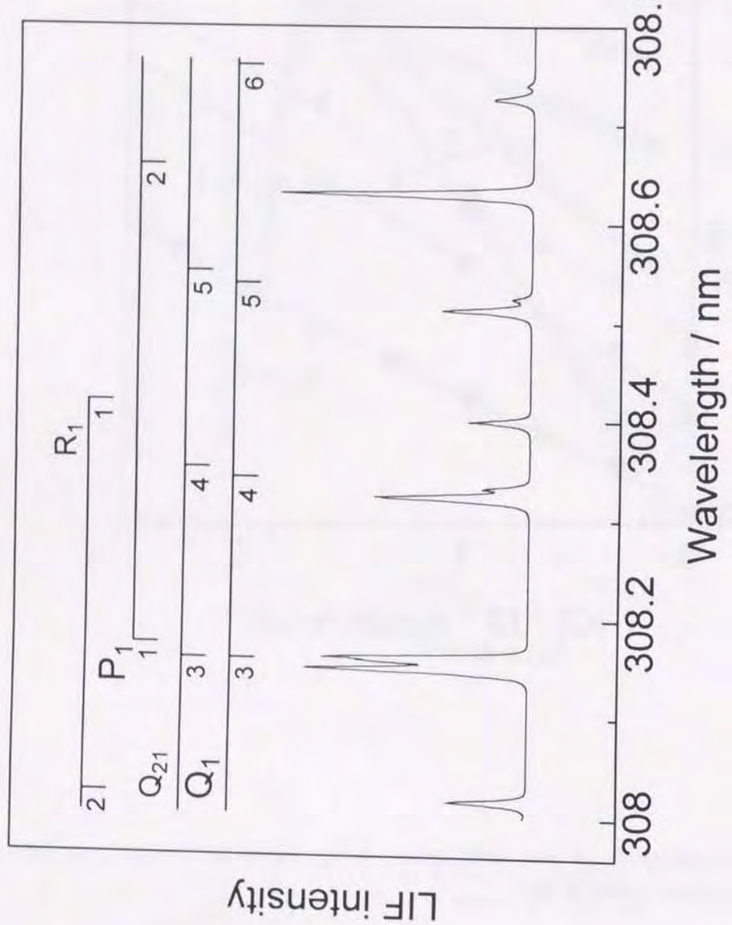

Fig. 5.16. LIF excitation spectrum of OH ($A^2\Sigma$ - $X^2\Pi_i$, 0-0) produced in NH_2+NO reaction. Pressure of NH_3 was 13 mTorr and NO was 20 mTorr. Delay time between photolysis and probe laser was 100 μs.

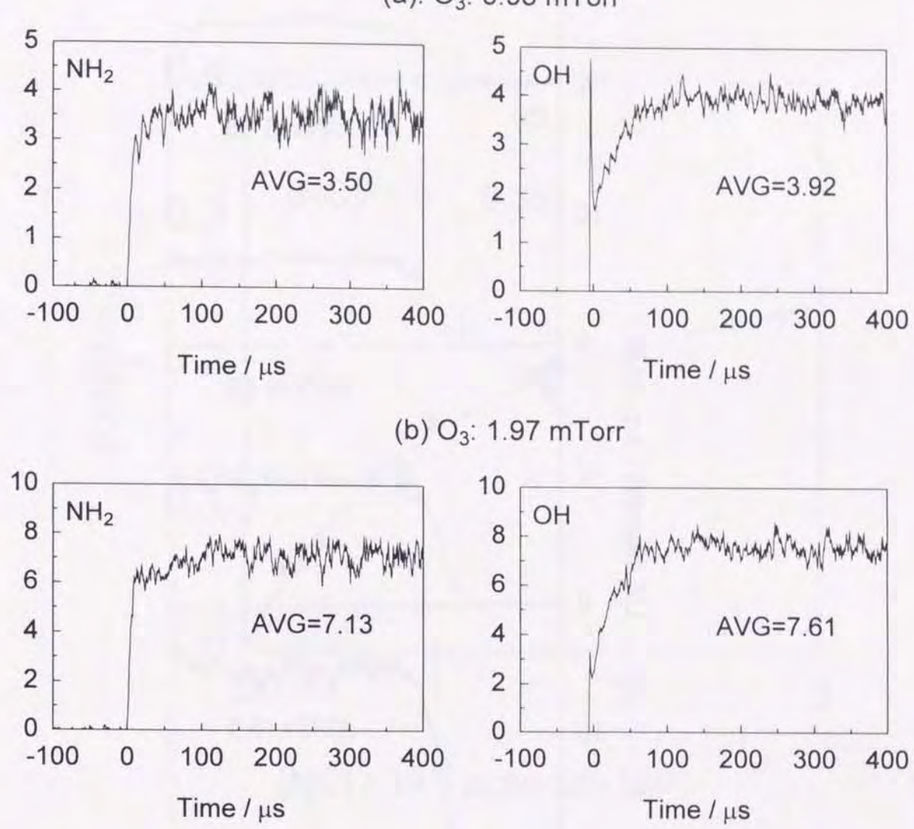

Fig. 5.17. Corrected profiles for calibration of LIF intensities of OH(A-X, 0-0) and $NH_2(\tilde{A}\text{-}\tilde{X}, 2^8_0)$ produced in $O(^1D) + NH_3$ reaction: (a) pressure of O_3 is 0.98 mTorr; (b) 1.97 mTorr. The ratio of LIF intensities was determined to be 0.95. The values of AVG in the figures are averages from 150 to 400 μs

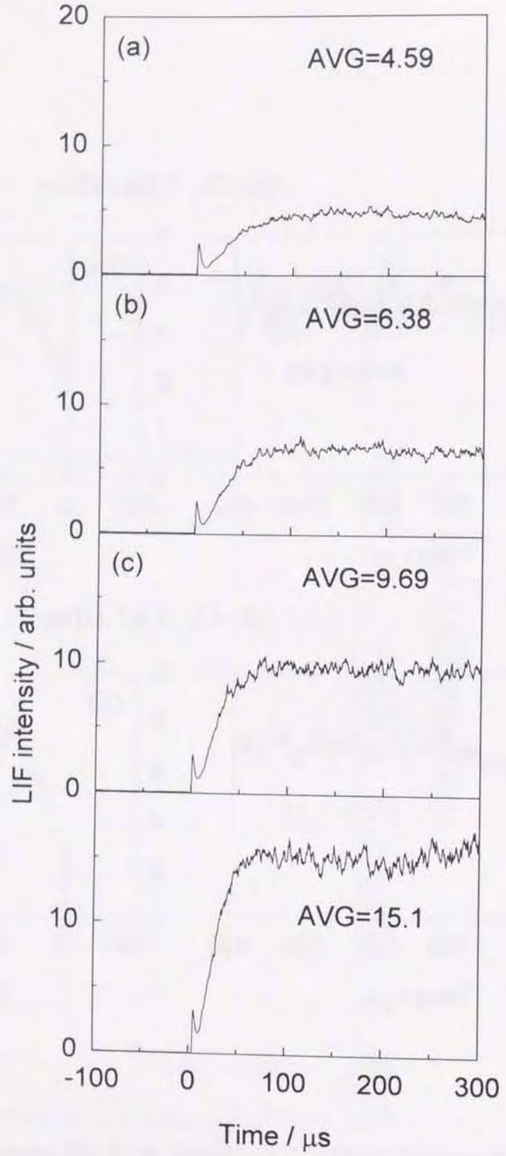

Fig. 5.18. Temporal profiles of OH produced in the reaction of NH_2+NO at various concentration of NO. Pressures of NO were: (a) 6.22 mTorr; (b) 12.3 mTorr; (c) 25.4 mTorr; (d) 48.7 mTorr.

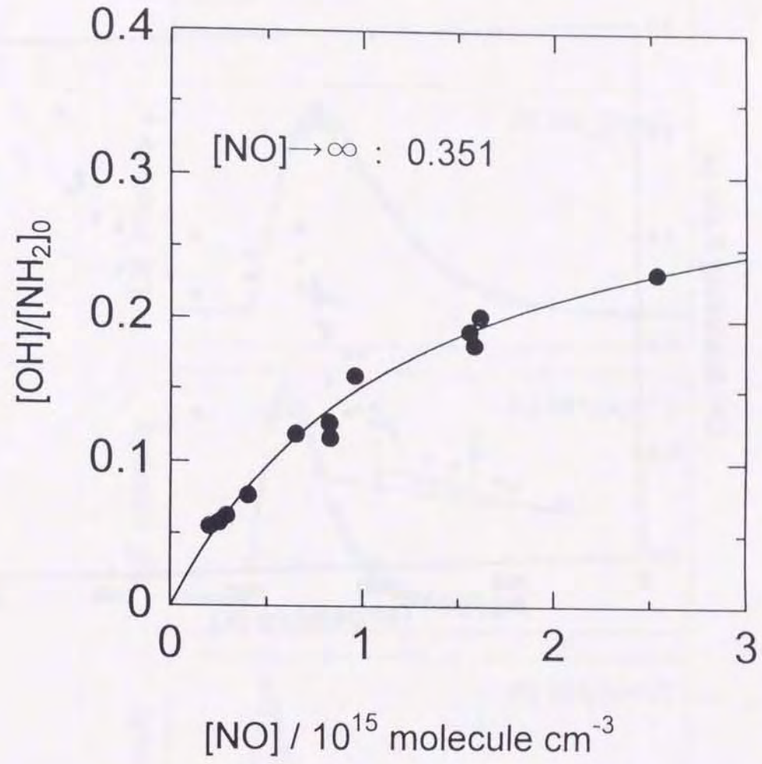

Fig. 5.19. The yield of OH in the reaction of NH_2+NO obtained by $[NO] \rightarrow \infty$ in eq. (10).

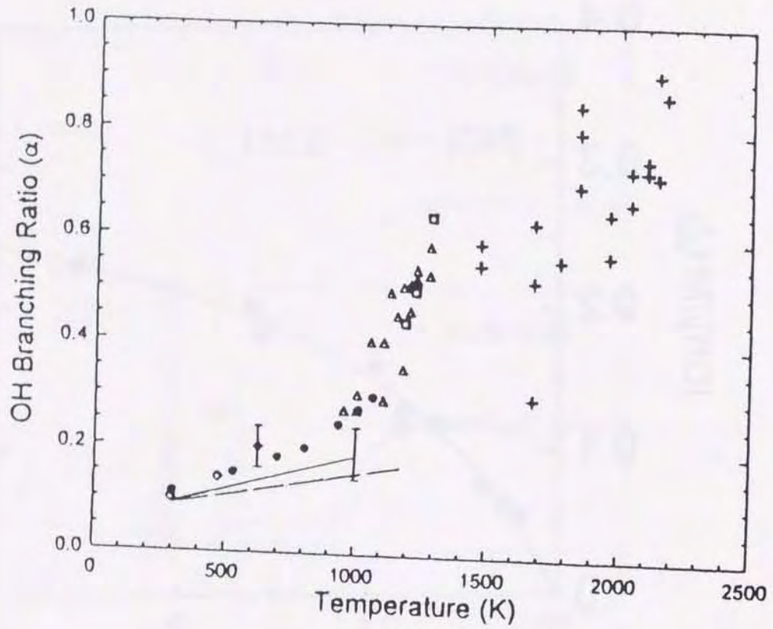

Fig. 5.20. Temperature dependence of α reported by various groups, summarized by Park and Lin.[18]

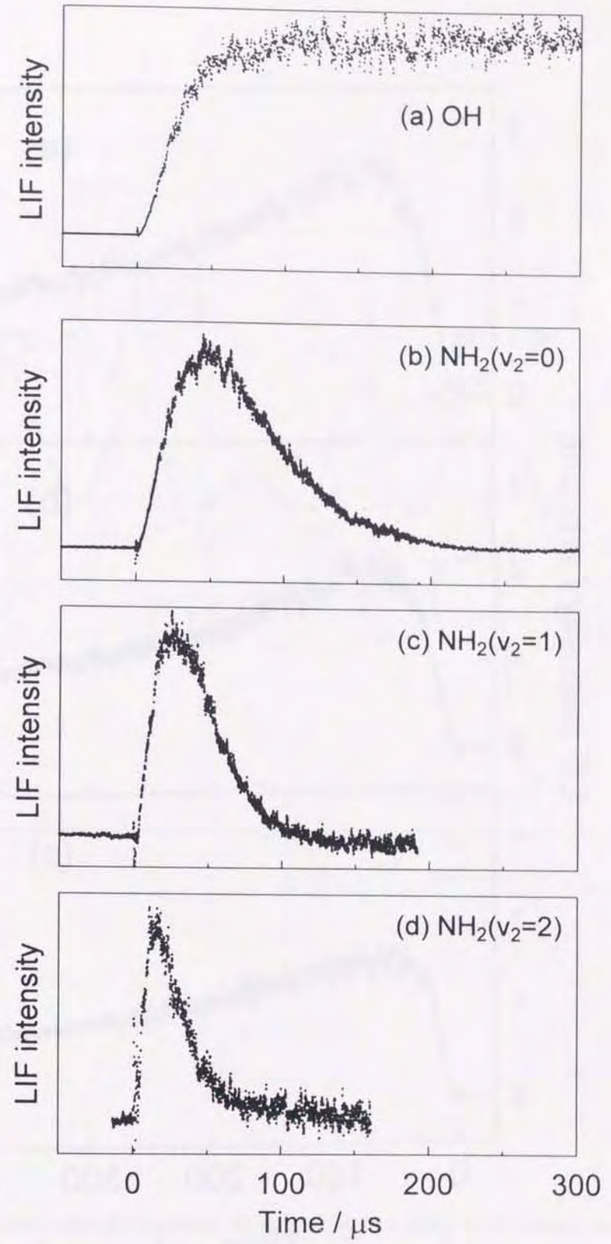

Fig. 5.21. Time dependent profiles for $NH_2(2_v)$ and OH produced in the NH_3 / NO / 193nm photolysis system. $P(NH_3)$=13 mTorr: P(NO)=40 mTorr.

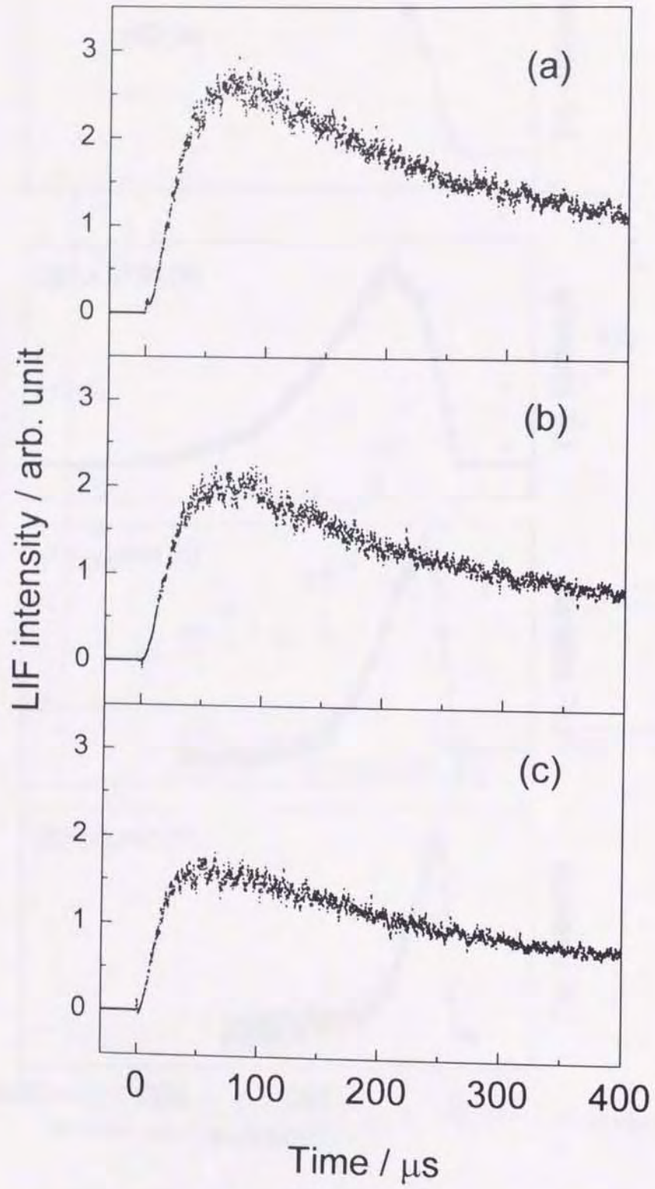

Fig. 5.22. Dependence of the profile of OH on the pressure of CF_4. P_{NO}=20 mTorr, and (a) 0 mTorr; (b) 10 mTorr; (c) 40 mTorr of CF_4.

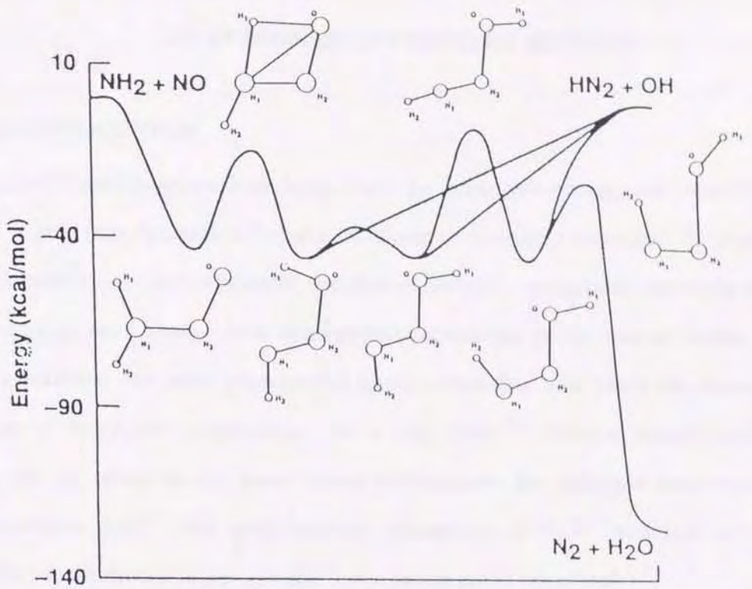

Fig. 5.23. Potential energy surface diagram for the NH_2 + NO reaction based on the CASSCF/ICCI calculation by Walch.[19]

CHAPTER 6 A NEW METHOD OF DETERMINING THE RATE CONSTANTS FOR STATE-TO-STATE VIBRATIONAL RELAXATION: AN INTEGRATED PROFILES METHOD

6.1 INTRODUCTION

Laser spectroscopy has been used to great advantage not only in the fields of reaction dynamics but also in those of chemical kinetics.[1-3] Study of the chemistry of non-emissive electronic states —a typical example is an electronic ground state— has been greatly advanced by the use of lasers. Not only reactions but also vibrational energy transfer has been an important subject of extensive experiments for a long time.[4] Since a single quantum level can be observed by laser-based techniques, for example laser-induced fluorescence (LIF)[5] and multiphoton ionization (MPI),[6,7] studies on state specific vibrational energy transfer have made great progress.

Temporal profiles of all the vibrational levels associated with energy transfer must be observed and analyzed to extract the information on the rate constant for each level. An ordinary way of analysis is non-linear fit by analytical solutions or numerical integration of rate equations. Fitting parameters are determined so that observed profiles are reproduced well. An initial trial set of parameters of concentrations and rate constants have to be given prior to the ordinary analyses. Unfortunately, results frequently depend on the initial trial set of parameters; therefore, rate constants are not always determined unequivocally. A new method is introduced in this paper to resolve the problems of the conventional analyses. Since regression

equations are linearized, parameters in the analysis, i.e., rate constants and relative detection sensitivities, are determined unambiguously.

A knowledge of relative populations among vibrational levels is helpful in some cases to perform non-linear analysis. Laser-induced fluorescence excitation spectra are usually recorded to obtain vibrational distributions of the molecules of interest. In the analysis of the spectra, various factors related to photochemical properties of the molecules have to be applied for correcting the spectra.[8,9] Franck-Condon factors and the dependence of transition dipole moment on the vibrational levels (r-centroid dependence of transition dipole) have to be taken into account to derive correct intensities of the transitions. In addition, information on the dependence of fluorescence quantum yield of each rotational line observed is also indispensable for correction. Furthermore, rates of predissociation and quenching, which reduce the LIF intensity, are known to depend on rotational quantum numbers.[10-13] If fluorescence lifetimes are different among rotational levels, the overlap between fluorescence decay curves and the sampling gate of an integrator (fixed boxcar) should also be corrected.[14] Optical filters are frequently used in LIF experiments to block the stray light of the photolysis and probe lasers. Since spectral distributions of the fluorescence from different vibrational levels are not the same, the overlap between the fluorescence and the filters used has to be corrected. Unfortunately, there are few cases in which all the precise factors described above are available.

Not only the rate constants of vibrational relaxation but also relative detection sensitivities are obtained simultaneously in the analysis introduced in this chapter. Since the time-evolutions of relative concentrations among

all the levels are obtained, the initial relative populations on the levels as the products of preceding photolysis or reaction can be determined. The difference between the present method and the conventional analyses will be shown and how the method is to be applied to realistic systems will be described in detail.

6.2 NEW METHOD

Conventional non-linear analyses

First, consider a process of vibrational relaxation

$$A \xrightarrow{k_1} B \xrightarrow{k_2} C, \qquad (1)$$

where A, B, and C are different vibrational levels: for example A represents a vibrational level $v = 2$, B is $v = 1$, and C is $v = 0$. As often seen in textbooks,[14-16] temporal profiles of the concentrations of each species are given under the initial conditions: $[A]_{t=0} = [A]_0$, $[B]_{t=0} = [C]_{t=0} = 0$,

$$[A] = [A]_0 \exp(-k_1 t) \qquad (2)$$

$$[B] = \frac{k_1[A]_0}{k_1 - k_2}\left[\exp(-k_2 t) - \exp(-k_1 t)\right] \qquad (3)$$

$$[C] = [A]_0\left\{1 - \frac{1}{k_1 - k_2}\left[k_1 \exp(-k_2 t) - k_2 \exp(-k_1 t)\right]\right\}. \qquad (4)$$

The initial concentrations except $[A]_0$ are zero for the sake of simplicity and

this assumption loses neither rigorousness nor generality. Concentration of A shows a single-exponential decay and that of B shows double-exponential profile with growth and decay. The rate constant k_1 is determined by an ordinary semilogarithmic plot of [A] vs. t. Another rate constant k_2 seems to be obtained from a semilogarithmic plot of [B] at large t over which $exp(-k_2t)$ is sufficiently larger than $exp(-k_1t)$. This type of analysis, however, is possible only when $k_1 > k_2$. It should be noted that the terms $exp(-k_1t)$ and $exp(-k_2t)$ do not always govern decay and growth, respectively. If $k_1 < k_2$, not k_2 but k_1 is derived from the semilogarithmic plot of the decay part of [B].

The intensity of a signal is not readily converted to an absolute concentration even when the intensity is proportional to the absolute concentration. Thus, unknown proportionality constants are always present to associate the observed signal intensities with absolute concentrations, for example $I_A = \alpha$[A], where I_A represents the observed signal intensity of LIF or MPI due to a single rotational transition of the species A, and α is a proportionality constant (detectivity of the apparatus) for the species A. As long as rotational motion is equilibrated with the ambient temperature, the population on each vibrational level of interest can be monitored by a signal due to a rotational transition. When the absolute concentrations in equation (3) are substituted with corresponding signal intensities, $I_A = \alpha$[A] and $I_B = \beta$[B], the following equation is obtained

$$I_B = \frac{\beta}{\alpha}\frac{k_1 I_{A_0}}{k_1 - k_2}\left[exp(-k_2t) - exp(-k_1t)\right], \qquad (5)$$

where I_{A_0} is a signal intensity of A at $t = 0$ and the factor β/α is a relative

sensitivity of the species A and B. Since the relative sensitivity β/α is unknown, not only rate constants but also a scaling factor must be determined in the analysis. Because the time dependence of the profile of B is represented by the term $exp(-k_2t)$-$exp(-k_1t)$, and growth always corresponds to the faster process and decay corresponds to the slower one in scheme (1), observed profile I_B is fit to the following form:

$$I_B = C\left[exp(-k_{decay}t) - exp(-k_{growth}t)\right] \quad (C > 0) \qquad (6)$$

using non-linear double-exponential least-squares fit.[17-19] Even when k_{growth} and k_{decay} are determined by the analysis using equation (6), there is no way to decide which of k_{growth} or k_{decay} corresponds to k_1 or k_2 from only the analysis of I_B. Since rate constant k_1 is separately determined by the profile (decay) of A, it seems to be possible to conclude which of k_{growth} or k_{decay} is k_1 or k_2. However, double-exponential analysis frequently fails to obtain correct k_{growth} and k_{decay} particularly when the rate constants are not much different. Carrington[20] gave a criterion for profiles to be reliably analyzed by the non-linear double-exponential least-squares fit:

$$\left|k_{growth} - k_{decay}\right| \cdot t_{max} \geq 1\,, \qquad (7)$$

where t_{max} is the maximum time over which the signal of B can be observed (that is, distinguished from background noise). Equation (7) indicates that the rate constants are not precisely determined from the profiles with $k_{growth} \approx k_{decay}$, because the actual signal at very large t is too weak to observe with good signal-to-nose (S/N) ratio. Therefore, the k_1 obtained from the profile of A is in agreement with neither k_{growth} nor k_{decay}, and thus k_2 cannot be

determined. When a profile with k_1 a little larger than k_2 is analyzed, the order of magnitude of the rate constants is $k_{decay} < k_2 < k_1 < k_{growth}$ as shown later.

The profile of B in scheme (1) with rate constants $k_1 = 4.0\times10^3$ s^{-1} and $k_2 = 3.8\times10^3$ s^{-1} was synthesized as shown in Fig. 6.1(a) and analyzed by non-linear regression method. For simplicity, the initial concentration of B was set to be zero ($[B]_0 = 0$). First, non-linear least squares fit was performed on the assumption that k_{growth} and k_{decay} correspond to k_1 and k_2, respectively. The initial trial values of k_{growth} and k_{decay} for the iterative calculations have to be given with the greatest care, because results are dependent on the initial values in non-linear analysis. We shall henceforth write the initial values of k_{growth} and k_{decay} by k^o_{growth} and k^o_{decay} to avoid confusion. The value of k^o_{decay} was first determined from a semilagarithmic plot (ln[B] vs. t) of the data shown in Fig. 6.1(a) over large t. In principle, more accurate value of k^o_{decay} is obtained from the slope at larger t; however, actually observed signal at large t cannot be analyzed because of noise on the data. When a S/N ratio is 10, signal is behind noise after the time at which the intensity is smaller than 1/10 of the maximum. The k^o_{decay} was determined to be 2.439×10^3 s^{-1} from the slope of a semilogarithmic plot in the range of 0.5 - 1 ms. When the S/N ratio increased up to 100, the analysis of the data in the range from 1.5 ms to 2 ms gave k^o_{decay} to be 3.300×10^3 s^{-1}. The value of k^o_{growth}, on the other hand, was determined by the curve generated from equation (6) multiplied by a term $exp(+k^o_{decay}t)$. The maximum value of the profile transformed from equation (6) was regarded as the asymptote in the determination of k^o_{growth}, and the values of k^o_{growth} were given to be 6.839×10^3 s^{-1} and 4.992×10^3 s^{-1} for

S/N = 10 and 100, respectively. The initial value of the scaling factor C was so obtained that the maximum value of equation (6) was the same as that of the analyzed data. A resulting curve obtained using the initial parameters for S/N = 100 with permissible error of 2 % is shown in Fig. 6.1(b). The curve appears to reproduce the data shown in Fig. 6.1(a); nevertheless, the rate constants finally obtained in the analysis, $k_{growth} = 4.655\times10^3$ s^{-1} and $k_{decay} = 3.297\times10^3$ s^{-1}, diverge substantially from the correct rate constants $k_1 = 4.0\times10^3$ s^{-1} and $k_2 = 3.8\times10^3$ s^{-1}. The values obtained for S/N =10, $k_{growth} = 4.657\times10^3$ s^{-1} and $k_{decay} = 3.295\times10^3$ s^{-1}, are also significantly different from the correct values.

Another type of fit was performed to resolve the problem in non-linear double-exponential on the assumption that the rate constant k_1 was determined first by the analysis of the profile of A. Because the k_1 has to be in agreement with k_{growth} or k_{decay}, one of the rate constants in equation (6) was fixed to the value of k_1, after which the other rate constant and the factor C were optimized to reproduce the analyzed data. This type of analysis, however, also has a problem. Since the difference between k_1 and k_2 is not known, which of k_{growth} or k_{decay} corresponds to k_1 is not obvious. Naturally, correct rate constant k_2 was obtained when the k_{growth} in equation (6) was replaced with k_1 in the analysis of the profiles with $k_1 > k_2$ or the k_{decay} was replaced with k_1 for the profiles with $k_1 < k_2$. When the profiles with correct rate constants $k_1 > k_2$ were analyzed by equation (6) whose initial parameter of k_{decay} was assumed to be k_1, resulting k_2 was incorrect. When the k_{decay} was replaced with k_1, the value of k_{growth} obtained by non-linear double-exponential analysis was adopted as k^o_{growth}. Figure 6.1(c) shows a

resulting curve obtained by the incorrect substitution, i.e., $k_{decay} = k_1$. The rate constants k_{growth} obtained are 4.127×10^3 s^{-1} for both S/N = 10 and 100. The values are widely different from correct k_2 (= 3.8×10^3 s^{-1}); nevertheless, the curves shown in Figs. 6.1(a) and 6.1(c) are too similar to distinguish any difference. Correlation coefficients of the curves in Figs. 6.6(b) and 6.6(c) are larger than 0.999. This fact indicates that non-linear fits are not effective particularly when the difference between k_1 and k_2 is not large.

When the k_1 is exactly the same as k_2 ($k_1 = k_2 = k$), equation (3) must be replaced by a different expression:

$$[B] = k[A]_0 t\, exp(-kt). \tag{8}$$

Equation (8) is an mathematically asymptotic form of (3) as $(k_1\text{-}k_2) \rightarrow 0$; however, the values of the equation (3) as $(k_1\text{-}k_2) \rightarrow 0$ cannot be correctly evaluated by a computer, because both denominator and numerator are close to zero.

An integrated profiles method

A new analysis introduced in the present paper will be described in this section. First, consider the analysis of time-dependent profiles of A, B, and C in scheme (1). Integration of rate equations from $t = t_0$ to an arbitrary time t gives the following expressions:

$$[A] = [A]_0 - k_1 \int_{t_0}^{t} [A]dt \tag{9}$$

$$[B] = [B]_0 + k_1 \int_{t_0}^{t} [A]dt - k_2 \int_{t_0}^{t} [B]dt \tag{10}$$

$$[C] = [C]_0 + k_2 \int_{t_0}^{t} [B]dt\,, \tag{11}$$

where $[A]_0$, $[B]_0$, and $[C]_0$ are the concentrations of A, B, and C at $t = t_0$. How to decide appropriate lower limits (t_0) of the integrals will be described later. These equations appear to be trivial as solutions for rate equations from a mathematical point of view. They, however, offer a great advantage for the analysis of temporal profiles for schemes more complicated than (1). Analytical solutions (3) and (4) are valuable to see the time evolution of concentrations of the species when the initial concentrations and rate constants are known. Equations (10) and (11), on the other hand, are useful in the analysis by which the rate constants and the initial populations of the levels are determined from temporal profiles observed in experiments. It is not difficult to calculate the integrals because the concentrations at each data point (i.e., time) can simply be summed up with a computer. A few significant characteristics of the equations should be noted. First, in contrast to the analysis using equation (3), simple linear regression is possible to determine the rate constants unequivocally. Second, the ambiguity of the non-linear analysis can be eliminated not only because k_1 and k_2 cannot be exchanged in equation (10) but also because an initial trial set of parameters is not necessary. Third, equation (10) is always satisfied as long as the relation between A and B is represented by scheme (1), even if the temporal profile of [A] in equation (10) is not given by such a formula as equation (2).

An additional feature is that the lower limits of the integrals of equations (9), (10), and (11) are not $t = 0$ but t_0. The signals at $t = 0$ are not always necessary to determine the rate constants and the relative sensitivities.

There are many unfortunate cases in which noise from the photolysis (or pump) laser at $t = 0$ is so large that the signal at around $t = 0$ is not reliable. A new arbitrary time t_0 ($\neq 0$) can be chosen as the lower limit of the integrals in order to exclude the contaminated signals around $t = 0$. The treatment is similar to that for the ordinary semilogarithmic analysis. The noise-free analysis determines reliable rate constants and newly defined "initial" intensities I_{A_0}, I_{B_0}, and I_{C_0} at t_0. Another type of problem can be resolved by the shifted lower limit of integration. Nascent rotational temperature of the molecules produced in the photolysis or reactions is not always equal to the ambient temperature. Rotational relaxation must be completed to monitor the concentration of a vibrational level by the signal due to a single rotational transition in LIF or MPI. Since rotational relaxation is much faster than vibrational relaxation,[1,4] an appropriate short delay for the lower limit of the integration (t_0) permits a reliable analysis without undesirable effect due to the non-thermalized rotation. Similarly, if the reaction producing vibrational levels A, B, and C is not completed instantaneously at $t = 0$, the initial time of integration (t_0) can be placed at the time after termination of the reaction.

Furthermore, all the lower limits of the integrals do not have to be the same. The temporal profile of A, i.e., [A], which appears in equations (10) is the same as [A] in equation (9), whereas the lower limits of the integrals in equations (10) and (11) may be different from that in equation (9). A different lower limits of the integrals offers an advantage in the analysis. There are some cases in which the level A shows growth immediately after $t = 0$ because of relaxation from a higher level X that cannot be detected. The lower limit t_0

in equation (9) is defined as the initial time of the range over which the semilogarithmic plot [A] vs. t (see (2)) or the plot [A] vs. $\int_{t_0}^{t}[A]dt$ (see (9)) shows a straight line. Rate constant k_1 is determined from the slope. The lower limits t_0 in (10) and (11) can be smaller than that in (9) as long as neither B nor C is not directly produced from the X. The presence of X, which is a vibrational level higher than the observed highest level, does not lead to an uncertainty of the parameters in the rate constants and relative detectivities.

Recall that observed signal intensities are proportional to the concentrations, for example $I_A = \alpha[A]$. The concentrations in equations (9), (10), and (11) have to be replaced with the signal intensities $I_A = \alpha[A]$, $I_B = \beta[B]$, and $I_C = \gamma[C]$, and the following equations are obtained:

$$I_A = I_{A_0} - k_1 \int_{t_0}^{t} I_A dt \tag{12}$$

$$I_B = I_{B_0} + \frac{\beta}{\alpha} k_1 \int_{t_0}^{t} I_A dt - k_2 \int_{t_0}^{t} I_B dt \tag{13}$$

$$I_C = I_{C_0} + \frac{\gamma}{\beta} k_2 \int_{t_0}^{t} I_B dt \,. \tag{14}$$

Note that the relative values among detection sensitivities (β/α and γ/β) are not known prior to the analysis. From a statistical point of view, k_1, $(\beta/\alpha)k_1$, k_2, and $(\gamma/\beta)k_2$ are partial regression coefficients, I_{A_0}, I_{B_0}, and I_{C_0} are constants, the integrals are independent variables, and I_A, I_B, and I_C are dependent variables. Since all the values of the partial regression coefficients are given by the multiple linear regression analysis, rate constants k_1 and k_2

and relative sensitivities β/α and γ/β are determined unequivocally. Analysis of the data shown in Fig. 6.1(a) by the present integrated profiles method gave correct rate constants ($k_1 = 3.9999\times10^3$ s^{-1} for A $\rightarrow$ B and $k_2 = 3.7999\times10^3$ s^{-1} for B $\rightarrow$ C) and a profile. The result is not shown because the curve obtained by the analysis is almost identical with the analyzed data. It was also confirmed that resulting parameters were independent of the temporal range of the analysis. The same rate constants and relative detectivities were actually obtained from the data within both 0 - 100 μs and 0 - 2 ms. Similarly, the results were the same when the data in the range of both 0 - 2 ms and 1.8 - 2 ms were analyzed.

In order to demonstrate the advantage of the present integrated profiles, the synthetic data was burdens with some realistic noise and deals with various types of complicated kinetic schemes. Counting noise, a random noise that is proportional to a square root of the intensity of the signal, was put on the data. The magnitude of counting noise was adjusted so that the signal-to-noise ratio was about 10 anywhere in the data. The parameters for scheme (1) were set to be $k_1 = 4.0\times10^3$ s^{-1} and $k_2 = 3.8\times10^3$ s^{-1}; the values of k_1 and k_2 are close to each other, but not the same. Since only the relative concentrations are necessary, $[A]_0 = 1$ and $[B]_0 = 0$ are given as the initial conditions and, as a consequence, the nominal constant C [= $(k_1[A]_0)/(k_1-k_2)$] is 20. For simplicity, the sensitivity of the signal of A is assumed to be the same as that of B, i.e., $\beta/\alpha = 1$. The synthetic profile of the species B is shown by the dots in Figure 6.2. It was shown that conventional non-linear fit was likely to derive incorrect rate constants from a profile with the same rate constants as those in the present study even if there was no noise on the

data.

The analysis using equations (13) and (14) gives correct rate constants $k_1 = 4.001\times10^3$ s^{-1} and $k_2 = 3.804\times10^3$ s^{-1}, relative sensitivity $\beta/\alpha = 1.000$, and the initial concentration $[A]_0 = 1.005$. The calculated factor C = 20.3 is also satisfactory. The solid line in Fig. 6.2 was obtained by numerical integration of rate equations by Runge-Kutta-Gill method with rate constants determined by the present analysis. We also synthesized ten sets of profiles with different noises but with the same rate constants k_1 and k_2 ($k_1 = 4.0\times10^3$ s^{-1} and $k_2 = 3.8\times10^3$ s^{-1}). Results averaged over the data are $k_1 = (4.011 \pm 0.040)\cdot10^3$ s^{-1} and $k_2 = (3.792 \pm 0.028)\cdot10^3$ s^{-1}. These values are in excellent agreement with the correct rate constants.

The new analysis can also be applied to extended consecutive processes, such as the vibrational relaxation shown here schematically

$$\mathrm{A} \xrightarrow{k_1} \mathrm{B} \xrightarrow{k_2} \mathrm{C} \xrightarrow{k_3} \mathrm{D}. \qquad (15)$$

The profile of C is governed not only by the rate constants k_2 and k_3, but also by k_1, because the relaxation from B $\rightarrow$ C occurs simultaneously with that from A $\rightarrow$ B. The profile of C is not exactly a double-exponential curve unless the process B $\rightarrow$ C is completely separated in time from the preceding relaxation A $\rightarrow$ B owing to a sufficiently large difference between k_1 and k_2. Nevertheless, since the profile of C frequently appears to be a simple growth and decay profile, double-exponential analysis is performed on an approximation called "stepped relaxation", by which the species A is assumed

to be almost exhausted when the relaxation of B begins [17-19]. However, this type of analysis does not always derive accurate rate constants for the relaxation. The present integrated method, on the other hand, can be applied without any complications to obtain rate constants for the profiles of C and D in scheme (15).

Determination of the Rate Constants for State-to-State Vibrational Relaxation

When vibrational relaxation with $\Delta v = 2$ cannot be neglected, two paths (A → B and A → C) of relaxation from A must be taken into account as shown in the following scheme:

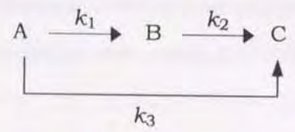

(16)

Since none of the analytical solutions of the rate equations for A, B, and C have terms whose time dependence is governed by only k_1 or k_3, the values or the ratio of k_1 and k_3 are difficult to determine by non-linear analysis. The present method, on the other hand, gives the following regression equations in the same manner as it gave equations (12) and (13):

$$I_A = I_{A_0} - (k_1 + k_3)\int_0^t I_A dt \tag{17}$$

$$I_B = I_{B_0} + \frac{\beta}{\alpha}k_1\int_0^t I_A dt - k_2\int_0^t I_B dt \tag{18}$$

$$I_C = I_{C_0} + \frac{\gamma}{\alpha}k_3\int_0^t I_A dt + \frac{\gamma}{\beta}k_2\int_0^t I_B dt\,. \tag{19}$$

Since the five linear regression coefficients, $k_1 + k_3$, $(\beta/\alpha)k_1$, k_2, $(\gamma/\alpha)k_3$, and $(\gamma/\beta)k_2$, are obtained by the analysis, unequivocal determination of the parameters k_1, k_2, k_3, β/α, and γ/α (γ/β is calculated from β/α and γ/α) can be made from simultaneous equations made by the regression coefficients.

An example of the analysis is shown in Fig. 6.3. Overall decay rate constants $k_1 + k_3$ for A, and k_2 for B are the same as in scheme (1) ($k_1 + k_3 = 4.0\cdot10^3$ s^{-1} and $k_2 = 3.8\cdot10^3$ s^{-1}), and the former is divided into $k_1 = 2.5\cdot10^3$ s^{-1} and $k_3 = 1.5\cdot10^3$ s^{-1}. The sensitivities α, β, and γ are to be unity in the data shown in Fig. 6.3. Results of the analysis are $k_1 = 2.486\cdot10^3$ s^{-1}, $k_2 = 3.808\cdot10^3$ s^{-1}, $k_3 = 1.521\cdot10^3$ s^{-1}, $\beta/\alpha = 1.008$, and $\gamma/\alpha = 0.998$. All the parameters are in excellent agreement with the correct values and the profiles are well-reproduced, as shown by the solid lines in Fig. 6.3.

If the A, B, and C are produced in a reaction or photolysis, a nascent distribution can also be determined. Since the initial signal intensities I_{A_0}, I_{B_0}, and I_{C_0}, and the relative sensitivities γ/α and γ/β are determined, the initial population ratio, $[A]_0 : [B]_0 : [C]_0 = I_{A_0}/\alpha : I_{B_0}/\beta : I_{C_0}/\gamma$, are calculated from $I_{A_0}(\gamma/\alpha) : I_{B_0}(\gamma/\beta) : I_{C_0}$. Therefore, a nascent vibrational distribution is determined without information on photochemical parameters, e.g., Franck-Condon factors and rotational level dependence of fluorescence quantum yields of excited states[21-28]. Since precise photochemical parameters are not always available for the molecule of interest, this method presents a new way to obtain information of the dynamics of chemical reactions and photolysis.

The present method can also be applied to more complicated and general

schemes in which reverse reactions are not negligible. Consider a reaction network in which three species (vibrational levels) are involved:

$$A \underset{k_{-1}}{\overset{k_1}{\rightleftharpoons}} B \qquad (20)$$

$$B \underset{k_{-2}}{\overset{k_2}{\rightleftharpoons}} C \qquad (21)$$

$$C \underset{k_{-3}}{\overset{k_3}{\rightleftharpoons}} A\,. \qquad (22)$$

Analytical solutions of the rate equations for schemes (20) to (22) are too complicated to be analyzed by conventional non-linear methods. It is easy, however, to simply integrate the rate equations:

$$I_A = I_{A_0} - (k_1 + k_{-3})\int_0^t I_A dt + \frac{\alpha}{\beta}k_{-1}\int_0^t I_A dt + \frac{\alpha}{\gamma}k_3\int_0^t I_C dt \qquad (23)$$

$$I_B = I_{B_0} + \frac{\beta}{\alpha}k_1\int_0^t I_A dt - (k_{-1} + k_2)\int_0^t I_B dt + \frac{\beta}{\gamma}k_{-2}\int_0^t I_C dt \qquad (24)$$

$$I_C = I_{C_0} + \frac{\gamma}{\alpha}k_{-3}\int_0^t I_A dt + \frac{\gamma}{\beta}k_2\int_0^t I_B dt - (k_{-2} + k_3)\int_0^t I_C dt\,. \qquad (25)$$

Though seemingly complicated, all three equations are linear, so their unknown time-independent parameters can be determined by a simple least-squares analysis. Three constants I_{A_0}, I_{B_0}, and I_{C_0} and nine regression coefficients (coefficients of the integrals) are readily and unequivocally

obtained, and then all the rate constants are derived from simultaneous equations made by the coefficients. Figure 6.4 shows the successful reproduction of all the profiles. Ten synthetic data with different noise, as shown by schemes (20), (21), and (22) were also analyzed and the results lists in Table 1. Results obtained by the present method are satisfactory.

Thus far, only closed systems have been treated. A different scheme, incorporating loss of the species from the system will be considered next. For example, diffusion loss is sometimes observed when a probed volume, i.e., cross section of a probe laser beam, is small. A scheme can be represented by

$$A \xrightarrow{k_1} B \xrightarrow{k_2} C\,. \qquad (26)$$

$$A,\ B,\ C \xrightarrow{k_d} \text{diffusion loss}, \qquad (27)$$

where it is assumed that the rate constant for the diffusion loss is the same for all species. The assumption is reasonable when the scheme represents vibrational relaxation, because A, B, and C have the same mass and also must have nearly the same diffusion rates[4]. The parameters for synthetic curves are: $k_1 = 2.5\times10^3\ s^{-1}$, $k_2 = 5.0\times10^3\ s^{-1}$, $k_d = 2.25\times10^3\ s^{-1}$, $\alpha = 1.0$, $\beta = 8.0$, $\gamma = 5.0$ and $[A]_0 : [B]_0 : [C]_0 = 3.0 : 0.1 : 1.0$. The rate constants and the initial population ratios are not realistic but appropriate to illustrate that the profile of C is not represented by the double-exponential form. The regression equations for the analysis are:

$$I_A = I_{A_0} - (k_1 + k_d)\int_0^t I_A dt \qquad (28)$$

$$I_B = I_{B_0} + \frac{\beta}{\alpha} k_1 \int_0^t I_A dt - (k_2 + k_d) \int_0^t I_B dt \qquad (29)$$

$$I_C = I_{C_0} + \frac{\gamma}{\beta} k_2 \int_0^t I_B dt - k_d \int_0^t I_C dt \,. \qquad (30)$$

The rate constant k_d for the common diffusion loss is obtained by equation (30), after which k_1 and k_2 can be determined from the results given by equations (28) and (29). When k_1 and k_2 are determined, the ratios β/α and γ/β are calculated from $(\beta/\alpha)k_1$ and $(\gamma/\beta)k_2$ obtained from equations (29) and (30), respectively. Consequently, all the rate constants and relative sensitivities are determined unequivocally. Figure 6.5 shows that the present integrated analysis reproduces the data successfully. The parameters giving the resultant curve are $k_1 = 2.504\times10^3$ s^{-1}, $k_2 = 4.990\times10^3$ s^{-1}, $k_d = 2.251\times10^3$ s^{-1}, $\alpha = 1.0$, $\beta = 7.973$, $\gamma = 4.986$, and $[A]_0 : [B]_0 : [C]_0 = 3.009 : 0.099 : 1.006$. Furthermore, ten synthetic data with different noise were analyzed, and the results, listed in Table I, are shown to be in excellent agreement with the correct parameters used to prepare the data.

Defects or limits of the present method should be referred to here. If the loss of the species is due to background reactions with different rate constants instead of diffusion loss (scheme (27)), rate constants and relative detectivities cannot be determined unequivocally. In other words, the present method does not give respective values of rate constants, k_1 and k_2, and relative detectivities of A, B, and C in the following schemes.

$$\mathrm{A} \xrightarrow{k_1} \mathrm{B} \qquad (31)$$

$$\mathrm{A} \xrightarrow{k_2} \mathrm{C}. \qquad (32)$$

Only a sum of rate constant, $k_1 + k_2$, and relative detection sensitivities multiplied by each rate constant, $(\beta/\alpha)k_1$ and $(\gamma/\alpha)k_2$, are merely determined. Because rate constants, k_1 and k_2, in the schemes (31) and (32) cannot also be derived by conventional non-linear fit as long as relative concentration between B and C is not given, the defect described above does not indicate that the method in the present paper is inferior to conventional methods of analysis.

Determination of nascent vibrational distributions

Ratios among the relative sensitivities, $\alpha : \beta : \gamma$, are independent of time because they are apparatus constants. Once the ratios are determined, time-evolution of relative concentrations on vibrational levels can be obtained. When the time constant of a preceding reaction is much shorter than that of a vibrational relaxation, all the vibrational levels are produced instantaneously like photolysis. In such cases, the initial vibrational distribution can be determined from the signal intensities at $t = 0$ (I_{A_0}, I_{B_0}, and I_{C_0}). The initial relative populations of the vibrational levels, $[A]_0 : [B]_0 : [C]_0$ are given by $I_{A_0}/\alpha : I_{B_0}/\beta : I_{C_0}/\gamma = I_{A_0} : (\alpha/\beta)I_{B_0} : (\alpha/\gamma)I_{C_0}$.

However, the signal intensities at $t = 0$ are not always determined precisely when the reaction is not sufficiently faster than the following relaxation. An example of such profiles is shown in Fig. 6.6(a). The profiles are synthesized according to the following scheme:

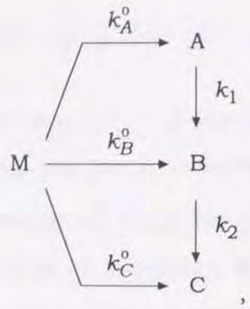

(33)

where M is a reactant converted to the product vibrational levels A, B, and C, and k_i^o denotes a rate constant for the reaction M $\rightarrow$ i (i = A, B, and C). As can be seen in Fig. 6.6(b), the nascent relative vibrational populations of A, B, and C cannot be determined because of the overlap between the timescales of the reaction and relaxation. Even in such cases, the initial population of each vibrational level can be obtained by the following analysis.

If the integrated profiles method is applied to the observed profiles A, B, and C first, the rate constants for the relaxation (k_1 and k_2) are determined as described in the previous section. Since the relative sensitivities for A, B, and C are also obtained in the first analysis, profiles of relative concentrations can be drawn in a graph whose ordinate is common for all the vibrational levels as shown in Fig. 6.6. The profile of M shows a single-exponential decay

$$[\mathrm{M}] = [\mathrm{M}]_0 \, exp(-k^o t), \tag{34}$$

where k^o (= $k_A^o + k_B^o + k_C^o$) is an overall rate constant for the reaction of M, and $[\mathrm{M}]_0$ is the initial concentration of M. The rate equations for A, B, and C in scheme (33) are

$$\frac{d[\mathrm{A}]}{dt} = k_A^o[\mathrm{M}]_0 \, exp(-k^o t) - k_1[\mathrm{A}] \tag{35}$$

$$\frac{d[\mathrm{B}]}{dt} = k_B^o[\mathrm{M}]_0 \, exp(-k^o t) + k_1[\mathrm{A}] - k_2[\mathrm{B}] \tag{36}$$

$$\frac{d[\mathrm{C}]}{dt} = k_C^o[\mathrm{M}]_0 \, exp(-k^o t) + k_2[\mathrm{B}] . \tag{37}$$

Because the concentrations of A and B at both t = 0 and t = ∞ are zero in scheme (33) as seen in Fig. 6.6(a), the integrated value of the left-hand side of equation (35) from t = 0 to t = ∞ is

$$\int_0^\infty \frac{d[\mathrm{A}]}{dt} dt = \int_0^\infty d[\mathrm{A}] = [\mathrm{A}]_\infty - [\mathrm{A}]_0 = 0 . \tag{38}$$

The same equation is also satisfied for B. Therefore, the following equations are obtained after integration of both sides of equations (35), (36), and (37) from t = 0 to t = ∞:

$$\frac{k_A^o[\mathrm{M}]_0}{k^o} = k_1 \int_0^\infty [\mathrm{A}] dt \tag{39}$$

$$\frac{k_B^o[\mathrm{M}]_0}{k^o} = k_2 \int_0^\infty [\mathrm{B}] dt - k_1 \int_0^\infty [\mathrm{A}] dt \tag{40}$$

$$\frac{k_C^o[\mathrm{M}]_0}{k^o} = [\mathrm{C}]_\infty - k_2 \int_0^\infty [\mathrm{B}] dt , \tag{41}$$

where $[\mathrm{C}]_\infty$ is the asymptotic concentration of C at t = ∞. Ratios among the rate constants (k_A^o, k_B^o, and k_C^o) for the reactions producing specific vibrational levels can be obtained from the ratios among the values of equations (39), (40)

and (41). Because the time-dependent profiles are drawn with the common ordinate, the right-hand sides of the equations are calculated using the rate constants determined in the first analysis. A real analysis of the profiles shown in Fig. 6.6 gave a perfectly correct set of the rate constants k_A^o, k_B^o, and k_C^o. Neither the overall rate constant k^o nor the initial concentration of M is necessary. The analysis described here can also be extended easily to the system containing more than three product vibrational levels.

There, however, is a defect of this method. If a part of the reaction products, A, B, and C in scheme (33) are lost by reactions with unknown different rate, rate constants k_1 and k_2 cannot be obtained in the first analysis as shown in the previous section. Accordingly, the calculation of the right-hand sides of equations (39), (40), and (41) are not possible, and thus the present method cannot be applied to the system in which vibrationally excited products undergo not only vibrational relaxation but also chemical reactions.

6.3 APPLICATION OF A NEW METHOD TO THE EXPERIMENTAL DATA: VIBRATIONAL RELAXATION AND THE INITIAL ENERGY DEPOSITION OF OH PRODUCED IN THE REACTION $O(^1D)$ + NH_3

6.3.1 Introduction

In the previous section, a new method of analyzing the time dependent profile of each vibrational level was explained. The method makes it possible to simultaneously determine the rate constants for vibrational relaxation and nascent vibrational distributions. Regression equations are linearized, and thus all the parameters for fitting can be obtained unequivocally. Because relative detection sensitivity for each vibrational level can also be determined, photochemical parameters for the correction of spectra are not necessary. In the present section, the method was applied to the reaction $O(^1D) + NH_3 \rightarrow OH(v) + NH_2$ followed by the relaxation of the OH by NH_3. There have been several reports on the rate constants for the vibrational relaxation of OH by NH_3[17,25-27] and the initial vibrational distributions of OH in the reaction $O(^1D) + NH_3$[27,28,29]. Since the results are qualitatively the same, the reaction is appropriate for demonstrating that the present method offers a reliable way of analyzing temporal profiles.

6.3.2 Experiment

The experimental apparatus have been outlined at previous section; details specific to this experiment are given below. Ozone was prepared by

electric discharge of oxygen and residual oxygen was thoroughly degassed. Ammonia and ozone were mixed in a flow before entering a fluorescence cell. A reaction $O(^1D) + NH_3$ was initiated upon irradiation of 248 nm light from a KrF excimer laser (Lambda Physik LEXtra 50, 10 mJ cm^{-2}) and the fluorescence from OH produced in the reaction was excited with a Nd^{3+}:YAG laser (Continuum YG660-20) pumped frequency doubled dye laser (Lambda Physik LPD-3001) with DCM dye. The signal from a photomultiplier (Hamamatsu R374) was averaged with a gated integrator (Stanford Research SR250) and processed with a computer. Vibrationally excited OH(υ = 0, 1, and 2) were detected via the transitions of (0,0), (1,1), and (2,2) of the $A^2\Sigma^+ - X^2\Pi$ system[32] and typical probe laser power was 80 - 100 μJ $pulse^{-1}$. Since the relaxation of rotation of OH is much faster than that of vibration[33], the intensity of LIF due to a single rotational line is in proportion to the population on each vibrational level. The delay time between the excimer and the dye laser was continuously scanned to record the time dependent profiles of the LIF signals.

Flow rates of all the gases were controlled with calibrated mass flow controllers (Tylan FC-260KZ and STEC SEC-400) and total pressure (N_2 buffer : 10 Torr) was monitored with a capacitance manometer (Baratron 122A). The total pressure measurement together with the mole fractions as measured by the flow controllers gave the partial pressure of reagents. Typical partial pressure of NH_3 was 25 mTorr and that of O_3 was 0.5 mTorr. Highly pure grade gases, O_2 (Toyo-Sanso, 99.9995 %), N_2(Nihon-Sanso, 99.9999 %), and NH_3(Nihon-Sanso, 99.999 %) were used without further purification.

6.3.3 Results and discussion

A. Rate constants for vibrational relaxation

Figure 6.7(a) shows observed time dependent profiles of LIF from OH normalized with their maximum intensities. The most likely exothermic reactions of $O(^1D)$ in the present system are

$$O(^1D) + NH_3 \rightarrow OH(\upsilon) + NH_2 \quad (42,v)$$

$$O(^1D) + N_2 \rightarrow O(^3P) + N_2 \quad (43)$$

$$O(^1D) + O_3 \rightarrow 2O_2 \quad (44)$$

$$OH(\upsilon) + NH_3 \rightarrow OH(\upsilon - 1) + NH_3 \quad (45,v)$$

$$OH(\upsilon) + N_2 \rightarrow OH(\upsilon - 1) + N_2. \quad (46,v)$$

As seen in Fig. 6.7(a), the production of OH(υ) is sufficiently faster than the relaxation. The rise of the lower levels (υ = 0 and 1 in Fig. 6.7(a)), and the decay of υ = 1 and 2 are due to vibrational relaxation. There have been no reports on the evidence of relaxation of OH by N_2. Rensberger et al.[26] tried to measure the rate constant for the relaxation of OH(υ = 1) by N_2; however, they did not observe apparent evidence of relaxation. Chalamala and Copeland[27] and Knutsen et al.[32] reported that removal rate constant for the relaxation by N_2 was not significantly different from zero even for the levels υ = 9 and 7. They only showed a scatter of the data as their upper limit. Therefore, the relaxations by N_2, i,e., (46,v) were neglected, and relaxations were governed by the collisions of NH_3 in the present experiment. The reactions of OH(υ = 0) with NH_3 and O_3, whose time constants are calculated to be 7 ms and 919 ms, are much slower than the observed decay rate of υ = 0. The level υ = 0 decayed slower with higher total pressure, and thus the decay of υ = 0 results

from a diffusion loss.

Rate equations for the scheme are written as follows:

$$\frac{d[\mathrm{OH}(v=2)]}{dt} = -\left(k_{21}[\mathrm{NH_3}] + k_d\right)[\mathrm{OH}(v=2)] \quad (47)$$

$$\frac{d[\mathrm{OH}(v=1)]}{dt} = k_{21}[\mathrm{NH_3}][\mathrm{OH}(v=2)] - \left(k_{10}[\mathrm{NH_3}] + k_d\right)[\mathrm{OH}(v=1)] \quad (48)$$

$$\frac{d[\mathrm{OH}(v=0)]}{dt} = k_{10}[\mathrm{NH_3}][\mathrm{OH}(v=1)] - k_d[\mathrm{OH}(v=0)], \quad (49)$$

where $k_{v,v-1}$ (v = 1 and 2) represent the second-order rate constants for the vibrational relaxation (45,v) and k_d is the first-order rate constant for the diffusion loss. It is assumed that the rate constant for the diffusion is the same for all the vibrational levels. The assumption is reasonable, because different vibrational levels have the same mass and they must have almost identical diffusion rates[4]. If all the exothermic energies of the reaction $O(^1D) + NH_3 \rightarrow OH + NH_2$, 165 kJ mol^{-1},[33] are deposited into OH, the highest populated vibrational level is v = 4. The relaxation from higher vibrational levels to v = 2 is not taken in account of in rate equation (47); nevertheless, the effect of the production and relaxation of the levels higher than v = 2 can be avoided as shown later.

The time dependent profiles of v = 2 and 1 are represented by the analytical solutions of equations (47) and (48). Unfortunately, the result obtained by non-linear analysis of the profile such as v = 1 is frequently ambiguous and have large errors[20]. A new method of analyzing the profiles and of determining the rate constants has been applied in the present

analysis. Analytical solutions are not necessary; what needs to be done is to simply integrate the equations (47), (48), and (49) in terms of t.

It should be noted that relative intensities of the LIF signals originating in different vibrational levels are not directly converted to relative vibrational populations. Since the detection sensitivities for vibrational levels are different and signal intensities are proportional to the absolute concentrations, the following equation

$$I_v = \alpha_v[\mathrm{OH}(v)] \quad (50)$$

is appropriate to associate the intensity of LIF (I_v) with the detectivity for the level v (α_v). Integration of equations (47), (48), and (49) with relation (50) gives the following equations:

$$I_2(t) = I_2(t_0) - \left(k_{21}[\mathrm{NH_3}] + k_d\right)\int_{t_0}^{t} I_2(t')dt' \quad (51)$$

$$I_1(t) = I_1(t_0) + \frac{\alpha_1}{\alpha_2}k_{21}[\mathrm{NH_3}]\int_{t_0}^{t} I_2(t')dt' - \left(k_{10}[\mathrm{NH_3}] + k_d\right)\int_{t_0}^{t} I_1(t')dt' \quad (52)$$

$$I_0(t) = I_0(t_0) - k_d\int_{t_0}^{t} I_0(t')dt' + \frac{\alpha_0}{\alpha_1}k_{10}[\mathrm{NH_3}]\int_{t_0}^{t} I_1(t')dt', \quad (53)$$

where $I_v(t)$ is a signal intensity of the level v at t. It should be noted that the upper limit of the integration is not infinite ($t = \infty$) but arbitrary time t and thus both sides of the equations are dependent on time. These equations have the form of ordinary multi-linear regression equations whose independent variables are the integrals. The ratios among detection sensitivities, α_1/α_2 and α_0/α_1, are not necessary prior to the analysis. The five partial regression coefficients, $k_{21}[NH_3] + k_d$, $k_{10}[NH_3] + k_d$,

$(\alpha_1/\alpha_2)k_{21}[NH_3]$, k_d, and $(\alpha_0/\alpha_1)k_{10}[NH_3]$ and the constants $I_\upsilon(t_0)$ are obtained by linear least-squares analysis. All the rate constants, k_{21}, k_{10}, and k_d and the ratios of sensitivities, α_1/α_2 and α_0/α_1 are determined unequivocally from the simultaneous equations composed of the five regression coefficients. The lower limit t_0 of the integration in equation (51) was defined to be the earliest time after which the semilogarithmic plot of the profile of OH(υ = 2) shows a straight line. In other words, there is little population on $\upsilon \geq 3$ after t_0. In the actual analysis, t_0 was set to be 13 μs.

The rate constants for vibrational relaxation obtained in the present study along with those previously reported are listed in Table 2. Relative sensitivities for the vibrational levels are also determined and profiles of relative populations can be drawn as shown in Fig. 6.7(b). Numerical integration of the rate equations (Runge-Kutta-Gill method) with rate constants obtained in the present analysis gives the solid lines in Fig. 6.7(b) which are almost identical with the observed profiles. The rate constant k_{21} ($\upsilon = 2 \rightarrow \upsilon = 1$) determined in the present study is in excellent agreement with previously reported values despite the difference of methods. There are also no significant differences among the rate constants k_{10} ($\upsilon = 1 \rightarrow \upsilon = 0$), although the values scatter a little larger than k_{21}.

Glass et al.[25] prepared vibrationally excited OH($\upsilon \leq 2$) by a reaction H + $NO_2 \rightarrow$ OH + NO in a fast-flow tube. Steady state analysis gave the ratio of the rate constants for several relaxers to the relaxation by NO. The reliability of their values are dependent on that of the rate constant for relaxation by NO, and, consequently, this is the reason for the discrepancy of k_{21} and relatively large error bars of k_{10}. Cheskis et al.[17] performed almost the same

experiments as the present study and they measured the profiles of OH produced in the reaction $O(^1D)$ + NH_3. They analyzed all the profiles with non-linear double-exponential fits on the assumption that relaxation $\upsilon + 2 \rightarrow \upsilon + 1$ terminated before the onset of $\upsilon \rightarrow \upsilon - 1$. However, the assumption is not always satisfactory and the treatment called "stepped relaxation" is an approximation in the analysis. This is a possible reason for the discrepancy of their k_{10}. Rensberger et al.[26] and Raiche et al.[27], they were in the same group, prepared OH(υ = 2) directly from OH(υ = 0) by overtone pumping with a Raman-shifted tunable dye laser. Time dependent profiles of populations on both υ = 1 and 2 were recorded by LIF with a UV laser. Since the OH(υ = 2) showed a simple exponential decay, their rate constants for k_{21} is most reliable and in good agreement with ours. The profile of υ = 1, on the other hand, was a double-exponential form with a growth and decay. They optimized the rate constant k_{10} by non-linear regression with fixed k_{21} until the observed profile was well reproduced. Their non-linear analysis was less ambiguous than the non-linear double-exponential analysis by Cheskis et al.[17], nevertheless any type of non-linear analysis cannot derive more unequivocal results than linear regression analysis in the present work.

B. The initial vibrational distributions

Since the highest vibrational level observed in the present study is υ = 2, the ratio of nascent populations $\upsilon = 1/\upsilon = 0$ is obtained from the following expression as described at section 6.2:

$$\frac{k_v[O(^1D)]_0}{\sum_v k_v} = \left(k_{v,v-1}[NH_3] + k_d\right)\int_0^\infty [OH(v)]dt - k_{v+1,v}[NH_3]\int_0^\infty [OH(v+1)]dt\,, \quad (54)$$

where k_v (v = 0 and 1) are the rate constants for the production of OH(v) in reaction (42,v). Since the values of the right hand side of (54) can be calculated after the first analysis, the ratio k_1/k_0, i.e., the initial population ratio $v = 1/v = 0$, is determined without the value of $[O(^1D)]_0$ or $\sum k_v$ in the left-hand side. As a result, the value for k_1/k_0 is obtained to be 1.3 ± 0.2 (2σ).

The ratio $v = 1/v = 0$ reported by Sanders et al.[28] ($1.4\ ^{+1}_{-0.5}$) and Cheskis et al.[17] (1.6 ± 0.5) are in agreement with ours, although their values have large error limits. A large discrepancy of the result, $v = 1/v = 0$: 0.66 ± 1.0, given by Córdova et al.[29] might be due to an error in the correction of saturation effect on their LIF excitation spectra. Saturation of signals has no effect on our analyses as long as signal intensities are proportion to the concentration. The value of Cheskis et al. are close to our values, although their approximation on the scheme is incorrect in the strict sense. All the findings demonstrate the reliability of the present method in determination of rate constants and nascent vibrational distributions.

References

1 R. D. Levine and R. B. Bernstein, "Molecular Reaction Dynamics and Chemical Reactivity," Oxford University Press (1987).

2 W. Demtröder, "Laser Spectroscopy," 2nd ed, Springer-Verlag (1982).

3 S. H. Lin, Y. Fujimura, H. J. Neusser, and E. W. Schlag, "Multiphoton Spectroscopy of Molecules," Academic Press (1984).

4 J. T. Yardley, "Introduction to Molecular Energy Transfer," Academic Press (1980).

5 R. N. Zare, and P. J. Dagdigian, *Science,* **185**, 739 (1974).

6 E. E. Marinero, C. T. Rettner, and R. N. Zare, *Phys. Rev. Lett.*, **48**, 1323 (1982).

7 E. E. Marinero, R. Vasudev, and R. N. Zare, J. *Chem. Phys.*, **78**, 692 (1983).

8 W. Hack and Th. Mill, J. *Phys. Chem.*, **97**, 5599 (1993).

9 K. Honma, J. *Chem. Phys.*, **99**, 7677 (1993).

10 K. Yamasaki and S. R. Leone, J. *Chem. Phys.*, **90**, 964 (1989).

11 D. R. Crosley, J. *Phys. Chem.*, **93**, 6273 (1989).

12 E. L. Chappell, J. B. Jeffries, and D. R. Crosley, J. *Chem. Phys.*, **97**, 2400 (1992).

13 D. E. Heard, D. R. Crosley, J. B. Jeffries, G. P. Smith, and A. Hirano, J. *Chem. Phys.*, **96**, 4366 (1992).

14 C. Capellos and B. H. Bielski, "Kinetic Systems," Wiley-Interscience (1972).

15 S. W. Benson, "The Foundations of Chemical Kinetics," Robert E. Krieger (1982).

16 K. J. Laidler, "Chemical Kinetics," 3rd ed, Harper & Row (1987).

17 S. G. Cheskis, A. A. Iogansen, P. V. Kulakov, O. M. Sarkisov, and A. A.

Titov, *Chem. Phys. Lett.*, **143**, 348 (1988).

18 S. G. Cheskis, A. A. Iogansen, P. V. Kulakov, I. Y. Razuvaev, O. M. Sarkisov, and A. A. Titov, *Chem. Phys. Lett.*, **155**, 37 (1989).

19 A. A. Iogansen, O. M. Sarkisov, E. V. Zimont, J. A. Seetula, R. S. Timonen, and S. Cheskis, *Chem. Phys. Lett.*, **212**, 604 (1993).

20 T. Carrington, *Int. J. Chem. Kinet.*, **14**, 517 (1982).

21. R. A. Copeland, M. L. Wise, and D. R. Crosley, *J. Phys. Chem.*, **92**, 5710 (1988).

22. D. R. Crosley, J. *Phys. Chem.*, **93**, 6273 (1993).

23. E. L. Chappell, J. B. Jeffries, and D. R. Crosley, *J. Chem. Phys.*, **97**, 2400 (1992).

24. D. E. Heard, D. R. Crosley, J. B. Jeffries, G. P. Smith, and A. Hirano, *J. Chem. Phys.*, **96**, 4366 (1992).

25 G. P. Glass, H. Endo, and B. K. Chaturvedi, *J. Chem. Phys.*, **77**, 5450 (1982).

26 K. J. Rensberger, J. B. Jeffries, and D. R. Crosley, *J. Chem. Phys.*, **90**, 2174 (1989).

27 G. A. Raiche, J. B. Jeffries, K. J. Rensberger, and D. R. Crosley, *J. Chem. Phys.*, **92**, 7258 (1990).

28 N. D. Sanders, J. E. Butler, and J. R. McDonald, *J. Chem. Phys.*, **73**, 5381 (1980).

29 J. F. Córdova, C. T. Rettner, and J. L. Kinsey, *J. Chem. Phys.*, **75**, 2742 (1981).

30 K. P. Huber and G. Herzberg, "Molecular Spectra and Molecular Structure IV, Constants of Diatomic Molecules," Van Nostrand Reinhold, New York, 1979.

31 B. R. Chalamala and R. A. Copeland, *J. Chem. Phys.*, **99**, 5807 (1993).

32 K. Knutsen, M. J. Dyer, and R. A. Copeland, *J. Chem. Phys.*, **104**, 5798 (1996).

33 W. B. DeMore, S. P. Sander, D. M. Golden, R. F. Hampson, M. J. Kurylo, C. J. Howard, A. R. Ravishankara, C. E. Kolb, and M. J. Molina, "Chemical Kinetics and Photochemical Data for Use in Stratospheric Modeling JPL Publication 94-26," Jet Propulsion Laboratory, California Institute of Technology, Pasadena, 1994.

Table 1. Rate constants and relative sensitivities determined by the integration method and comparison with correct values.[a]

Scheme[b]	k_1	k_{-1}	k_2	k_{-2}	k_3	k_{-3}	β/α	γ/α
(20) - (22)[c]	3.038±0.120	0.615±0.078	2.388±0.086	0.309±0.020	1.496±0.026	1.191±0.095	1.973±0.109	1.996±0.029
Correct values	3.0	0.6	2.4	0.3	1.5	1.2	2.0	2.0

Scheme[a]	k_1[b]	k_2	k_d	β/α	γ/α
(26) and (27)[d]	2.503±0.023	4.990±0.030	2.252±0.004	7.974±0.103	5.005±0.058
Correct values	2.5	5.0	2.25	8	5

[a]Rate constants are in units of 10^3 s^{-1}.

[d]Definition of the rate constants are shown in the schemes (20) - (22).

[c]Ten sets of synthetic data with different random noise were analyzed.

[d]Definition of the rate constants are shown in the schemes (26) and (27).

Table 2. Rate constants for the vibrational relaxation of OH.

	k_{21}[a)]	k_{10}[a)]	Method of analysis
Glass *et al.* [25]	$(0.80 \pm 0.30)\times10^{-10}$	$(2.5 \pm 0.5)\times10^{-11}$	Steady state analysis[b)]
Cheskis *et al.* [17]	$(1.0 \pm 0.3)\times10^{-10}$	$(2.1 \pm 0.3)\times10^{-11}$	Double-exponential fit
Rensberger et al. [26]	$(1.20 \pm 0.15)\times10^{-10}$	-	Single-exponential fit
Raiche *et al.* [27]	$(1.01 \pm 0.09)\times10^{-10}$	$(2.49 \pm 0.22)\times10^{-11}$	Single and double-exponential fit
This work[c)]	$(1.1 \pm 0.1)\times10^{-10}$	$(2.9 \pm 0.1)\times10^{-11}$	Integrated profiles

[a)] Rate constants for the vibrational relaxation in process (4) are represented by $k_{v,v-1}$.

[b)] Values in ref. 25 were corrected by Cheskis *et al.* [17] using more reliable rate constant for reference reaction.

[c)] Quoted errors are 2σ.

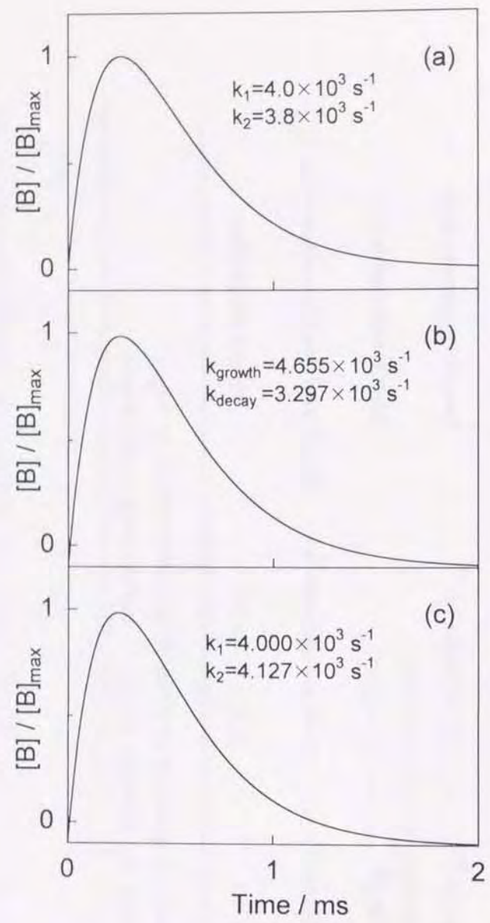

Fig. 6.1. Temporal profiles of the species B in a scheme of A → B → C. Each profile is normalized with its maximum value. (a) A synthetic profile of B with the rate constants: k_1 = 4.0×10^3 s^{-1} for A → B and k_2 = 3.8×10^3 s^{-1} for B → C; (b) A profile obtained by the non-linear double-exponential analysis: k_{growth} = 4.655×10^3 s^{-1} and k_{decay} = 3.297×10^3 s^{-1}; (c) A profile obtained by the optimization of the rate constant k_2 = 4.127×10^3 s^{-1} with a fixed k_1 = 4.000×10^3 s^{-1}. The initial trial set of the parameters were determined from semilogarithmic plot of the synthesized data over 1.5 - 2 ms on the assumption that S/N = 100. The method introduced in the present paper gave perfect results: k_1 = 3.9999×10^3 s^{-1} for A → B and k_2 = 3.7999×10^3 s^{-1} for B → C and almost identical profile with that shown in (a).

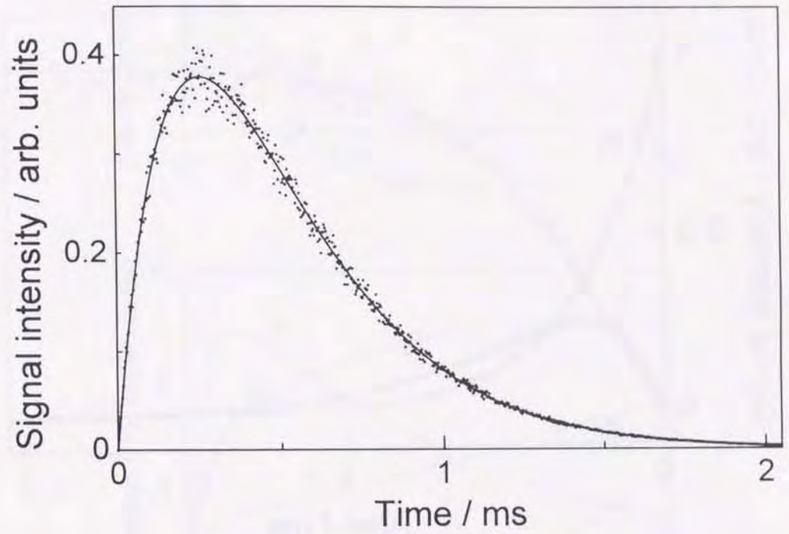

Fig. 6.2. Analyzed profile (shown by dots) and a curve (drawn with solid lines) obtained by the present analyses. The scheme is A → B → C with rate constants 4.0×10^3 s^{-1} for A → B and 3.8×10^3 s^{-1} for B → C.

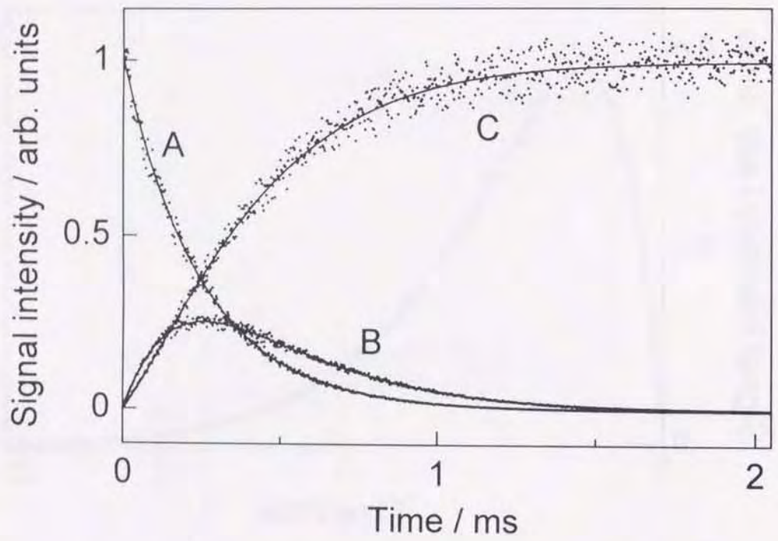

Fig. 6.3. Synthetic data (plotted with dots) and curves (drawn with solid lines) obtained by the integrated profiles method. The scheme is shown by (16) in the text.

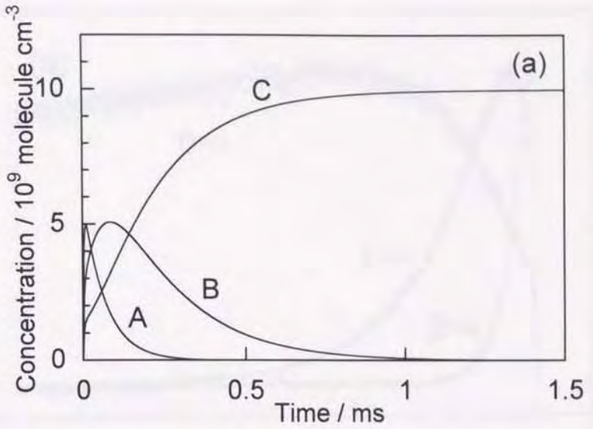

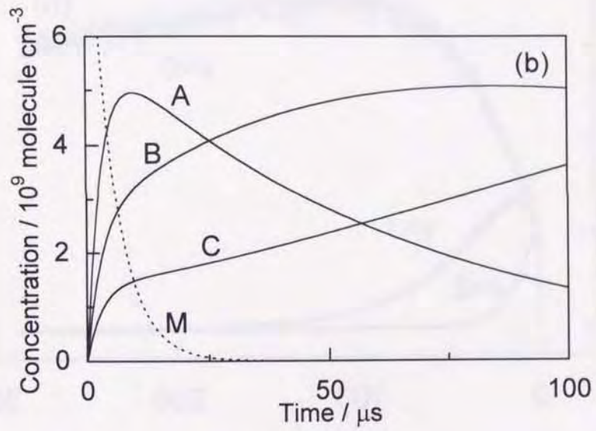

Fig. 6.6. Synthetic profiles of the species A, B, and C produced from a reaction of M (see scheme (33)). Rate constants for the reactions: $k_A^o = 2\times10^5$ s^{-1} (M → A); $k_B^o = 1\times10^5$ s^{-1} (M → B); and $k_C^o = 5\times10^4$ s^{-1} (M → C). Rate constants for the relaxation $k_1 = 1.5\times10^4$ s^{-1} (A → B) and $k_2 = 5\times10^3$ s^{-1} (B → C). The initial conditions are $[M]_0 = 1\times10^{10}$ molecule cm^{-3} and $[A]_0 = [B]_0 = [C]_0 = 0$. (a) Profiles over the range of 0 - 1.5 ms; (b) Expanded profiles over the range of 0 - 100 μs. The profile of the reactant M is shown by the broken line.

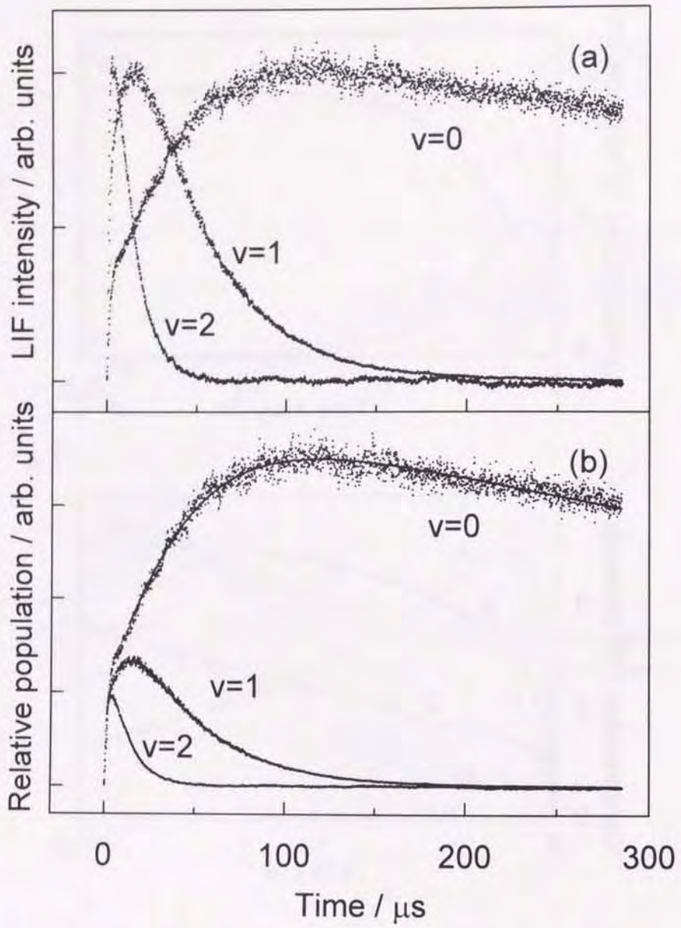

Fig. 6.7. (a) Time dependent profiles of LIF intensities of OH(v =0, 1 and 2) in the first 300 μs. All the profiles are normalized their maximum intensities. Total pressure (N_2) = 10 Torr; O_3 = 0.5 mTorr; and NH_3 = 26.4 mTorr. (b) Time dependent profiles of relative populations obtained by the analysis of (a). Dots denote observed data, and the solid lines are obtained by numerical integration of rate equations (Runge-Kutta-Gill method) using rate constants and the initial relative populations determined by the present method.

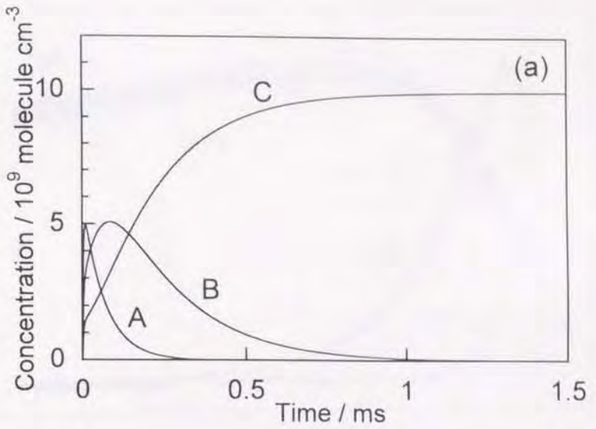

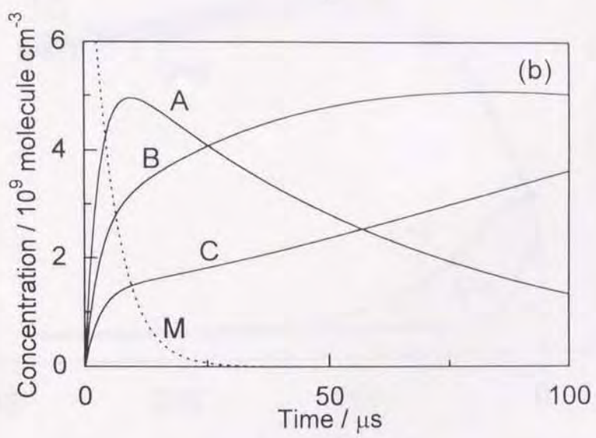

Fig. 6.6. Synthetic profiles of the species A, B, and C produced from a reaction of M (see scheme (33)). Rate constants for the reactions: $k_A^o = 2\times10^5$ s^{-1} (M → A); $k_B^o = 1\times10^5$ s^{-1} (M → B); and $k_C^o = 5\times10^4$ s^{-1} (M → C). Rate constants for the relaxation $k_1 = 1.5\times10^4$ s^{-1} (A → B) and $k_2 = 5\times10^3$ s^{-1} (B → C). The initial conditions are $[M]_0 = 1\times10^{10}$ molecule cm^{-3} and $[A]_0 = [B]_0 = [C]_0 = 0$. (a) Profiles over the range of 0 - 1.5 ms; (b) Expanded profiles over the range of 0 - 100 μs. The profile of the reactant M is shown by the broken line.

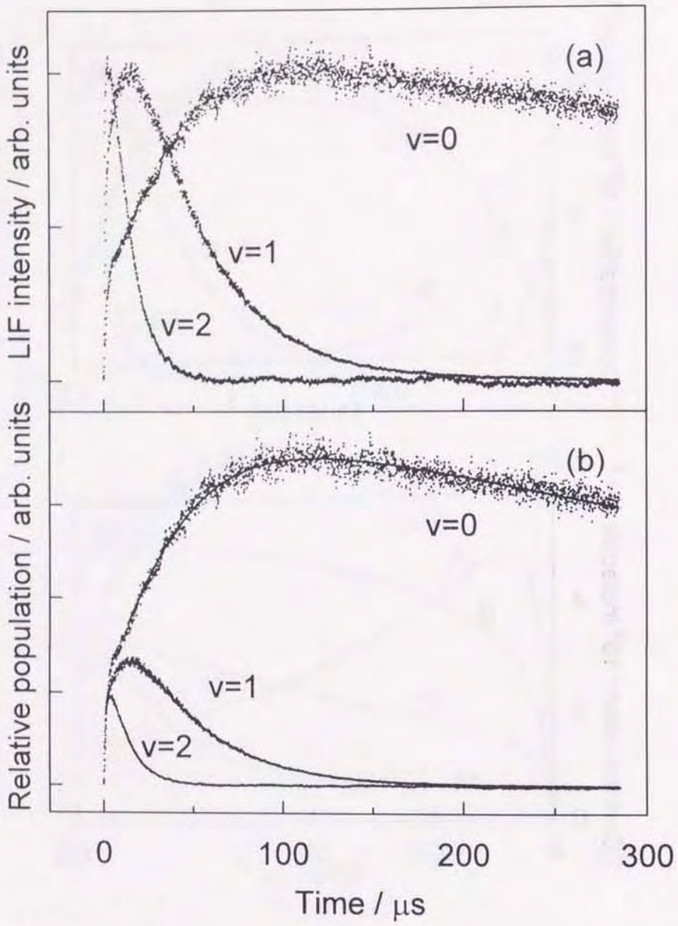

Fig. 6.7. (a) Time dependent profiles of LIF intensities of OH(v =0, 1 and 2) in the first 300 μs. All the profiles are normalized their maximum intensities. Total pressure (N_2) = 10 Torr; O_3 = 0.5 mTorr; and NH_3 = 26.4 mTorr. (b) Time dependent profiles of relative populations obtained by the analysis of (a). Dots denote observed data, and the solid lines are obtained by numerical integration of rate equations (Runge-Kutta-Gill method) using rate constants and the initial relative populations determined by the present method.